PRODUCTION OF C, N AND O FRAGMENTS IN THE INTERACTION OF ^{12}C WITH ^{12}C AT AN INCIDENT ENERGY OF 200 MeV

Mxolisi Justice Dlamini

Thesis presented in fulfillment of the requirements for the degree of Master of

Sciences in the Department of Physics and Engineering

University of Zululand.

Supervisor: Dr. S.V. Förtsch
Physics Group
iThemba LABS

Co-supervisor: Prof. M.O. Ndwandwe
Head: Department. of Physics and Engineering
Vice-Dean: Faculty of Science and Agriculture
University of Zululand

December 2006

DECLARATION

I, the undersigned, hereby declare that the work contained in this thesis is my own original work and that I have not previously in its entirety or in part submitted it at any university for a degree.

Signature: ....

Date: ....

Production of C, N and O fragments in the interaction of ^{12}C with ^{12}C at an incident energy of 200 MeV.

M.J. Dlamini[1,2]

[1]University of Zululand, Private Bag X1001, KwaDlangezwa 3886, South Africa

e-mail: mjdlamini@gmail.com

[2]iThemba LABS, Old Faure Road, Somerset West 7129, South Africa

e-mail: justice@tlabs.ac.za

Abstract

The double differential cross sections of different isotopes of carbon (C), nitrogen (N), and oxygen (O) emitted in the interaction of ^{12}C with ^{12}C at an incident energy of 200 MeV were measured in the angular range of 8°- 45°. The high-energy part of the spectra was measured with a Si ΔE-E detector while the corresponding low energy part was measured with a Bragg Curve Detector (BCD). The standard ΔE-E technique was used for particle identification which allowed good separation of different isotopes of the emitted fragments with $Z \geq 3$. The BCD could only resolve charge of different fragments. Energy spectra of the isotopes of C, N, and O indicate that at forward angles (8°-20°), the high-energy part of the spectra is produced by transfer reactions of few neutrons or protons from the projectile to the target nucleus or vice versa. At lower emission energies pre-equilibrium emission is mainly governed by nucleon coalescence and further by evaporation. As the emission angle as well as the mass of the fragments increases the evaporation process dominates the spectra. The fragments heavier than ^{17}O are almost entirely produced as evaporation residues.

Ukukhiqizwa kuka Khabhoni, Unayitrojini no Okusijini ekuhlanganeni kukaKhabhoni weshumi nambili no Khabhoni weshumi nambili ohamba ngomfutho ongu 200 MeV.

M.J. Dlamini[1,2]
[1]University of Zululand, Private Bag X1001, KwaDlangezwa 3886, South Africa
e-mail: mjdlamini@gmail.com
[2]iThemba LABS, Old Faure Road, Somerset West 7129, South Africa
e-mail: justice@tlabs.ac.za

Isifingqo

Ukwenzeka kwezinhlamvana ezahlukene zika Khabhoni, Unayitrojini no-Okusijini zikhishwa ukuhlangana kukaKhabhoni weshumi nambili no Khabhoni weshumi nambili ehamba ngomfutho ongu 200 MeV, lezi nhlamvana zakalwa kuma-engela kusuka ku 8° kuya ku-45°. Lezi zinhlamvana ezisinda ngokuphakathi nendawo zitholakala ngisho *ngomfutho omncane ngakho kubalulekile ukuthi zikalwe* emfuthweni omncane ukuze kuqondakale kahle izindlela ezakheka noma ezitholakala ngazo. Inxenye yesipekithilamu sezinhlamvu ezinomfutho omkhulu yakalwa ngesikali sikaSilikhoni onobubanzi obuncane alandelwe onobubanzi obukhulu, kanti inxenye yesipekithilamu sezinhlamvu ezinomfutho omncane yakalwa nge Bragg Curve detector. Indlela eyejwayelekile yokukala ngokubeka isikali esinobubanzi obuncane silandelwe esinobubanzi obukhulu yasentshenziswa ukuhlukanisa izinhlamvu, futhi eyavumela ukuhlukanisa izinhlamvana zohlamvu ngalunye ezinesisindo esilingana nokuthathu nangaphezulu. I-BCD yona ikhona ukuhlukanisa izinhlamvu ezahlukane kuphela.

Isipekithilamu somfutho wezinhlamvana zika Khabhoni, uNayitrojini kanye no Okusijini akhombisa ukuthi kuma-engela aphambili (8°-20°), inxenye yesipekithilamu esinomfutho omkhulu sikhiqizwa ukudluliswa kwama nwutroni noma amaprothoni kusuka kwi nucleyasi ethunyelwayo eya kuleyo athunyelwa kuyo noma kusuka esuka kuleyo athunyelwa kuyo eya kwethunyelwayo. Ekukhiqizweni komfutho omncane, i-pre-equilibrium ilawulwa i-nucliyoni kholisensi bese ngokuqhubeka kuba ukuhwamuka. Ngokukhuphuka kwe-engela yokukhiqiza ne sisindo sezinhlamvana, ukuhwamuka yikhona okuthatha indawo eningi. Izinhlamva ezisinda ngaphezu kuka okusijini weshumi sesikhombisa, cishe zonke zikhiqizwa ngezinsalela zomhwamuko.

ACKNOWLEDGEMENTS

I wish to express my thanks to all those who have assisted in bringing this thesis to completion. I am particularly indebted to

- My supervisor, Dr S.V. Förtsch for the guidance, for his support, motivation, patience, encouragement, and active participation he gave me during the start of this work until the end. God be with you (Unkulunkulu abe nawe).
- My university supervisor, Prof. O.M. Ndwandwe for his invaluable support and encouragement.
- Dr. F.D. Smit, Dr. R. Neveling, Dr. H. Fujita, Dr. Z. Buthelezi, Dr A.A. Cowley, Dr. S. Connell and Mr. S.S. Ntshangase for their generous assistance in many weekends of data taking.
- Professor E. Gadioli and Mr. Andrea Miarani of the University of Milano for performing theoretical calculations for this project.
- My loving and generous friends for their motivation, co-operation and support.
- Most importantly, my wonderful loving family for their support, encouragement, generosity and outpouring of love, throughout the year.

This work is dedicated to my late uncle Samuel Bhekinkosi Khumalo and my family umama nobaba, abafowethu nodadewethu kanye nabo bonke omalume nomalumekazi. Ngibonga kakhulu indlela eningixhase ngayo ezikhathini ezinzima. Inkosi ibenani nginithanda nonke.

Mxolisi Justice Dlamini *UniZulu, December 2006*

CONTENTS

LIST OF FIGURES

LIST OF TABLES

CHAPTER 1

Introduction

1.1 Overview

It has been demostrated that when the incident energy for heavy ion reactions is raised above 10 MeV/nucleon, a kind of transition region [Mör88] is entered. At incident energies below 10 MeV/nucleon, the projectile and target keep their shape and either fuse completely or separate again after a deep inelastic collision while at higher incident energies (above 10 MeV/nucleon) it is expected that different phenomena may occur [Mag98]. In fact at an energy above 10 MeV/nucleon the projectile gains a high velocity such that the target has an influence on the projectile. The projectile feels a differential force, the side facing the target getting attracted whereas the rest moves more or less unaffected. Due to this effect the projectile might break up and part of it may fuse with the target. The incomplete fusion and the subsequently emission of ejectiles are observed over a gradually rising mass and velocity range [Mag98]. Some of the reaction mechanisms that dominate the region around 10 MeV are incomplete fusion, deep inelastic collision and projectile break-up.

Many experimental studies have also been conducted at iThemba LABS to explain the emission of the Intermediate Mass Fragments (IMF) in the interaction of many different nuclei at energies above 10 MeV/nucleon [Bec03], [Gad03], [Ste05], [För05]. The emission of these Intermediate mass fragments is common in heavy ion reactions. These fragments are commonly defined to have charges of $3 \leq Z \leq 13$. In the interaction of medium heavy ions at the energies ranging from 6 to 25 MeV/nucleon, IMF are produced either by the break-up of the projectile or by the nucleon coalescence. The break-up of a projectile is considered during the course of the nucleon-nucleon interaction cascade which starts as soon as the two ions come into contact. The orderly kinetic energy of the composite nucleus created in the complete or partial fusion of the projectile and the target transforms into random thermal energy. Furthermore, in projectile break-up the fragment is produced together with a fragment with smaller mass and charge. If this fragment fuses with the target nucleus, it is unlikely that a fragment of charge and mass equal to those of the already produced heavy fragments will be formed. A fragment of charge and mass comparable to the projectile may be produced by nucleon coalescence only if the entire projectile fuses with the target nucleus. More than one isotope may contribute to the produced fragment. The studies of the light ion system in the emission of alpha particles from the reaction ^{12}C + ^{12}C at 28.7 MeV/nucleon has suggested that the energy spectra of particles with $6 \leq A \leq 12$ indicated the projectile fragmentation accompanied by the energy dissipation due to interaction with the target [Sze91]. In the interactions of ^{12}C with ^{12}C, ^{27}Al and ^{58}Ni at energy 28.7 MeV/nucleon suggested that Li, Be, and B are mainly produced by projectile fragmentation [Cze91]. The IMFs are observed even at lower incident energies [Gad03], the present study have undertaken to test the inferred reaction mechanisms involved in the production of IMF heavier than the projectile or target at an incident energy of 16.67 MeV/nucleon.

1.2 Reaction mechanisms

Some of the possible reaction mechanisms that might be involved in the production of intermediate mass fragments in the interaction of ^{12}C with ^{12}C at an incident energy of 200 MeV are direct nucleon transfer, pre-equilibrium, fragmentation, evaporation, nucleon coalescence via complete and incomplete fusion, deep inelastic reactions. These reaction mechanisms are discussed below.

1.2.1 Direct and nucleon transfer reactions

In general, direct reactions are applied to all processes that directly connect the initial and final states in nuclear reactions without formation of an intermediate compound system [Gad92], [Lil01]. The contribution to these processes comes from the surface region of the nucleus where an incident projectile can interact with one or a few target nucleons or induce a simple normal mode of nuclear motion like a shape oscillation. Direct reactions favour emission of high-energy particles with the excitation of low energy states of the residual nucleus. The examples of direct reactions include elastic scattering, which can be explained by the interaction between the incident nucleon and the nucleus is given by a one body potential; inelastic scattering which excites collective states which involves the coherent motion of many nucleons.

In transfer reactions a nucleon or cluster of nucleons is transferred from the projectile to the target or from the target to the projectile [Gad92]. One nucleon transfer reactions provide information about the single-particle aspects of nuclei and allow the energies of single particle states to be determined. One nucleon transfer reactions are divided up into reactions that either transfer a nucleon to an unfilled state of the residual nucleus (stripping reactions) and those that remove a nucleon from a filled or partially filled state of the target nucleus (pick-up reactions). More than one nucleon or clusters of nucleons can be transferred from the projectile to the target or vice versa. Such nuclear reactions may be treated by the same general methods as one nucleon transfer reactions, mainly because of the difficulty of describing the bound state properties of the transferred clusters. Transfer reactions can be studied experimentally with a magnetic spectrometer since the interest is in the high energy resolution of the discrete region at high energy part of the spectra.

1.2.2 Pre-equilibrium reactions

Pre-equilibrium processes occur between the one step direct processes [Gad92] which involve few degrees of freedom and the compound nucleus reactions in which the projectile energy is divided between all the nucleons of the compound nucleus in a completely statistical way. A pre-equilibrium process is described as the emission of fast particles prior to equilibration of the compound nucleus. These particles which are emitted to the pre-equilibrium region, also referred to as the continuum, are described by most existing models in terms of a sequence of nucleon-nucleon (N-N) interactions inside the target nucleus from which particles can be emitted after any stage. It's mainly light energetic particles which are emitted in these fast direct processes.

1.2.3 Fragmentation

Projectile or target break-up also known as far break-up as described in the perturbative Serber [Ser47] approximation has a maximum at the energy corresponding to the beam velocity and a width related to the momentum distribution of the observed fragment within the projectile. This is assumed to be a peripheral direct reaction by which the projectile breaks up into two fragments which may be emitted without further interactions with the target nucleus. Alternatively one fragment may excite and even fuse with the target nucleus. The target could also break-up into two fragments, one of which might interact with the projectile.

1.2.4 Nucleon coalescence and thermalization through complete and incomplete fusion.

The fusion of the projectile with the target nucleus (complete fusion) or the fusion of the participant [Gad03] fragment with the nucleus after projectile break-up (incomplete fusion) creates a non-equilibrated excited nucleus. When the projectile fuses with the target nucleus, a large amount of energy and momentum is transferred to the target nucleus which leads to the formation of the compound nucleus. The produced nucleus is heavier than either the original projectile or target nucleus. The incomplete fusion involves either a partial overlap between projectile and target or the break-up of the projectile into two fragments. One of these fragments (participant fragment) fuses with the target nucleus.

The non-equilibrated nucleus reaches statistical equilibrium through a cascade of nucleon-nucleon (N-N) interactions during which nucleons or clusters of nucleons maybe emitted with higher emission energies than expected from evaporation by an equilibrated system.

This so called nucleon coalescence is observed at higher energies because this is where complete fusion is dominant, the interaction of two ions, slowed by their Coulomb repulsion, takes so long that the orderly energy of the projectile's nucleons transforms into thermal energy when they still form a dinuclear system and a large part of the Coulomb potential energy is not transformed into nucleon kinetic energy. This limits the emission of pre-equilibrium particles. At higher incident energy, the two nuclei overlap much faster and their nucleons may even increase their energy when they fall in the common potential well because the composite nucleus Fermi energy is greater than those of the projectile and the target [Gad03].

1.2.5 Evaporation

This nuclear reaction mechanism begins with the capture of the projectile or participant fragment by the target nucleus followed by the sharing of its energy among all the nucleons of the compound system [Gad92]. The compound nucleus lives long enough for complete statistical equilibrium to be established. According to Bohr independence hypothesis the decay of a compound nucleus is determined entirely by its energy, angular momentum, and parity and not by the way it was formed [Gad92]. It is necessary for the validity of the independence hypothesis that a long time should elapse between the formation of the compound system and its eventual decay. This is the case if the average excitation energy of the nucleon in the compound system is much less than the energy needed by any one of the nucleons to escape from the nucleus, making it very unlikely that sufficient energy is concentrated on one particle to enable it to escape. Subsequently, long after capture, light particles are emitted by a statistical process similar to the evaporation of molecules from a liquid drop, until finally the nucleus reaches its ground state by gamma emission. Mainly light particles evaporate from the excited compound nucleus, leaving amongst others IMF as evaporation residues.

1.2.6 Deep-inelastic collision

When two nuclei collide, they lead to a complex sequence of reaction processes [Lil01]. As the projectile approaches the target nucleus, a significant part of their relative kinetic energy is converted into Coulomb potential energy. This means that they may be moving slow enough so that, during the initial interaction as they pass each other, there is enough time for a large amount of the remaining relative kinetic energy to be converted into internal excitation. The energy dissipation occurs via nucleon-nucleon collisions and mass exchange through the region of contact, where a neck of nuclear matter may form as the two nuclei stick together and begin to rotate as a single unit. The angular momentum is too large for fusion to take place and, a short time later, the fragments separate again with a certain amount of kinetic energy corresponding to their relative angular momentum. They then acquire a considerable amount of extra kinetic energy from their Coulomb potential energy as they repel each other. During the initial interaction, nucleon transfer occurs in both directions and the masses and charges of the final products may not be very different from those of the initial reactants. However, contact time does not last long enough for a complete rotation of the combination to take place and the angular distribution is peaked in the forward direction. Deep inelastic collision plays a role in the production of fragments, in particular of those with velocities substantially below beam velocity at the incident energy below 10 MeV/nucleon.

1.3 Carbon induced IMF production

In recent studies, the emission of Intermediate Mass Fragments (IMF) in ^{12}C-induced reactions has been investigated at incident energies ranging from 100 to 400 MeV ([Bec03], [Gad01]). A general theory which explains all the observed features in the production of IMF is however still lacking. A quite considerable emission yield of IMF is observed even at the lower incident energies. Therefore, it is important to study the IMF emission also at low incident energies to improve the understanding of the reaction mechanisms involved. A series of these experiments have been conducted at iThemba LABS to extend the understanding of the underlying reaction mechanisms. One of these experiments was the interaction of ^{12}C and ^{16}O with ^{103}Rh at incident energies up to 33 MeV/nucleon, in which the angular and forward recoil range distributions of residues were studied [Bir96], [Gad97], [Gad98], [But04]. This study has suggested that at a low energy, the dominant mechanism in these reactions is complete fusion and incomplete fusion of alpha fragments which subsequently led to inclusive measurements of alpha [Gad99], ^{8}Be [Gad01] and other IMF [Gad03] produced in the interaction of ^{12}C with various nuclei. These were followed by a study of the emission of IMF in the interaction of ^{16}O with ^{59}Co, ^{93}Nb and ^{197}Au which were investigated at incident energies varying from 6 to 25 MeV/nucleon [Gad03]. This study suggested that the spectra of these IMFs at forward angles are dominated by a component originating from break-up of the projectile. At higher excitation energies nucleon coalescence was found to reproduce the energy spectra over the entire angular range. It was also suggested that at higher incident energy, prior to break-up the projectile suffers an energy loss consequently it was considered that when the projectile moves in the field of the target nucleus it loses energy in a continuous way thereby exciting the target, with the probability of breaking up or transferring nucleons to the target nucleus [Gad00].

The projectile breaks up more easily into fragments for which a smaller separation energy is required. For instance, the energy needed to split ^{12}C into ^{5}Li and a ^{7}Li is 26.588 MeV while the energy for splitting ^{12}C into a proton and ^{11}B is 15.96 MeV [Gad03]. So in the case of these two examples above, the separation energy favours the break up of ^{12}C into a proton and ^{11}B. The projectile loses its energy when it comes into contact with the target nucleus. These reaction mechanisms (projectile and target fragmentation) were recently further tested in the light ion reactions i.e. ^{12}C + ^{27}Al and ^{27}Al + ^{12}C [För05]. In this case the inverse reaction was important in order to study the excitation energy dependence of all possible reaction channels. In this study target and projectile fragmentation as well as nucleon coalescence were found to be dominant reaction mechanisms in the emission of IMF with masses between ^{12}C and ^{27}Al. All the reaction mechanisms mentioned above were incorporated in a code which was developed and extended at the University of Milano during the past fifteen years [Bec03], [Gad01]. In this code, projectile break-up is evaluated under the hypothesis of the Serber approximation [Ser47] and the local plane wave approximation (LPWA) [McV80], while nucleon coalescence is evaluated by solving a set of Boltzmann Master equations (BME) which give the time evolution of the occupation probability of nucleon states of the emitted composite nucleus [Cav01].

A further application of the code as well as a test of the inferred reaction mechanisms at these incident energies is the interaction of a 200 MeV ^{12}C projectile with a ^{12}C target which forms the topic of this thesis.

1.4 Motivation of this study

Studies involving the interactions of two light nuclei are still of great interest, not only for the understanding of the underlying reaction mechanisms, but also for their applications in Hadron therapy and radiation protection during space missions. As was mentioned the aim of this experiment is to extend the study of the interaction of ^{12}C with ^{27}Al [För05] at an incident energy of 13 MeV/nucleon to the ^{12}C + ^{12}C

system. The interest of the present study is therefore to further investigate the reaction mechanisms involved in the production of IMFs in very light-projectile systems and to study in particular those IMFs which are emitted with a mass heavier than the target or projectile. The purpose of this work was therefore to separate C, N and O isotopes and to measure the double differential cross sections of amongst others, positron emitters produced in these interactions. The double differential cross sections of these fragments were measured in the angular range to study the reaction mechanisms involved at forward angles and larger angles. Previous studies showed that the IMFs are most likely produced as evaporation residues in complete fusion and break-up fusion reactions.

The study of the production of these IMFs is of the utmost importance for the following two reasons. Firstly (and most importantly), to measure the yields and energy of fragments with masses greater than those of the interacting ions. These are most likely produced as evaporation residues in complete fusion and incomplete fusion reactions with relatively low energies. Secondly, the aim is to obtain information which is of use in hadron therapy. It allows to estimate the production of positron emitters like e.g. ^{11}C, ^{13}N and ^{15}O at energies very close to the Bragg peak region (BPR). Consequently, these may increase the relative biological effectiveness (RBE) of the beam in the BPR which might have been noticeably reduced due to reactions occurring along its passage through the healthy biological tissue [Paw97]. Through PET techniques these isotopes can be used and assist in visualizing the beam during irradiation and will consequently allow for a better conformation of the irradiated tumor volume.

The set-up of the experiment as well as the electronics used for data acquisition is discussed in the following chapter. In chapter 3, the procedure of the data taking and the analysis of the data are explained while the theoretical model to interpret the data is described in chapter 4. The results of the experiment together with the comparison of the experimental results and the theoretical calculations based on the completed calculations of ^{18}O and discussion are presented in chapter 5. The summary of the study and conclusions are given in chapter 6.

CHAPTER 2

Experiment

2.1 Introduction

The experiment was intended to measure angular distributions of the continuum energy spectra of Intermediate Mass fragments (IMF) with $Z \geq 6$ which were produced during the bombardment of a ^{12}C target with a 200 MeV ^{12}C beam. From the energy spectra of IMF, the double differential cross sections of IMF with a mass heavier than ^{12}C were extracted. A silicon telescope was used to measure the high energy component of the spectra at emission angles from 8° to 60°, while the low energy component of the spectra was measured with a Bragg Curve Detector (BCD) over an angular range of 15° to 60°. The BCD has a thin entrance window which allows for a low energy threshold. Hence the Si telescope was used to complement the BCD in measuring the full energy spectra. Standard ΔE-E techniques were used to obtain particle identification as well as isotope separation for most of the fragments detected in the silicon telescope. This chapter summarizes the experimental set-up as well as the electronics used to measure and process all the signals required to obtain the data.

2.2 Bragg Curve Detector

Previous studies where Bragg-curve detectors (BCD) were used showed that these detectors are able to identify isotopes from Li to Ti with an energy threshold of about 1 MeV/amu [Tan95, Och96]. This energy threshold is determined by the thickness of its entrance window and the first 2 cm of the active volume which corresponds to the size of the sampling region of the BCD (see section 2.2.1). The entrance window of the BCD must be as thin as possible so that the detector is able to identify low energy fragments. Several advantages are realized in this type of detector:

- The detector is relatively insensitive to radiation effects.

- Large solid angle is easily achieved.
- Adaptation to the energy range by changing gas pressure.
- Insensitivity to minimum-ionizing particles through the detector which does not affect the registration of other particles.

2.2.1 BCD construction

The construction of the BCD is shown in Figures 2.1 and 2.2. The entrance window consists of 1.01 μm Mylar foil coated with 0.80 μm carbon on the inside which constitutes the cathode (see Figure 2.3). The entrance window must be as thin as possible to minimize energy loss. The window was tested to withstand an inner pressure of 300 mbar. Figure 2.3 shows the entrance window of the BCD. A chain of seven field shaping rings separated by 10 MΩ resistors connected the cathode and the Frisch grid. The voltage applied to the Frisch grid was divided by these resistors and shaping rings chain thereby creating and preserving a homogeneous longitudinal electric field over the distance from the cathode to the Frisch grid within the shaping rings, which is called the active volume of the detector. The cathode was kept at zero potential. The distance between cathode and Frisch grid was 160 mm, while the gap between Frisch grid and anode was 20 mm which is called the sampling region. The Frisch grid consists of a mesh of 2 μm tungsten wires with 1 mm spacing. A circular copper disk formed the anode. The Frisch grid and anode voltages were set to +1800 V and +2500 V, respectively [Tho03]. The detector is encapsulated by a stainless steel cylinder 200 mm long and with an internal diameter of 55 mm. Gas tight BCD was achieved by employing o-rings at all opening flanges of the BCD.

2.2.2 Frisch grid

The Frisch grid defines the sampling region and is made to be as transparent as possible to the electrons. The sampling region is the gap width between Frisch grid and anode. The sampling region determines the dynamic range of particles which are identified by the BCD.

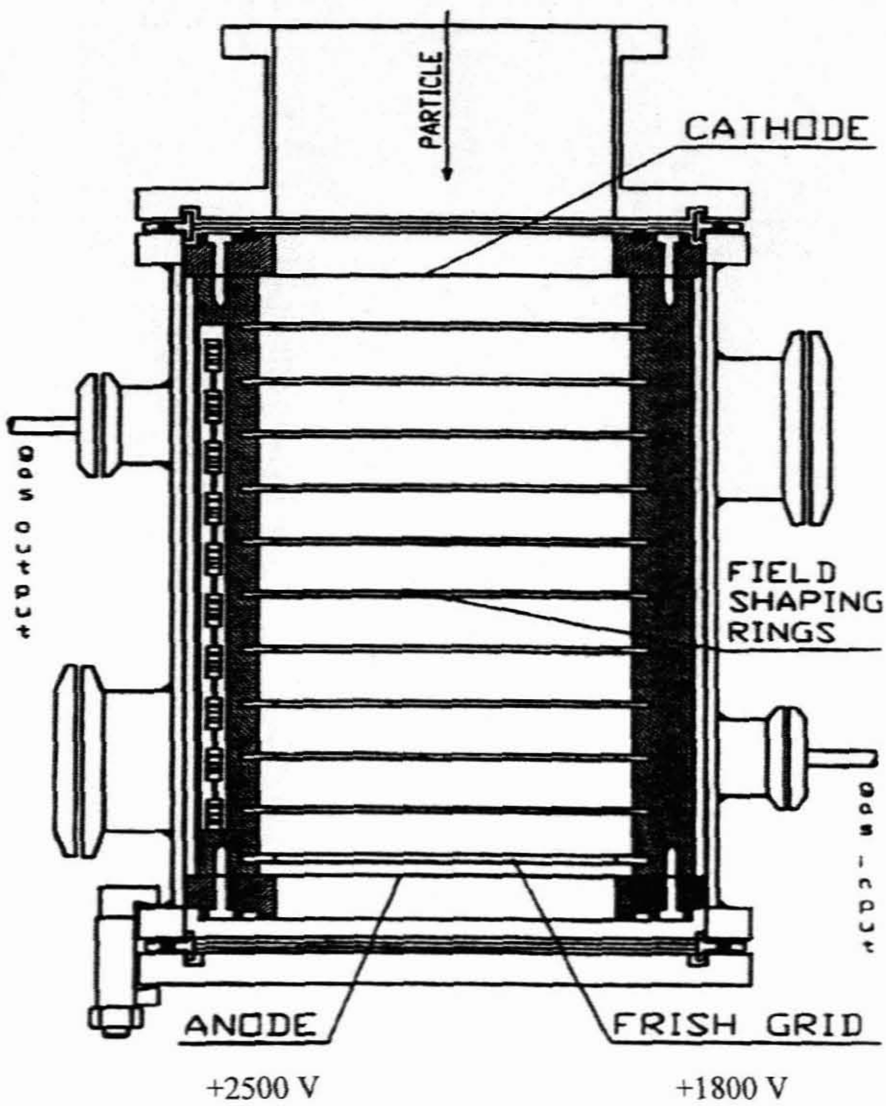

Figure 2.1: *Schematic drawing of the Bragg curve detector. The distance between the cathode and the anode was 180 mm. The internal diameter was 55 mm. The distance between the Frisch grid and anode was 20 mm.*

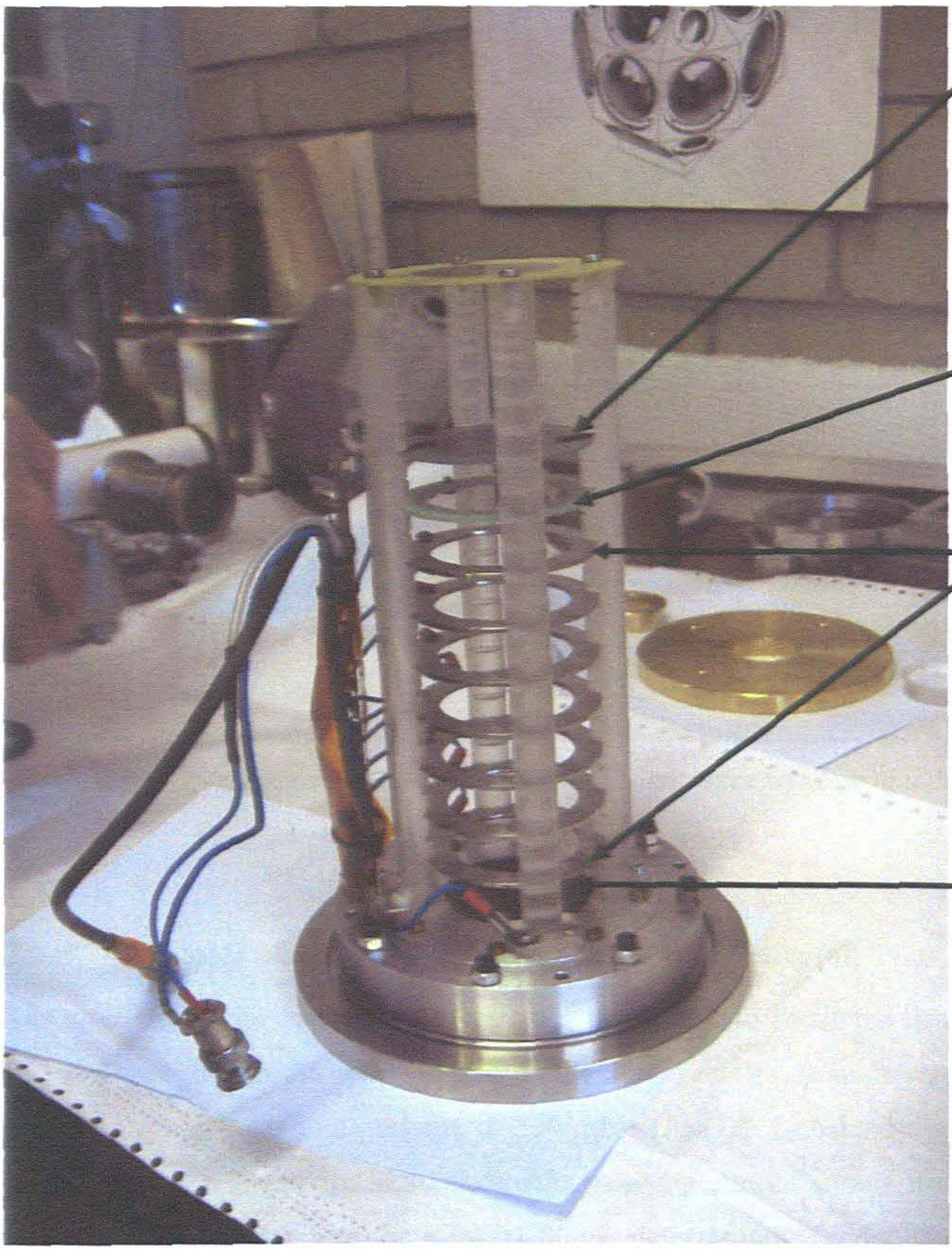

Figure 2.2: *A photo of the active volume of the BCD*

Figure 2.3: *The front part of the BCD showing the entrance window and collimator.*

2.2.3 Principles of operation of the Bragg Curve Detector

The main aim of the detector and electronics involved is to obtain the Bragg Curve of the ions that stop in the active region of the detector. The detector was filled with isobutane (C_4H_{10}) gas to a pressure of 300 mbar [Ass82]. Isobutane was chosen for the following reasons. Its high electronic stopping power allows operation at a relatively low gas pressure for a reasonable counter length. Secondly, the electron drift velocity is high and does not depend strongly on the applied reduced field in a given range. Thirdly, this large velocity limits electron combination and attachment. For good identification, the anode current must reproduce very closely the Bragg curve. Hence, the gaseous absorber quantity between the grid and anode must be small. The smaller the grid anode distance, the smaller the grid screening efficiency. So, the grid anode distance results in a compromise [Bar04].

Particles entered the detector through a carbon coated Mylar foil which constituted the cathode. As they move through the active volume of the detector they ionize the gas inside the detector creating the ion pairs. Since the energy loss per collision is very small, it increases slowly along the particle's path. Only when the remaining energy is smaller than 1 MeV/nucleon the energy loss increases rapidly forming the Bragg Peak (see Figure 2.4). Particles are stopped in the detector before reaching the Frisch grid after losing all of its kinetic energy. Based on the detector design electric field in the gas is maintained parallel to the ionization track. This causes ion pairs with negative charges to move from the cathode towards the anode while the positive charges move towards the cathode at a smaller rate.

The induced anode current is proportional only to the charge contained in the grid to anode gap and is given by [She85]

$$i(t) = \frac{v_d}{g} \int_{l}^{l+g} q^{-}(x,t)dx \tag{2.1}$$

where,

$l \cong$ drift region length

$g \cong$ grid to anode gap width

$v_d \cong$ electron drift velocity

$q^{-} \cong$ ionization charge distribution of an electron at given time

Due to the convolution operation of the Frisch grid to anode gap, the anode signal is a distorted mirror image of the original Bragg curve as shown in figures 2.4 and 2.5 [She85],[Bun47] .

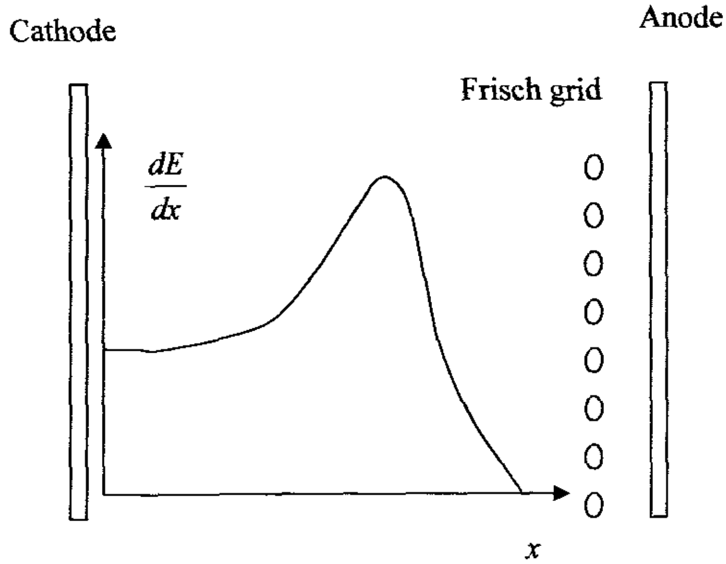

Figure 2.4: Bragg signal produced by a particle stopping in the BCD before reaching the Frisch grid.

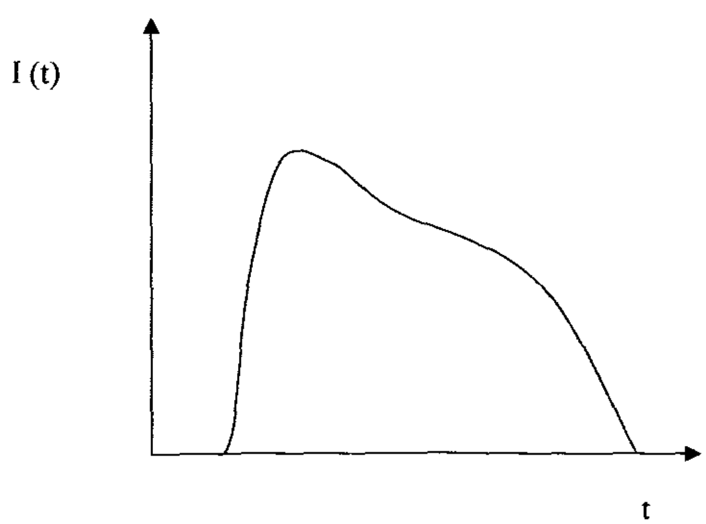

Figure 2.5: *The anode current of the BCD as function of time.*

The amplitude of the peak shown in Figure 2.5 is directly proportional to the charge of the particle thus allows identification of particle's atomic number. Integrating the area underneath the peak gives the kinetic energy of the stopped particle. Table 2.1 shows the energy range of different charged particles stopping in the active volume of isobutane at 300 mbar which is calculated with the ELOSS program [Jip84].

Table 2.1: *Table showing the energy ranges of different particles stopping in the active volume of the BCD at a pressure of about 300 mbar.*

Intermediate Mass Fragments	Energy range (MeV)
^{12}C	14-60
^{14}N	20-75
^{16}O	25-90

2.3 Silicon surface barrier detectors

Both ΔE and E detector was a charge sensitive silicon surface barrier (SSB) detector. The ΔE detector was used as a transmission detector which measured the energy lost by a charged particle passing through it. The E detector was used to measure the energy of particles deposited in the detector. Some of the characteristics of these detectors include [Mud05]:

- Thin dead layers
- Energy loss distribution function
- Surface area of the SSB
- Ability to operate at room temperature without excessive leakage current
- The means to detect bound charged particles due to low intrinsic conductivity

The thicknesses of the detectors were chosen to stop all the fragments in the E detector with $Z \geq 6$ and to have a low-energy threshold as low as possible as well as obtaining sufficient separation for the different isotopes of the fragments detected.

2.4 Experimental procedure

2.4.1 Beam energy

The separated sector cyclotron (SSC) at iThemba LABS can accelerate carbon ions up to an energy of 35 MeV/nucleon. The layout of the cyclotron facility of iThemba LABS is shown in Figure 2.6. ^{12}C ions with a charge state of +4 were generated by an Electron Cyclotron Resonance (ECR) ion source and accelerated to a few tens of keV (see Figure 2.6). Thereafter, the ions are injected into a solid pole cyclotron (SPC2) which accelerates the ions to a few MeV. From SPC2 the beam is extracted and injected into the SSC which accelerates the ions to the required energy. The 200 MeV ^{12}C beam was delivered over two weekends into the A-line vault where the experiment was performed. The beam was focused to a spot of less than a 3 mm diameter on the center of the target which was mounted at the center of the scattering chamber.

2.4.2 Scattering chamber

The 1.5 m diameter scattering chamber situated in the A-line vault has two independently movable detector arms which can be positioned at different angles with respect to the beam. At the centre of the scattering chamber a movable aluminium target ladder which can hold 5 different targets (see figure 2.7) vertically stacked above one another can be mounted. This allows the positioning of any selected target in the line of the beam. The target ladder can also be rotated to select the target angle with respect to the beam. The wall of the Scattering Chamber is equipped with various ports. There is a beam pipe connected to one side of the chamber for incoming beam and at the opposite side of the chamber the beam pipe is connected to the beam stop. Above the incoming beam pipe is a viewing port sealed with a lead glass. Through this port a closed-circuit television camera can be used to view the beam spot on a ruby target mounted on the target ladder. Other ports were used to feed through 50 Ω and 90 Ω BNC, high voltage and power supply cables for the preamplifiers. All cables were patched through to the data room. Figures 2.8 and 2.9 show a diagram and photo of the detector setup inside the scattering chamber, respectively. All the movable components inside the scattering chamber can be remotely controlled from inside the vault or from a control unit in the data room.

Before closing the scattering chamber, the o-rings were cleaned properly and greased in preparation to obtain the right vacuum condition. The chamber was pumped down to 10^{-5} mbar in the following three stages. Firstly, a rotary pump was engaged to pump the scattering chamber down to 10^{-1} mbar. Then, a turbo pump was switched on to lower the pressure to 10^{-3} mbar. Finally, a cryogenic pump was used to reach a pressure of 10^{-5} mbar. The pump down took about one and a half hours. After pumping down the chamber, the valve to the beam stopped was opened, before the

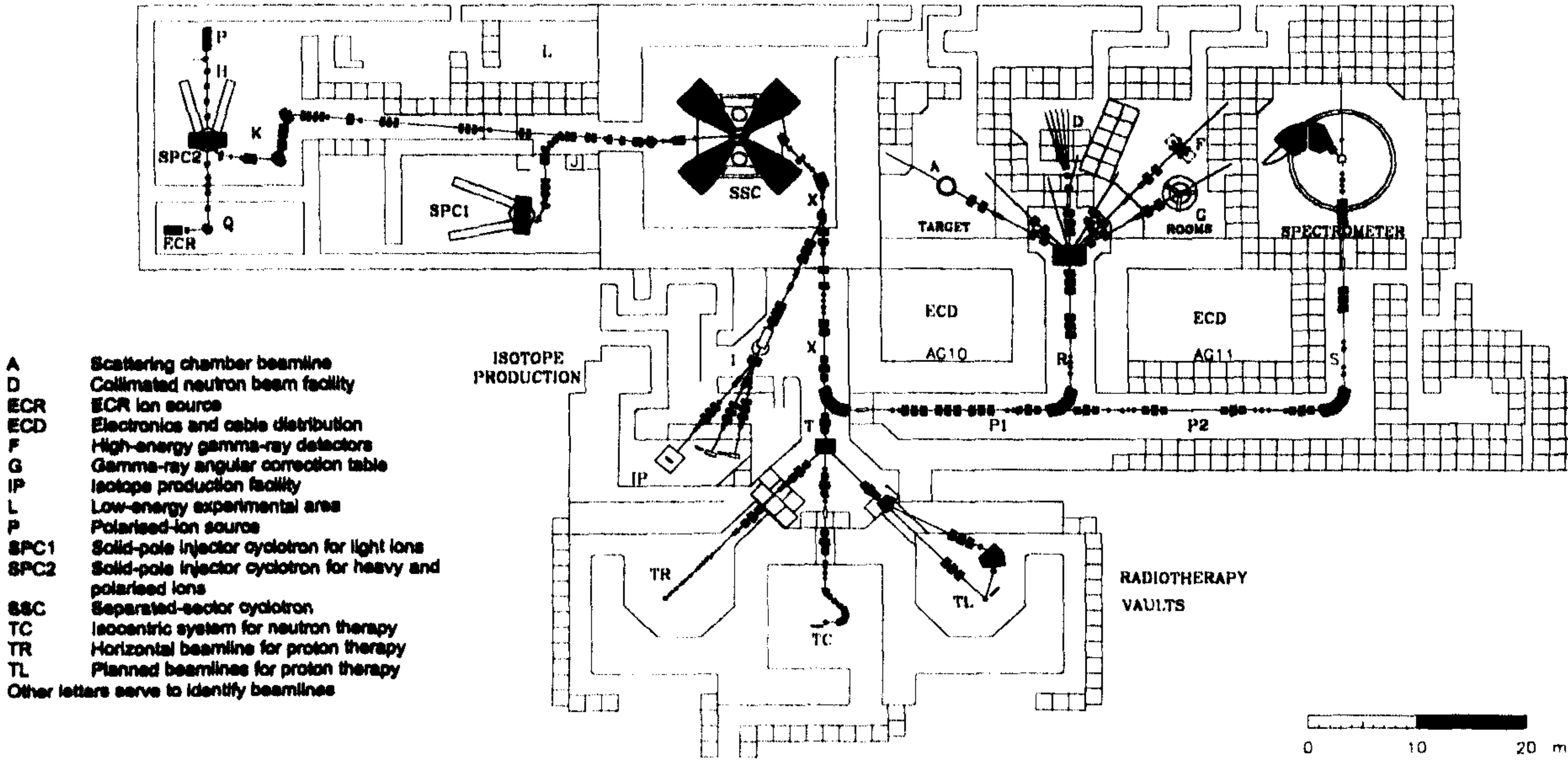

Figure 2.6: *Layout of the iThemba LABS cyclotron facility*

vault was cleared for beam. All the Si detectors used inside the chamber required a holding bias of 10% of the operating bias under vacuum in order to protect the detectors against the damage. The Si detectors as well as the BCD were fully biased as soon as beam was delivered.

2.4.3 Targets

Two ^{12}C targets of thickness 100μg/cm^2 and 1 mg/cm^2, were mounted in aluminium frames of 25 mm and 20 mm diameter, respectively. Since two ^{12}C targets were mounted in two different diameter frames two corresponding empty frames were used to monitor the beam halo. The target ladder (see figure 2.7) provided five target positions. Delta electrons which are produced in beam-target collisions are known to increase the count rate in the front detector [Nts05]. Therefore the ladder was equipped with small magnets on either side of the two ^{12}C targets to ensure that electrons were deflected away from the Si ΔE detectors. Furthermore the target ladder was also supplied with 500 V to deflect the electrons away.

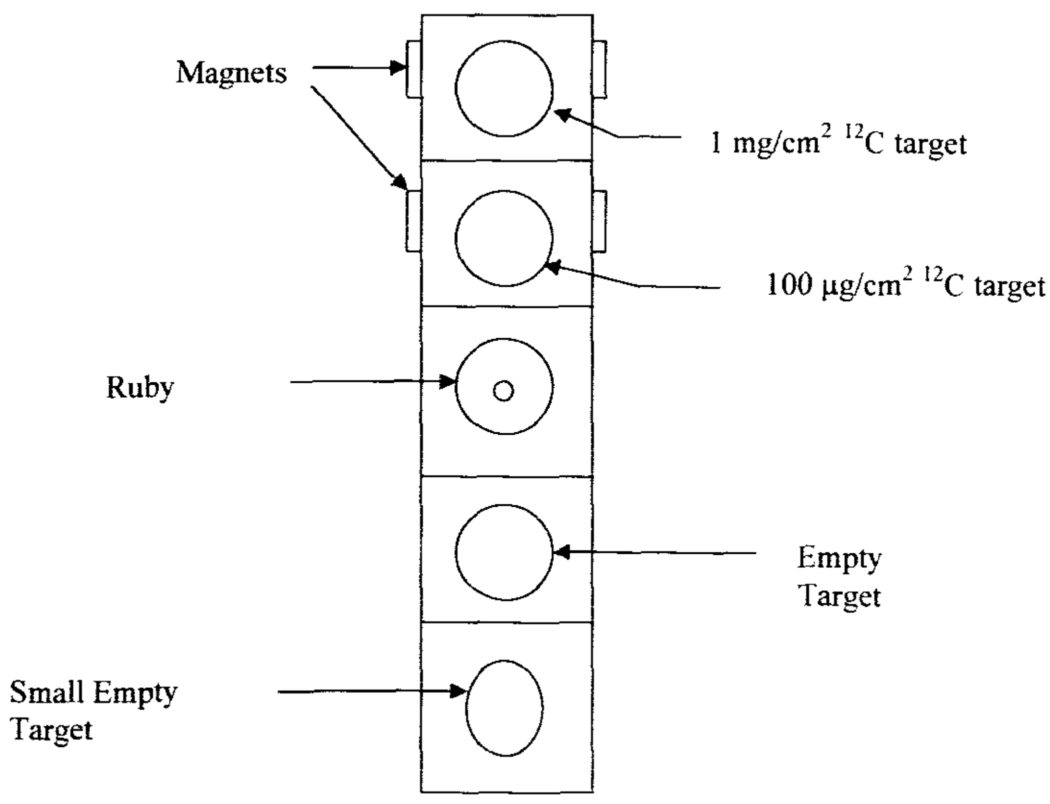

Figure 2.7: *A diagram showing the target ladder with the five target positions.*

The ruby target with a 3 mm diameter hole at the centre was used for tuning the beam and focussing the beam spot through the centre. Beam halo was monitored by comparing the count rates produced by a target run with that of an empty frame run. Typically a background of less than 10% was acceptable.

2.4.4 Setup of Detectors

The Bragg Curve Detector (BCD) and the Silicon detector telescope were each mounted on a movable arm inside the 1.5 m diameter scattering chamber (See figure 2.8). The silicon detector telescope which consisted of a 50 μm thick ΔE followed by 1000 μm thick (E) silicon surface barrier detector was mounted on one side of the scattering chamber with respect to the beam. Shielding of the silicon telescope was provided by a brass collimator which is 10 mm thick. A collimator insert of 8 mm thick with 8 mm diameter hole was fitted in the collimator hole. This insert opening was chosen to have an optimal linearity in the thickness of the ΔE detector. Thereby, the mass resolution of the detected fragments could be improved. A collimator insert of 8 mm diameter aperture defined the solid angle of the Si detector telescope to be of 1.132 ± 0.002 msr. The solid angle was calculated from the equation

$$\Delta\Omega = \frac{\pi r^2}{x^2} \tag{2.2}$$

where,

r ≅ *the radius of the collimator insert*

x ≅ *the distance from the target to the back of the collimator*

As shown in figure 2.8 the Bragg Curve Detector was mounted on the opposite side of the Si telescope. A brass collimator of 10 mm thickness was mounted in front of the BCD for shielding. The BCD was mounted at a distance of 393.67 mm from the target. A 32 mm diameter collimator insert was fitted in the diameter hole to reduce the effective collimator opening. The criterion for this was to avoid fragments hitting the shaping rings throughout the active volume of the detector. The collimator insert opening subtended a solid angle of 5.189± 0.001 msr.

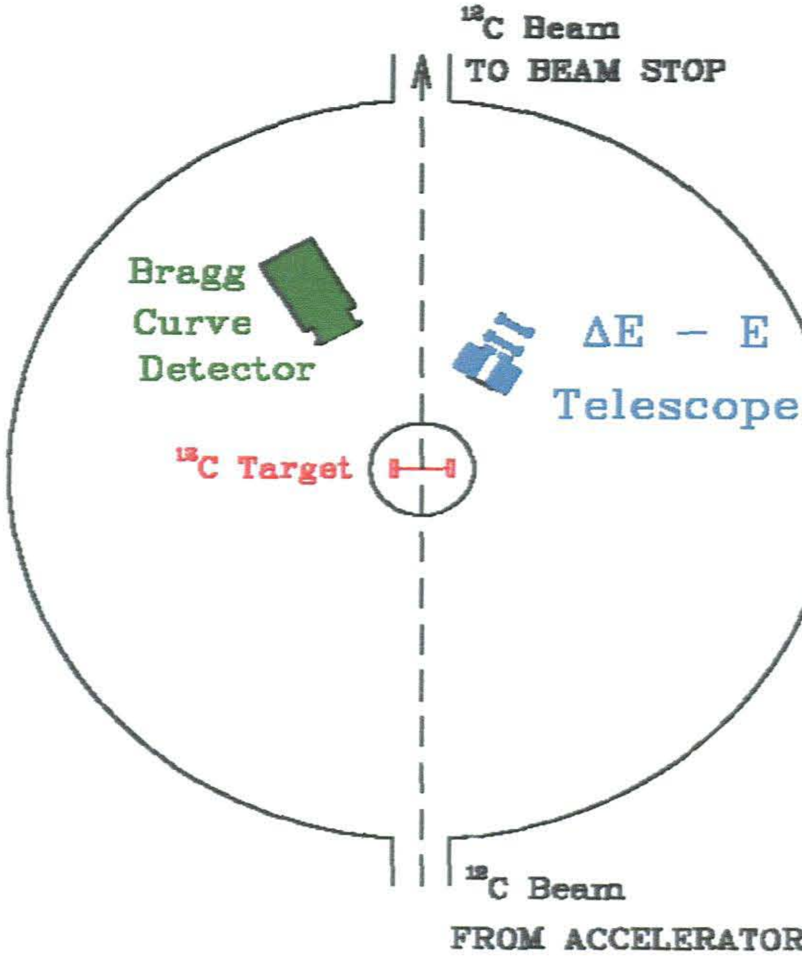

Figure 2.8: *Schematic diagram of the detectors inside the scattering chamber.*

The most forward angle which the silicon telescope could reach was 8° while BCD could reach a minimum angle of 15° relative to the beam. All the detectors were isolated from the scattering chamber to avoid noise pick-up from ground loops.

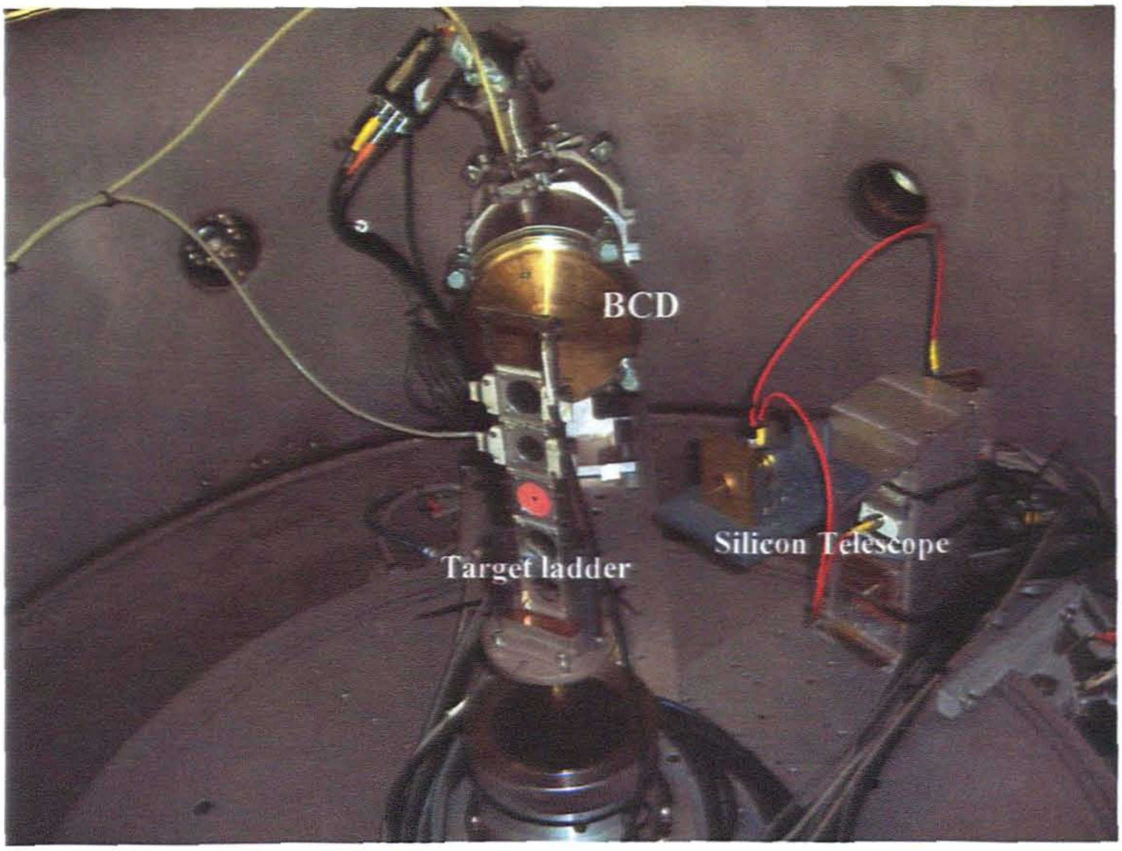

Figure 2.9: *Photo showing the experimental setup inside the scattering chamber*

2.5 Gas flow system

A crucial aspect for proper performance of the BCD is a reliable gas flow controlling system [Bar04]. Gas ageing can significantly reduce the detection efficiency of the BCD [Och96]. When the gas is not refreshed continuously, after a short time the detection efficiency drops. This is caused by the mixture into isobutane remnants of electronegative gasses, which are attached initially to the vessel walls and are hidden in the pores of various parts of the detector. Such mixtures may capture the drifting free electrons. These electrons must instead be allowed to drift over the detector length with low combination. Therefore the gas used, its pressure as well as the applied voltages have to be selected carefully.

The following procedures were followed in filling the BCD with isobutane gas. Firstly, the by-pass linking the scattering chamber to the detector was opened allowing the BCD to be at the same operating pressure as the scattering chamber. The hand throttle on the scattering chamber roughing pump was closed and then the normal pump down procedure of the scattering chamber was started. The hand throttle on the roughing pump was opened slowly in order to avoid any damage to the entrance window.

When the pressure inside the scattering chamber of about 10^{-4} mbar was reached, the by-pass was closed thereby isolating of the BCD from the scattering chamber vacuum. The roughing pump of the gas supply system was then started to allow for gas to circulate through the BCD. The gas bottle was opened to supply the gas. A needle valve as well as the supply valve on the pressure regulator control unit was opened to start the gas flow. The regulator readout of the gas pressure was expressed as a percentage of 500 mbar. For an operating pressure of the BCD of 300 mbar the regulator therefore corresponded to 60%. After the gas filling was completed, the gas regulator control unit was set to remote to be operated it in the data room. Figure 2.10 shows the gas flow controlling system used to fill the BCD with isobutane.

2.6 Electronics

This section describes the electronic set-up that was used to process the signals from the BCD preamplifier as well as the preamplifiers of the Si detector telescope.

2.6.1 Detector signals and Preamplifiers

The function of the preamplifiers is to provide an interface between the detector and pulse processing electronics, to amplify weak signals from the detectors and to shape the subsequent output pulses. Charge-sensitive preamplifiers produce fast timing and slow linear pulses [Ste97]. Therefore charge-sensitive preamplifiers amplified the signals from the anode of the BCD, silicon ΔE and silicon E detectors. All three preamplifiers were mounted inside the scattering chamber using short BNC cables and trapped to the rotating arms on which the detectors were mounted to avoid noise pick-up. While the preamplifiers of the Si telescope give out a linear as well as a timing signal, only the linear output from the BCD preamplifier was used. Two different preamplifiers were used in the case of Si telescope due to the different thicknesses of the ΔE and E detectors.

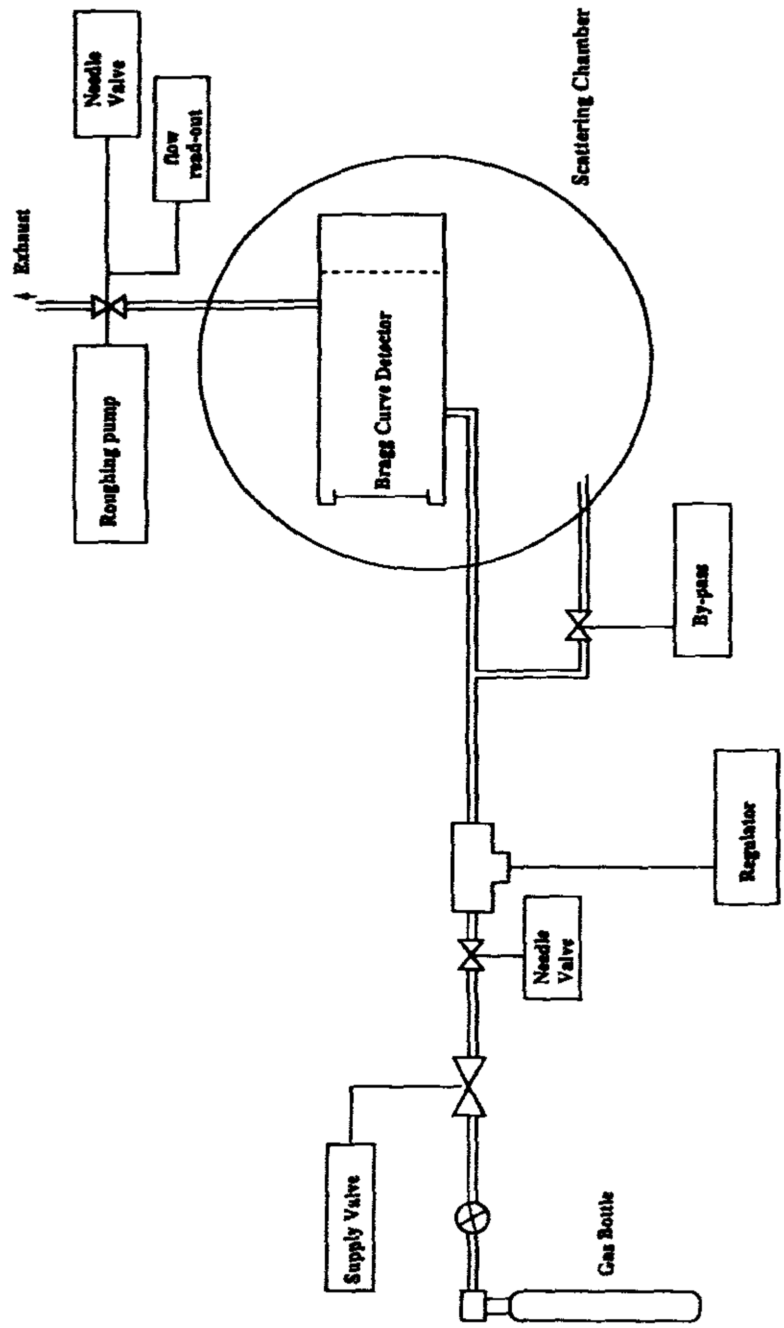

Figure 2.10: *The BCD gas filling system*

2.6.2 Linear signals of the Si detector telescope

The amplitude of a linear signal contains information about the energy and the charge of the detected particle. The linear signals from the two preamplifiers of the silicon detector telescope were transmitted to individual amplifiers in the data room using BNC 93Ω coaxial cables. The signals from each amplifier were fed to a Linear Gate and Stretcher (LGS) module to allow the linear signals to be sent to the Analog-to-Digital Converter (ADC) modules. The LGS opened the gate only for a valid event which was defined as coincidence event between the ΔE and E detectors. All the NIM modules used to process the linear signals are listed in Table 2.2. Figure 2.11 shows a schematic representation of the setup used to process the linear signals.

Table 2.2: *NIM modules used to process the linear signals of the detectors*

Module	*Model*
Charge Sensitive Preamplifier	ORTEC 142B (ΔE) CANBERRA 2003BT (E)
Linear Gate and Stretcher	EG&G ORTEC 542
Spectroscopy Amplifier	CANBERRA 2021
Analog-to-Digital Converter (ADC)	CANBERRA 8077
Gate and Delay Generator	ORTEC 416

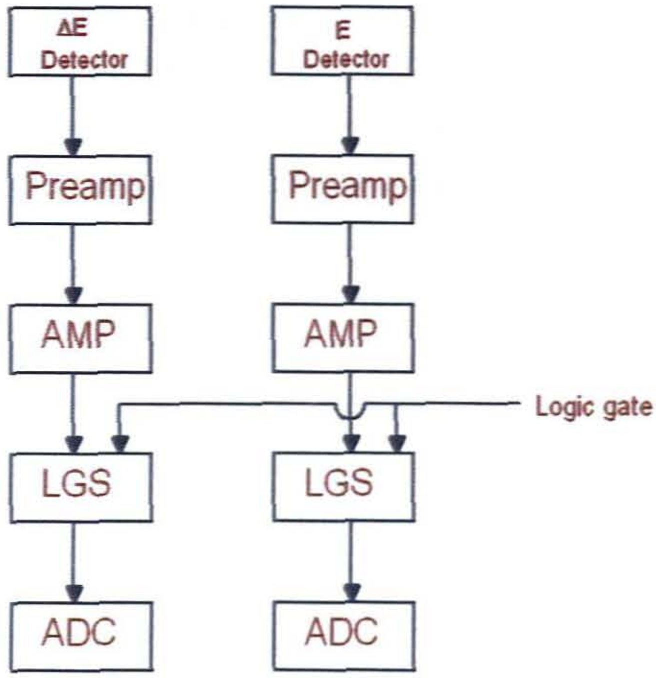

Figure 2.11: *Electronic diagram used to process the linear signals from the Silicon surface barrier detectors.*

2.6.3 BCD linear signals

The BCD preamplifier output was connected to a spectroscopy amplifier. The signal from the amplifier was sampled and digitized by a Flash ADC. The shaping time on the spectroscopy amplifier of the BCD was 0.25 μs. This was set to the minimum value of the spectroscopy amplifier in order to retain as much as possible the shape of the Bragg signal. The NIM modules that were used to process the BCD linear signals are summarized in Table 2.3. Figure 2.12 also illustrates the circuit diagram that was used to process the BCD linear signals.

Table 2.3: *The NIM modules used to process the BCD linear signals*

NIM modules	Models
Preamplifier	Built in-house
Spectroscopy Amplifier	CANBERRA 2020
Delay Amplifier	ORTEC 427A
Flash Analog-to-Digital Converter (Flash ADC)	Caen V729A

2.6.4 Logic signals of the Si detector telescope

Logic or digital signals are used to count events or provide timing information of a detected event. Logic signals have a fixed shape in order to indicate the only two possible conditions of either 0 or 1. Timing signals from the preamplifiers of the Si detectors were fed to the data room via 50 Ω BNC cables. These timing signals were shaped and amplified by the timing filter amplifier (TFA) and fed to Constant Fraction Discriminators (CFD). A CFD generated logic signals at a constant fraction of the analog peak height to produce an essentially walk-free timing signal [Leo87]. Logic signals from the CFD were fed to a 4-fold logic unit (4FLU) which was used to perform the AND operation between the ΔE and E detector.

The E-detector timing signal provided the timing reference for coincidences between the ΔE and E detector since it is more stable not as sensitive to noise as compared to the ΔE detector. For every coincidence that occurred, the corresponding logic pulse was fanned out to the GDG, a level adaptor, and a discriminator. The output signals from GDG were fed to LGS to open the gates. The discriminator outputs were fed to the scaler, and after being delayed also triggered both the event trigger as well as the strobe of the pattern register. The NIM modules used to process the Si logic signals are listed in Table 2.4. Figure 2.13 shows the block diagram for the setup used to process the Si logic signals.

Table 2.4: *NIM modules used to process logic signals of Si detectors*

Module	Model
Timing Filter Amplifier (TFA)	ORTEC 474
Constant Fraction Discriminator (CFD)	EG&G ORTEC 934
4 Fold Logic Unit (4FLU)	Le Croy 365AL
Discriminator (DISC)	ORTEC 436
Logic fan-in-out (FAN)	Le Croy Model 428F
Timer	ORTEC 719
Level Adaptor (LA)	
Gate and Delay Generator (GDG)	ORTEC 416A
QUAD Discriminator	Le Croy 821

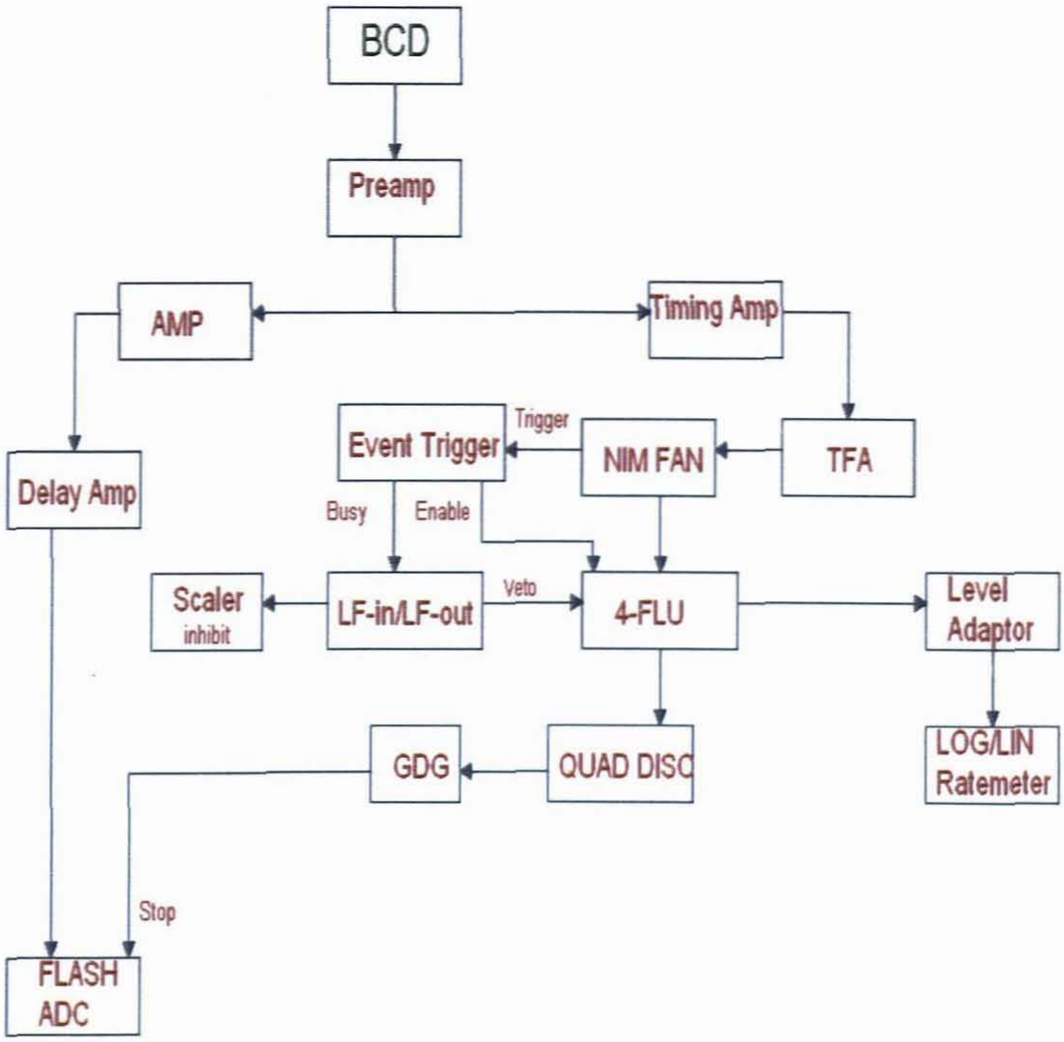

Figure 2.12: *Block diagram used to process the BCD signals*

2.6.5 BCD logic signal

The linear signal from the preamplier of the BCD was teed off at the input of the amplifier to produce both a linear as well as a timing signal. The timing signal was amplified and shaped by a timing amplifier before being fed to a timing filter amplifier (TFA). The event trigger module sends out an enable signal to a 4FLU while it is not busy. The 4FLU performed the AND operation between the enable signal and

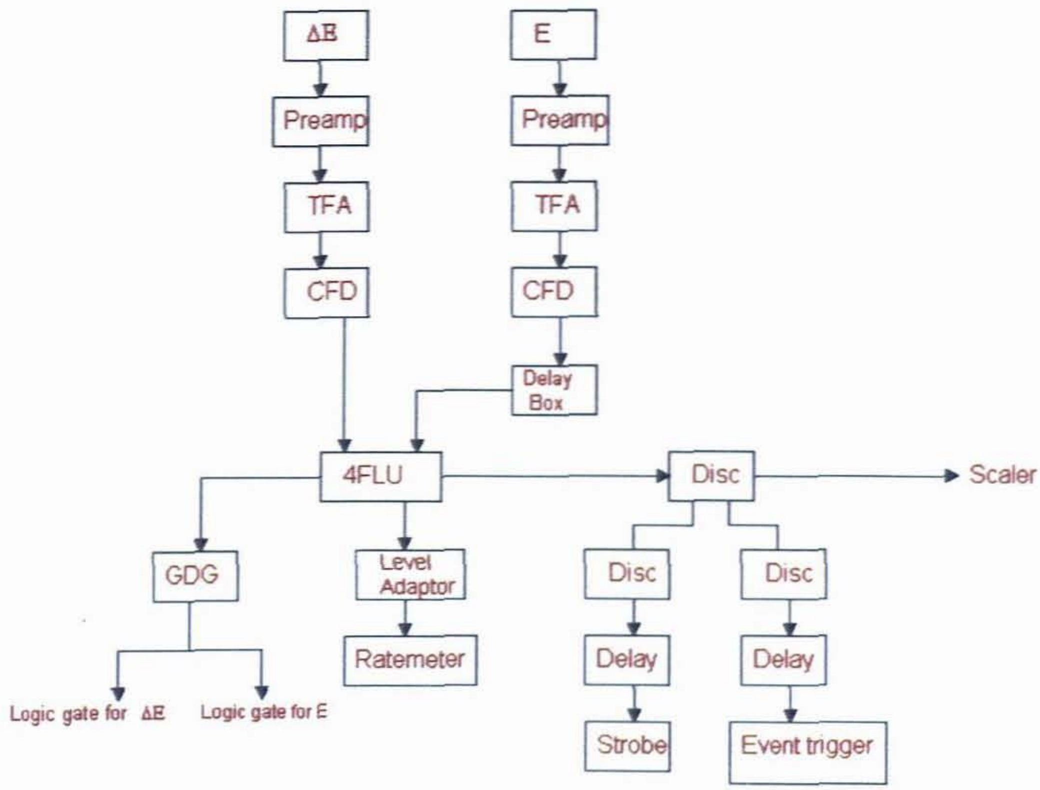

Figure 2.13: *Block diagram used to process the Si logic signals*

the timing signal of the BCD to generate a logic signal that was used as a stop signal. This stop signal was fed through a GDG to delay the stop signal such that it arrives 1 to 2 μs after the end of the Bragg signal as shown in figure 2.14. An event trigger provided a busy signal which was split by a logic fan to inhibit the scaler and veto the AND operation. This meant that all the signals arriving at the 4FLU in coincidence with the busy signal were discarded. The NIM modules used to process the BCD logic signals are the same as the ones listed in Table 2.4. The stop signal was set to be a negative logic signal with a width of 400 ns. Upon the arrival of the stop signal at the flash Analog-to-Digital Converter (FADC) the FADC sampled and digitized the Bragg signal into 200 samples at a sampling rate of 10 MHz. Hence, up to 20 μs wide Bragg signals could be sampled and digitized by the FADC. The schematic representation of the setup of the electronics used to process all the BCD signals are shown in Figure 2.12.

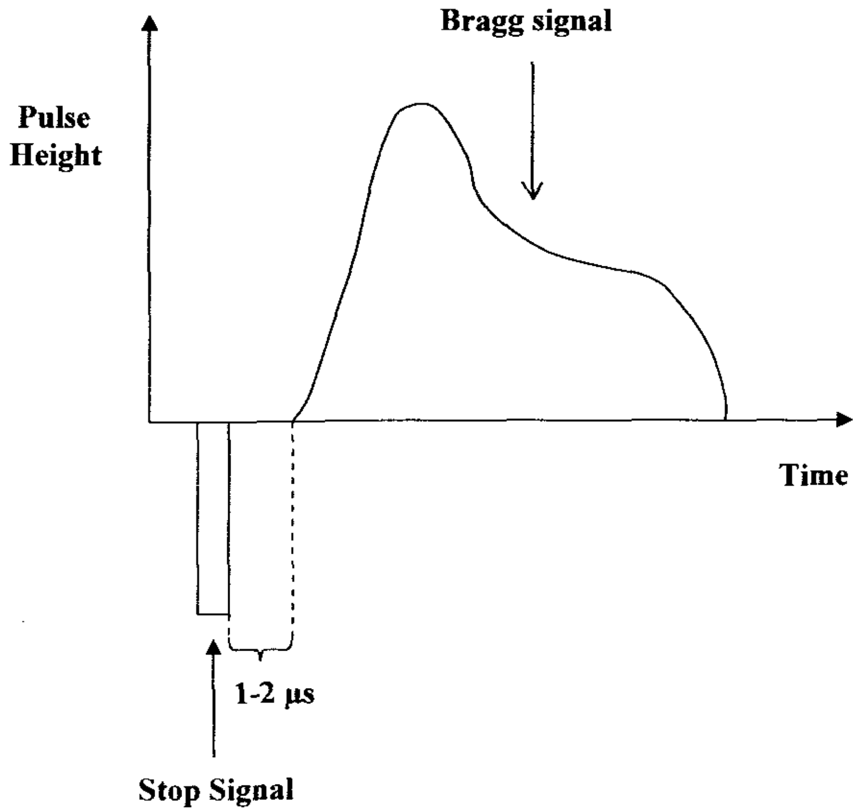

Figure 2.14: *The Setting of the Stop signal with regard to the Bragg signal.*

2.6.6 Current integrator

In order to measure the ^{12}C beam current, the beam stop was connected to the Brookhaven Instruments Current integrator (BIC 1000C) module. This module allowed selection of the current integrator range which determines the number of pulses output for every unit of accumulated charge. It also provided digital output pulses with a width of 5 μs. These pulses triggered the scalars and pulser as described in the next sections.

2.6.7 Event trigger

An event trigger is the logic signal generated by the timing logic which informs the data acquisition program that an event had occurred and initiates the event readout cycle. The event trigger was assigned with event 0 for the BCD and event 1 for the Si detector telescope through individual event trigger modules. This trigger signal enters the computer via a CAMAC module.

2.6.8 Pattern register

In this experiment the pattern register was only set up for events belonging to event 1. The function of the pattern register is to register the type of event. To register the event, the timing signals were fed into a pattern register. This input signal was stretched using a discriminator module and delayed using a delay box. The arrival of the delayed strobe signal initiated the readout of the register. Pattern register is read-out for every accepted event. Table 2.5 lists the two inputs definitions for the pattern register.

Table 2.5: *Scaler and pattern register input definitions*

Scalers		Bit	Pattern Register
Uninhibited	Inhibited		
Telescope	Telescope	1	Telescope
Pulser trigger	Pulser trigger	2	Pulser
Clock	Clock	3	-
Current integrator	Current integrator	4	-
BCD	BCD	5	-

2.6.9 Computer busy

When the event trigger signal is received by the computer, the event trigger module provides the computer busy signal to inhibit any further triggers. The computer busy signal is fanned out to veto all logic operations, block the LGS gates and to inhibit the scalers.

2.6.10 Clock

A Timer with stop output connected to start input was fed into a timing single channel analyzer (TSCA). The output from the TSCA was fed to a CAMAC inhibited and uninhibited scaler module via a discriminator. By comparing the uninhibited and inhibited scaler readings during data acquisition, an estimate of the computer dead time could be made.

2.6.11 Pulsers

The output of the current integrator (BIC model 1000C) was fed to a timing single channel analyzer (TSCA) from which the positive output was fed to a constantly running timer. The timer acted as a prescaler which provided prescaled signals to gate and delay generator (GDG). The GDG externally triggered the pulse generators which generated pulser signals for the pulsers in the ΔE and E detectors via the test inputs of the charge sensitive preamplifiers. To monitor the electronic dead time, pulsers were generated at a rate proportional to the beam current by means of an output signal from the current integrator as explained in subsection 2.5.4. The output from the pulse generator was fed through a TSCA of which the output was fed to a discriminator and pattern register via GDG (see figure 2.15). Discriminator outputs were fed to inhibited and uninhibited scalers.

The negative output from the TSCA was fed through a discriminator to an uninhibited scaler as well as a scaler inhibited by the computer busy signal. The inhibited scaler was used to determine the electronic dead time by taking the ratio between the number of pulser events recorded in the inhibited scaler and the number of counts in the pulser peak as observed in the pulser spectrum.

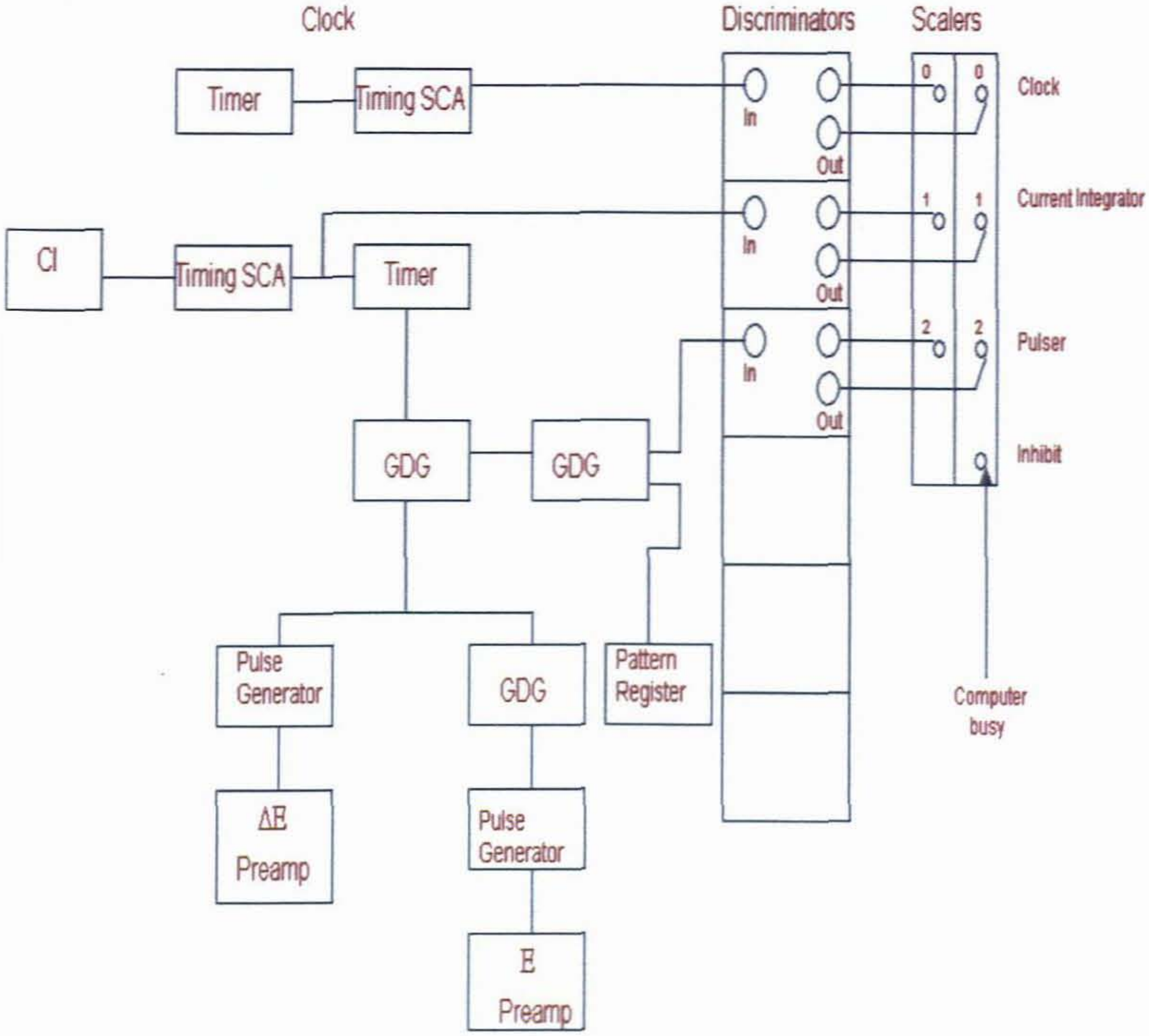

Figure 2.15: *The block diagram used to measure the electronic dead time and the beam current.*

2.6.12 Scalers

The function of the scalers is simply to count the number of a specific event (see figure 2.15). One of these scaler modules was inhibited by the computer busy signal (see table 2.5 for a list of all the scalers).

CHAPTER 3

Data analysis

3.1 Introduction

Prior to data talking, the electronic setup was tested by observing all detector signals on the oscilloscope. Both the linear and the timing signals were tuned. The events from the Si ΔE detector were set to be in coincidence with the events from Si E detector (event 1), while events from the BCD (event 0) were processed separately. After confirming whether the electronic setup handled the signals correctly, further steps were taken to extract the double differential cross sections of different isotopes produced for each fragment with $6 \leq Z \leq 8$.

3.2 Data acquisition programs

The XSYS software system was used for the online data acquisition and offline analysis. XSYS runs under VMS/VAX implementation of the event analysis language for all data sorting [Gou83]. By undergoing the following steps the online data acquisition was started:

- Run XSYS
- Load VME file
- Load Com file
- Load EVAL file

The VME files are CAMAC and sub process control files which are used for general sub process control information provided to the computer system for the data acquisition. The subprocess XSORT [Pil96] reads the Com file and EVAL file that activate the sorting process. The com file defines all the data areas for the histograms and gates that are used in the EVAL file. The EVAL programme is an event analysis language for sorting data either online or during event-by-event read back from disk or tape. The EVAL file contains the sorting algorithms that sort the events and increment the spectra. The event-by-event data are also stored in event files for offline replay.

3.3 Online data taking

As soon as the beam was delivered to the scattering chamber and aligned onto the ^{12}C 100 $\mu g/cm^2$ thick target, the signals from the detectors were processed by the electronic setup as described in the previous chapter. Next, the data acquisition as explained in section 3.2 was started. Once XSYS was running, the Particle Identification (PID) spectra of the BCD and Si telescope were inspected. Beam halo was monitored by comparing the number of counts per second detected in both the BCD and the Si telescope by using a target and an empty target frame. A background of not more than 10% was accepted before starting to take data. Good mass resolution in the PID spectrum was improved by optimizing the shaping time on the spectroscopy amplifier of the E and ΔE detectors. Different isotopes of elements or fragments could be resolved with the Si telescope while the BCD could resolve only the different charges.

The experimental data was acquired by taking data runs each lasting for one hour. Data runs of empty target frame were acquired for a period of about five minutes. These runs were performed before and after changing the detector angles. The BCD covered the angular range from 15° to 60° while the Si telescope covered the range from 8° and up to 45°. During the measurements, the pressure inside the BCD was monitored on a regular basis and was kept at 300 mbar. The data for an incident energy of 200 MeV were taken over two weekends.

3.4 Energy calibrations

In this section the procedure of the energy calibrations of both Si detectors as well as the BCD is described.

3.4.1 Si (ΔE) detector

The energy loss for different carbon isotopes in the 57.6 μm thick ΔE and 1011 μm thick E detector was calculated using the ELOSS program [Jip84]. The ΔE detector was calibrated differently from the E detector since it was not thick enough to stop the alpha particles from a ^{228}Th source. The calculated carbon isotopes loci were fitted to the corresponding experimental carbon isotopes loci in a particle identification (PID) spectrum by multiplying the calculated ΔE energy loss by a certain factor. Figure 3.1 shows the Si PID spectrum fitted with the calculated loci of ^{10}C, ^{12}C, ^{13}C and ^{14}C. This factor was taken as the gradient of the calibration of the Si (ΔE) detector. The factors for the E detector were obtained from an individual calibration described in the next section.

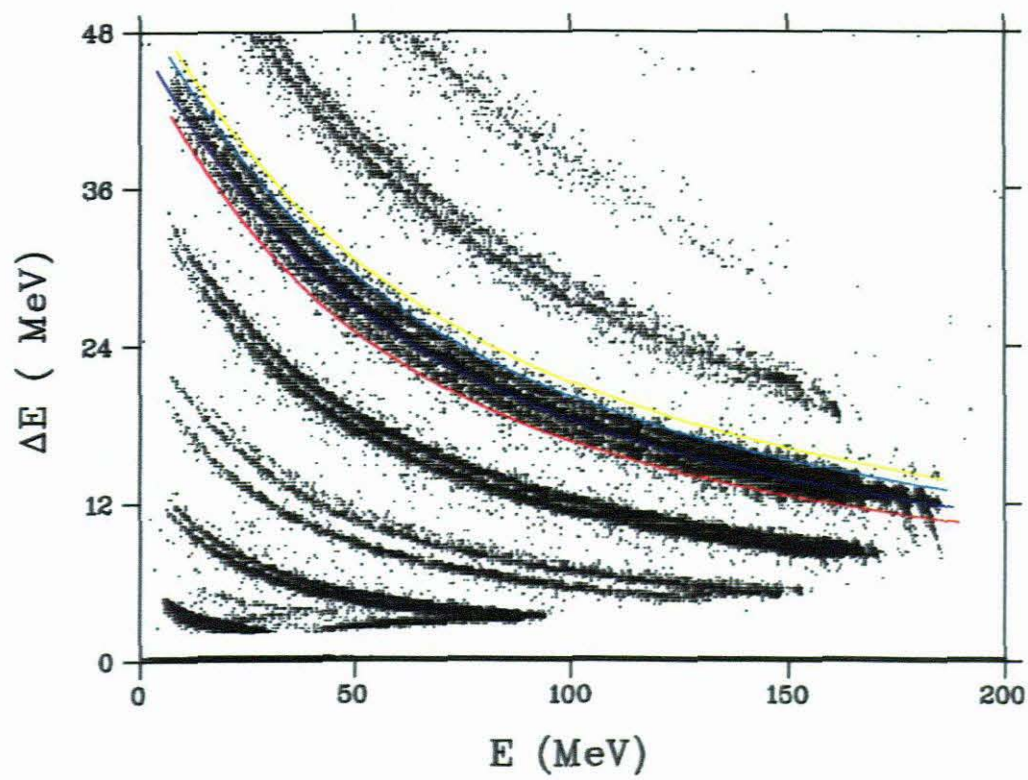

Figure 3.1: *The Si PID spectrum fitted with calculated ^{10}C (red line), ^{12}C (blue line), ^{13}C (green) and ^{14}C (yellow line) loci using ELOSS program.*

3.4.2 Si (E) detector

The 1011 μm thick Si detector was calibrated under vacuum using alphas emitted from a ^{228}Th source in a the scattering chamber. A ^{228}Th source was placed in front of the E detector. Due to the Si detector thickness, all the alphas were stopped in the detector. Figure 3.2 shows the energy spectrum of the alphas stopped in the detector. All the peaks in this spectrum were identified together with their corresponding

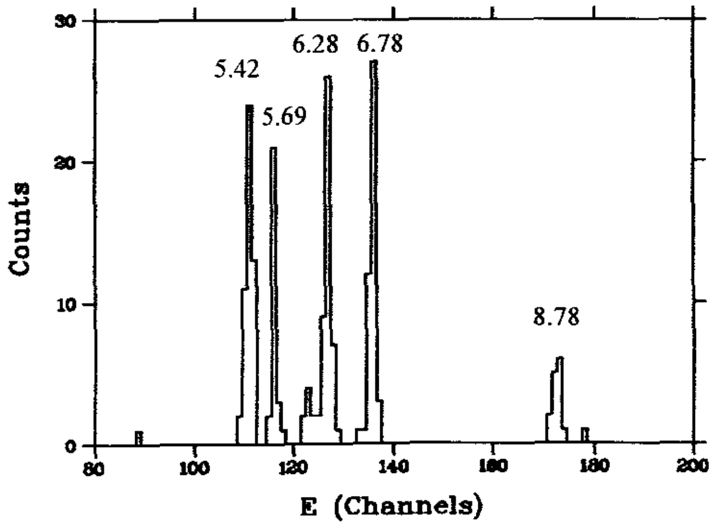

Figure 3.2: *The energy spectrum of the alpha particles stopped in 1011μm Si E detector.*

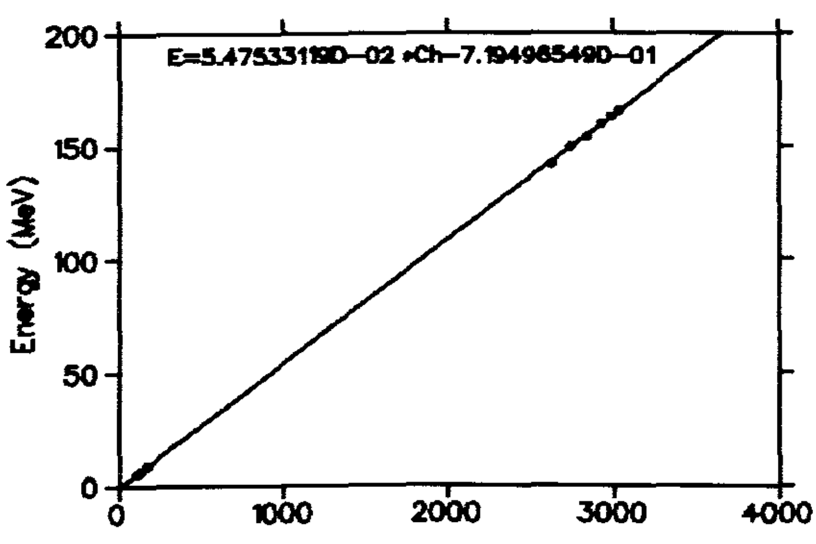

Figure 3.3: *A calibration curve for the 1011μm Si E detector given by a straight line fit through the energy values and the corresponding alpha peaks.*

energies (in MeV). The plot of the channel numbers against the corresponding energies of the peaks yielded the calibration curve as shown in Figure 3.3. This linear relationship gives the gradient and the offset parameters of the detector. The energy calibration was confirmed by comparing the energy of the ground state peak of the detected particles to the calculated energy values using KINMAT program.

3.4.3 BCD detector

The energy calibration of the BCD was performed using alphas emitted from a ^{228}Th source. The ^{228}Th source was placed in front of the cathode of the BCD. The gated α energy spectrum is shown in Figure 3.4. The BCD could only fully resolve the 8.78 MeV energy peak. The corresponding channel number of the 8.78 MeV energy peak was identified. The gradient and offset of the detector was determined by the linear relationship between this channel number and the energy as shown in Figure 3.5.

The energy loss by the alpha particles in the entrance window were corrected for by identifying the energy from the spectra as shown in figure 3.4 as the same energy from the original source spectrum. The energy calibration was then confirmed by comparing the energy spectra of different species and their maximum energy loss calculated by the program ELOSS [Jip84].

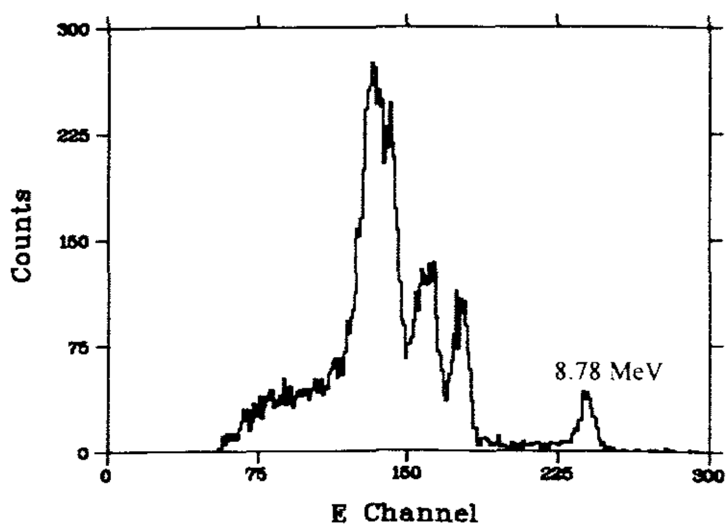

Figure 3.4: *Energy spectrum for the alpha particles from a* ^{228}Th *source measured with the BCD.*

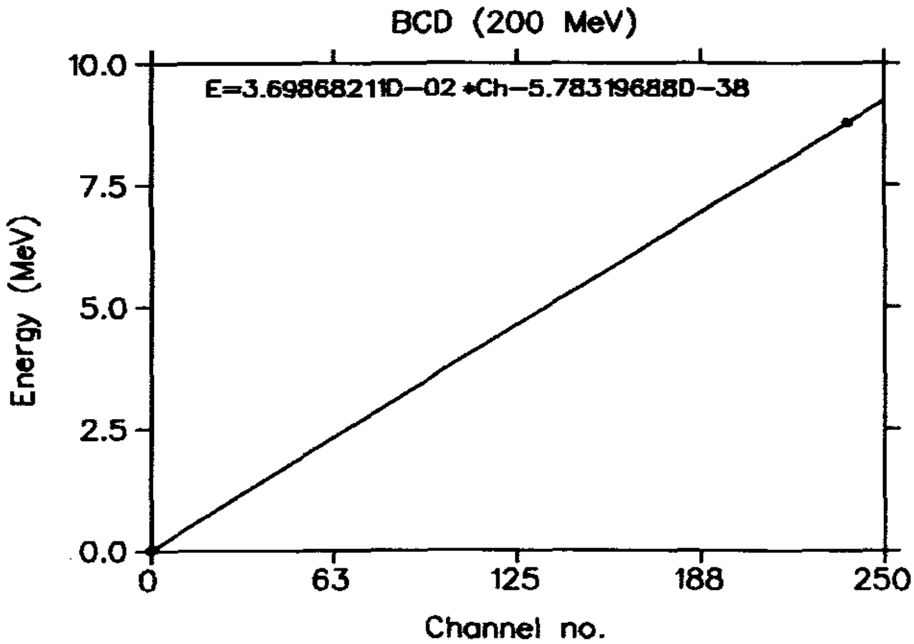

Figure 3.5: *Calibration fit of the resolved 8.78 MeV peak with the corresponding channel number.*

3.5 Replay

The main objective during data replay was to extract the angular distributions of the energy spectra of C, N, and O isotopes as measured with the Si telescope as well as the low energy spectra of fragments as detected by the BCD. The off-line replay of the data was based on the same XSYS software used in data acquisition as discussed in section 3.2. The COM and EVAL files were modified accordingly by adding data areas and gates.

3.6 Particle identification

The ΔE-E technique and Bragg peak against energy were employed to separate types of charged particles of interest detected with the Si detector telescope and the BCD, respectively. Both these techniques were applied to obtain the PID spectra for each detector. These techniques will be described in the following two sections.

3.6.1 Si telescope

Standard ΔE-E techniques were used to obtain particle identification as well as isotope separation for most of the fragments detected in the silicon detector telescope as shown in Figure 3.6. All loci were well separated from each other. The fragment loci in the PID spectrum were identified by the fact that ^{8}Be is unbound and cannot survive a violent final-state interaction without destroying the correlation between its two constituent α particles [Ste05]. The various fragment loci were deduced from the beryllium loci consisting of ^{7}Be and ^{9}Be, which were well separated. In the PID spectrum of the Si detector telescope 2-dimensional gates were set around the loci corresponding to C, N and O fragments as shown in Figure 3.6. From these gated loci, the mass functions were generated for each locus to separate different isotopes of C, N and O by applying the following formula [Mud05]

$$MF = \left[(E_B + E_A)^P - (E_A)^P \right] \times M_S + M_O \tag{3.1}$$

where,

$E_B \cong$ energy deposited in E detector

$E_A \cong$ energy lost in ΔE detector

$P \cong$ constant,

$M_S \cong$ is a slope factor and was used to optimize the position of the loci in the Mass function spectra.

$M_O \cong$ is an offset factor and was used to optimize the position of the loci in the Mass function spectra.

The parameters used in generating the Mass function spectra for C, N, and O are listed in table 3.1.

Table 3.1: *The parameters used in generating the mass function spectra.*

Fragments	M_s	M_o	P
Carbon	2.0	-1600.0	1.75
Nitrogen	1.8	-1700.0	1.7
Oxygen	1.35	-1900.0	1.7

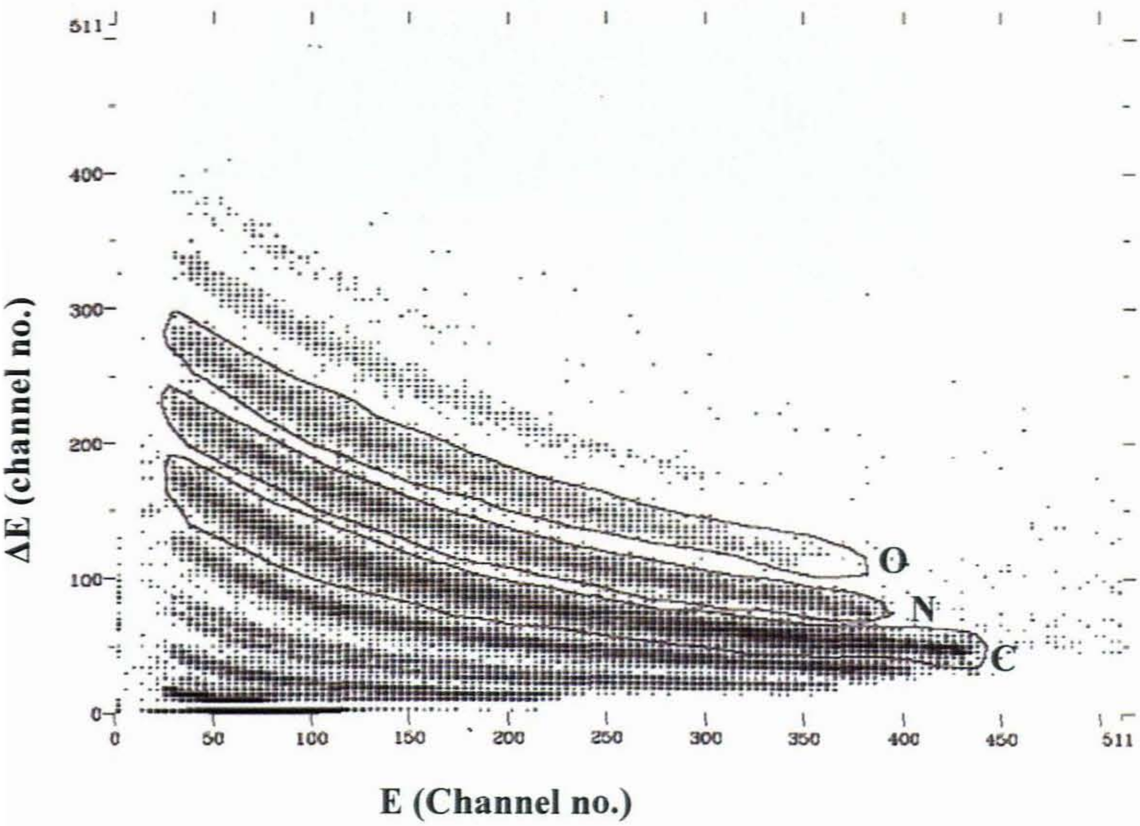

Figure 3.6: *Silicon detector telescope PID spectrum showing the gates set around carbon, nitrogen and oxygen locus, respectively. These fragments are emitted in the interaction of* ^{12}C *with* ^{12}C *at an incident energy of 200 MeV.*

From the events in the carbon, nitrogen and oxygen loci (see figure 3.6), mass functions were generated to separate the isotopes of each element. Gates on the Mass Functions had to be set with great care such that the events from pile-up events were excluded. From the gated Mass Functions, energy spectra of the selected isotopes were generated. The gates around the different isotopes of carbon, nitrogen and oxygen in the Mass Function spectra are shown in Figures 3.7, 3.8 and 3.9.

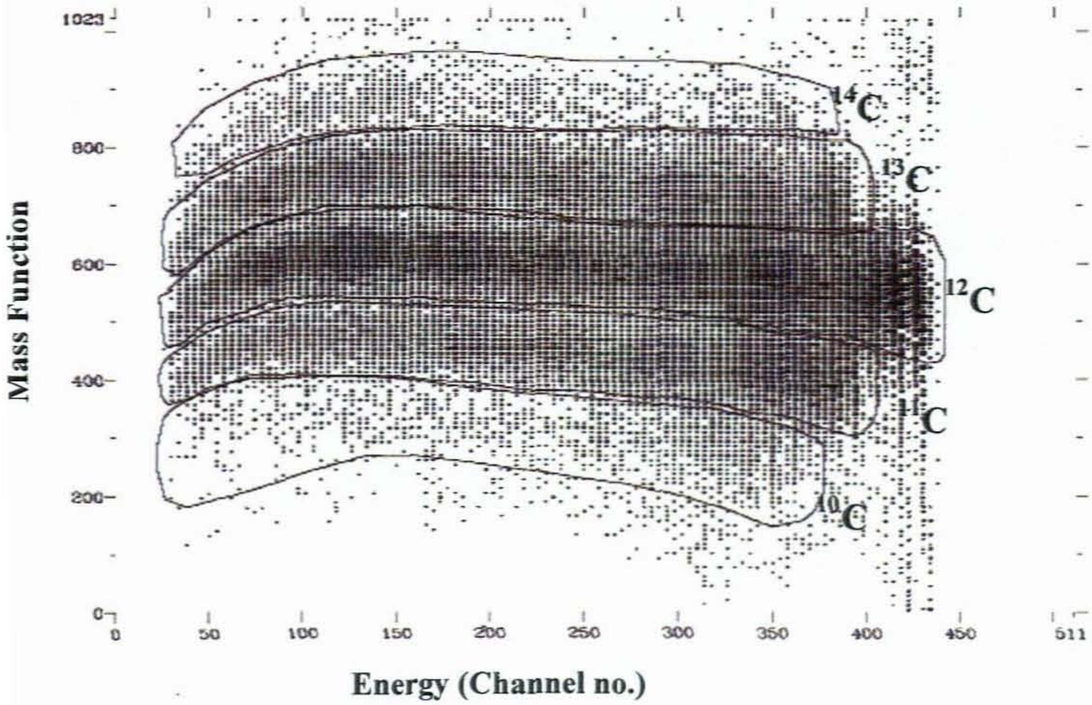

Figure 3.7: *Mass Function spectrum showing the gates set around the different carbon isotopes. The isotopes shown in the figure were emitted in the interaction of ^{12}C with ^{12}C at an incident energy of 200 MeV.*

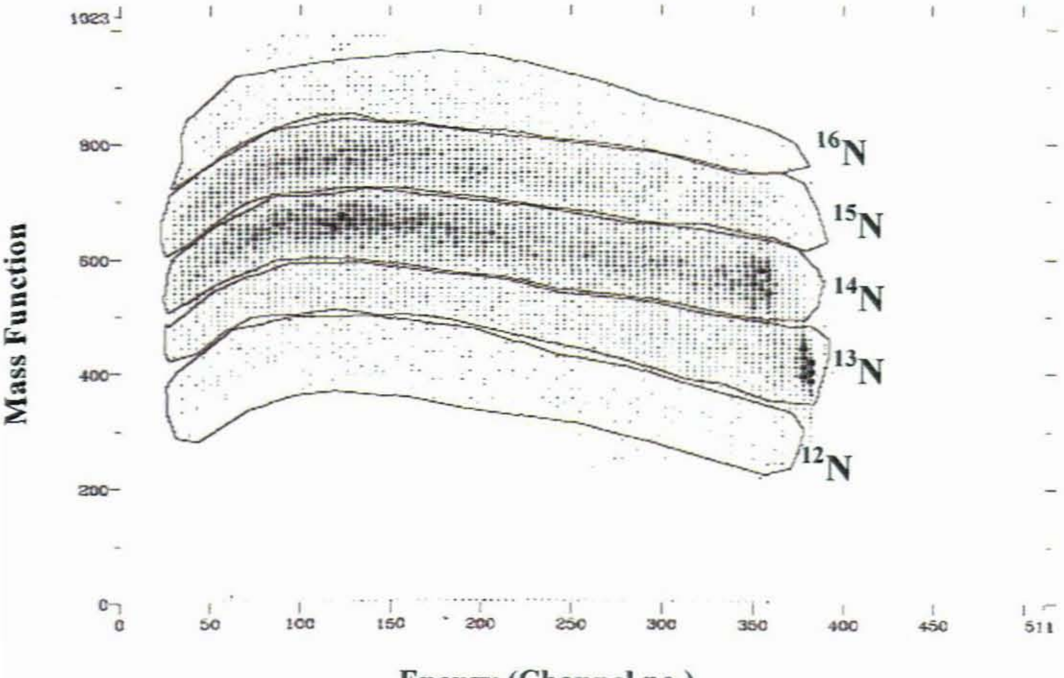

Figure 3.8: *Mass Function spectrum showing the gates set around the different nitrogen isotopes. The isotopes shown in the figure were emitted in the interaction of ^{12}C with ^{12}C at an incident energy of 200 MeV.*

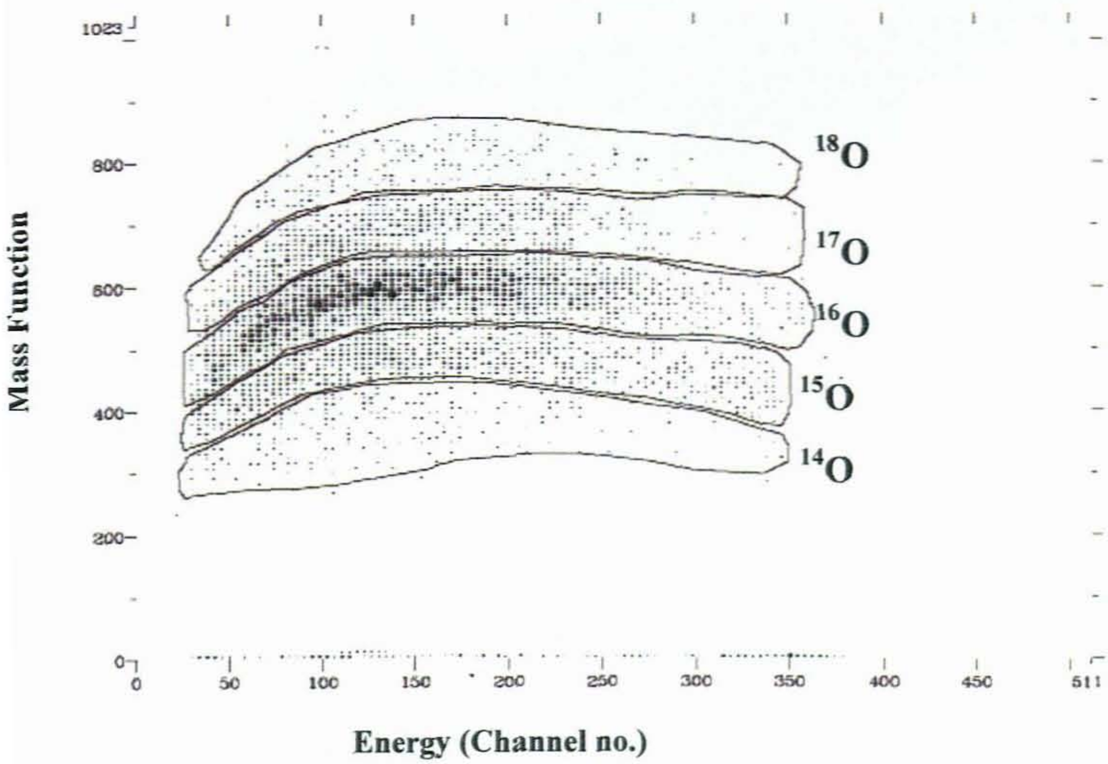

Figure 3.9: *Mass Function spectrum showing the gates set around the different oxygen isotopes. The isotopes shown in the figure were emitted in the interaction of ^{12}C with ^{12}C at an incident energy of 200 MeV.*

3.6.2 BCD

Particle identification with the BCD was performed in the standard way by displaying Bragg peak against the energy of the registered particle [And92]. The maximum amplitude of the Bragg signals (Bragg peak) corresponding to the maximum energy loss is a direct measure of the nuclear charge of the particle. By integrating the area under the pulse shown in figure 2.5 gives the total energy of the registered particle. Figure 3.10 shows the BCD PID spectrum where the different loci in the spectrum correspond to Z of the mass fragments in the range of $2 \leq Z \leq 10$. The charge of different fragments was also identified as mentioned in subsection 3.6.1. At the higher energies of some loci tailing effects in the energy spectra were observed. These effects were caused either by protons and alphas punching through the BCD or by the

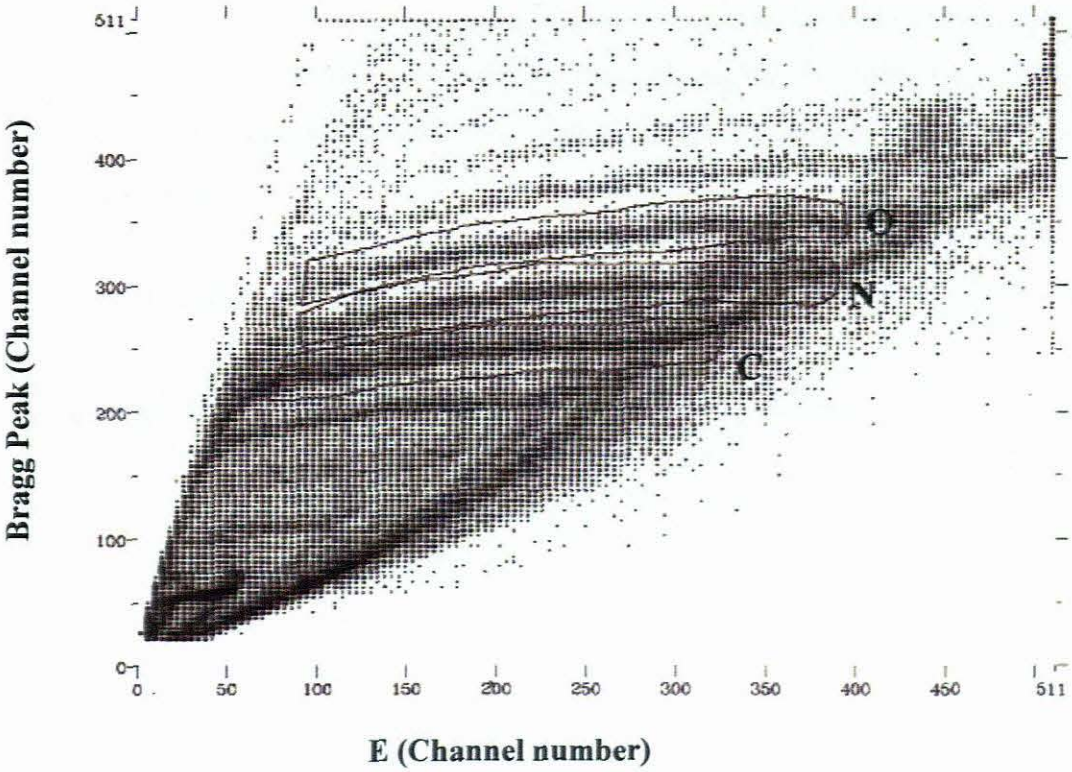

Figure 3.10: *Typical BCD PID spectrum showing the gates set around the fragments of Carbon, Nitrogen and Oxygen emitted in the interaction of* ^{12}C *with* ^{12}C *at an incident energy of 200 MeV.*

fold back of lower lying loci. The events which contaminated these parts of the loci of interest were either corrected for or lead to the exclusion of that part of the spectrum.

3.7 Background subtraction

In order to determine the amount of background, corresponding spectra were recorded using the empty frame target. The amount of background was generally about 10% at the forward angles and less than 5% at the larger angles. The background spectra were analyzed in the same manner as the target spectra. For a background subtraction, the charge of an empty run was normalized to the same charge as that of the target run so that the background could be subtracted appropriately. Background subtractions affected mostly the Si telescope data. Due to excessive background at forward angles for some data runs which affected mostly the carbon locus, not all carbon isotopes were analyzed as shown in the overview of all the isotopes analyzed which is presented in table 3.2. As the emission angle increases the yield of the fragments drop rapidly especially for the heavier fragments. The statistics for oxygen as from 25°

were very poor which meant that the different isotopes could not always be separated. In the case of the while for nitrogen isotopes this applied to angles larger than 35°. Therefore, as from these angles there were no data were extracted for the oxygen and nitrogen isotopes.

Table 3.2: *The analyzed angular distribution of the isotopes of carbon, nitrogen and oxygen.*

Angle	Carbon isotopes	Nitrogen isotopes	Oxygen isotopes
8°	^{10}C, ^{11}C, ^{12}C, ^{13}C, ^{14}C	^{12}N,^{13}N, ^{14}N, ^{15}N,^{16}N	^{14}O, ^{15}O, ^{16}O, ^{17}O, ^{18}O
10°	^{10}C, ^{11}C, , ^{13}C, ^{14}C	^{12}N,^{13}N, ^{14}N, ^{15}N,^{16}N	^{14}O, ^{15}O, ^{16}O, ^{17}O, ^{18}O
12°	^{10}C, ^{11}C, ^{12}C, – , –.	^{12}N,^{13}N, ^{14}N, ^{15}N,^{16}N	^{14}O, ^{15}O, ^{16}O, ^{17}O, ^{18}O.
15°	^{10}C, ^{11}C, – , – , ^{14}C.	^{12}N,^{13}N, ^{14}N, ^{15}N,^{16}N	^{14}O, ^{15}O, ^{16}O, ^{17}O, ^{18}O
17°	–	^{12}N,^{13}N, ^{14}N, ^{15}N,^{16}N	^{14}O, ^{15}O, ^{16}O, ^{17}O, ^{18}O
20°	^{10}C, ^{11}C, ^{12}C, – , ^{14}C	^{12}N,^{13}N, ^{14}N, ^{15}N,^{16}N	^{14}O, ^{15}O, ^{16}O, ^{17}O, –.
25°	^{10}C, ^{11}C,^{12}C, ^{13}C, ^{14}C	^{12}N,^{13}N, ^{14}N, ^{15}N,^{16}N	–
30°	^{10}C, ^{11}C,^{12}C, ^{13}C, ^{14}C	^{12}N,^{13}N, ^{14}N, ^{15}N,^{16}N	–
35°	^{10}C, ^{11}C, ^{12}C, ^{13}C, –.	–	–
40°	^{10}C, ^{11}C, ^{12}C, ^{13}C, –.	–	–
45°	^{10}C, ^{11}C, ^{12}C, ^{13}C, –.	–	–

3.8 Tail correction

These corrections only applied to the BCD spectra. Particles with sufficient energy could either punch through the 16 mm active volume of the BCD depositing only a partial amount of their energy in the detector, or stop in the sampling region between the Frisch grid and the anode. These particles created a fold back in the BCD PID spectrum (see Figure 3.10) also seen in other experiments using such BCDs [Bar04]. Most fragments detected by the BCD especially at the forward angles caused this fold back effect, which affected the smoothness between the atomic number and the energy of a Bragg signal thereby contaminating the various

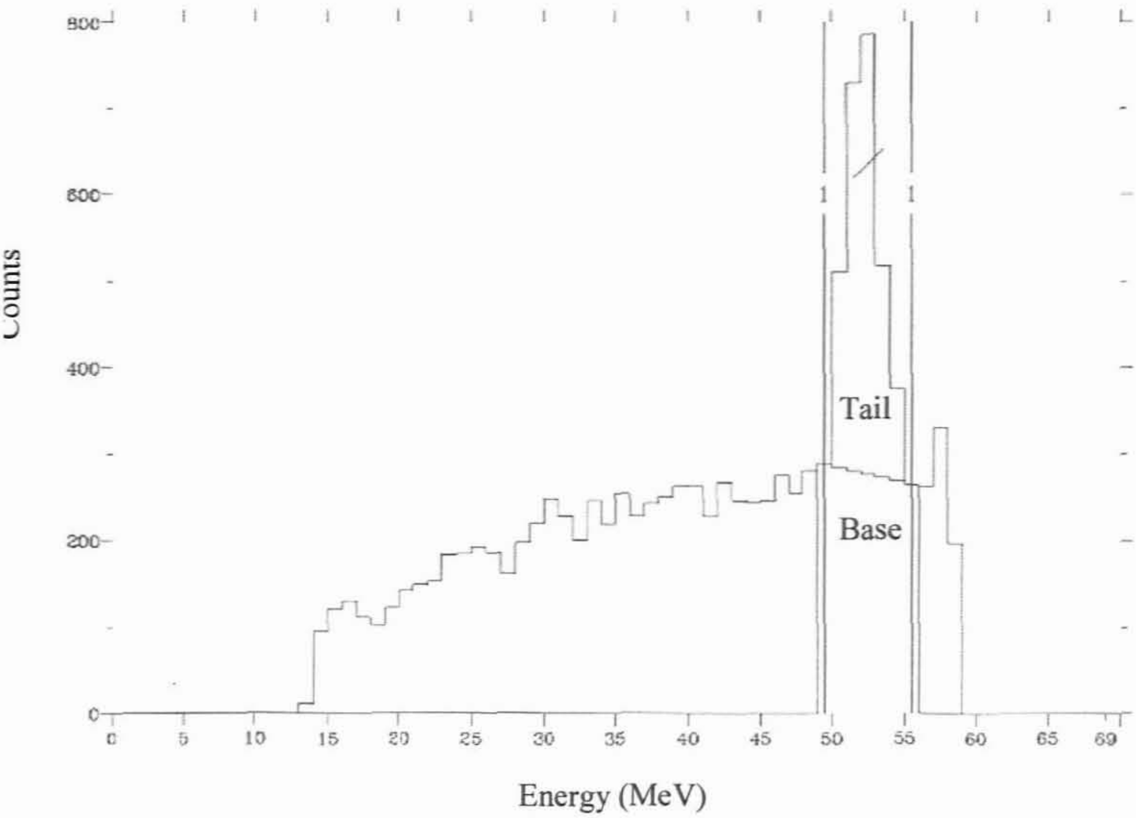

Figure 3.11: *The BCD energy spectrum showing the tail to be corrected.*

loci. These effects affected mostly the high energy part of the loci. In these cases, it was necessary to correct the contributions from such tails to the inclusive spectra.

The corrections of the tail events were performed in XSYS. The procedure for the tail correction was as follows. The region of the tail was isolated by setting a gate around the peak in the energy spectrum as depicted in Figure 3.11. A linear background was then fitted underneath the peak and subsequently subtracted from the gated region. The resulting tail portion was then subtracted from the original spectrum.

In the case of severe contamination these loci in the PID spectrum were truncated. This procedure created a gap in the double differential cross sections which contained both the BCD as well as the Si telescope data as shown in chapter 5. This gap in the double differential cross sections is approximately 35 MeV.

3.9 Conversion to double differential cross sections

The number of counts in the analyzed spectra was converted to the double differential cross sections. The conversion of the spectra was carried out by multiplying the number of counts with a conversion factor. Double differential cross sections (in mb. $sr^{-1}.MeV^{-1}$) were obtained by using the equation [För92]

$$\frac{d^2\sigma}{d\Omega\, dE} = N_c \cdot \Lambda \tag{3.2}$$

where,

$N_c \cong$ is the corrected number of counts in an energy bin where the conversion factor Λ was calculated from:

$$\Lambda = \frac{1}{\Delta E \Delta\Omega} \frac{e \cos\theta_T A}{N \lambda_T N_A D} \tag{3.3}$$

where

$\Delta\Omega \cong$ is the solid angle in (sr) given by equation 2.2,

$\Delta E \cong$ is the energy per bin (in MeV),

$e \cong$ is the proton charge,

D $\cong$ is the correction factor for the electronic dead time,

$\rho \cong$ is the density of target nuclei (in barn),

N $\cong$ is the total number of carbon nuclei incident on the target which was determined from:

$$N = \frac{N_0}{6} \tag{3.4}$$

where,

$N_0 \cong$ is the number of protons in the ^{12}C nucleus calculated from

$$N_0 = \frac{C}{e} \tag{3.5}$$

where

$e \cong$ is the proton charge,

C $\cong$ is the total integrated charge as measured by the current integrator at the beam stop (in Coulomb) which is given by:

$$C = CI \cdot R \cdot 10^{-12}, \tag{3.6}$$

where,

CI $\cong$ is the inhibited scaler read-out of the Current integrator,

R $\cong$ is the selected range (in nA) which represents 1000 counts·s^{-1} for full scale readout and ρ is given by the expression:

$$\rho = \frac{\lambda_T N_A}{\cos \theta_T A}, \tag{3.7}$$

where

$\lambda_T \cong$ is the target thickness expressed in mass per unit area,

$N_A \cong$ is Avogadro's number,

$\theta_T \cong$ is the angle of the target's normal with respect to the beam direction, and

A $\cong$ is the atomic mass of the target.

3.10 Error analysis

3.10.1 Statistical errors

The statistical error is based on the uncertainty in the total number of counts. One standard deviation on the counts is equal to the square root of the total number of counts, so that the range of values $N_i \pm \sqrt{N_i}$ will contain the true number of counts. The propagation of the statistical error for the background subtractions and tail corrections were performed in XSYS for each spectrum analyzed. Statistical errors are presented as error bars together with the double differential cross sections.

3.10.2 Systematic errors

The uncertainties which are assumed to contribute to the systematic errors are solid angle, particle identification, total charge, target thickness, electronic dead time and energy calibrations.

a) Solid angle

The uncertainty in the solid angle was due to the uncertainties in the distances from the centre of the target to the back of the respective collimators as well as in the radii of these collimators. The uncertainty in the solid angles of the Si detector telescope and BCD was found to be less 0.1-1%.

b) Target Thickness

The uncertainty in the uniformity of the target thickness is an important contributor to the systematic error. Such possible variations in the target thickness were checked after the experiment with a ^{228}Th source. The runs with the ^{12}C target positioned at the center, at two thirds and at one third positions above and below the target center were performed as shown in table 3.2 where position 445 corresponds to the center of the target. The 8.78 MeV alpha energy peak appeared to be consistent for the different positions. The 8.78 MeV alpha energy peak appeared in channels 322.1 channel numbers using an empty target. The uncertainty in the target thickness was found to be less than 1%.

Table 3.2: *The target thickness variations showing the appearance of the 8.78 MeV alpha peak for different target positions.*

Target position	Target	8.78 MeV peak (Channel no.)
445	empty	319.8
450	^{12}C	319.7
440	^{12}C	320.0
435	^{12}C	320.0
455	^{12}C	320.1

c) Energy calibrations

The uncertainty in the energy calibration of the Si telescope was based on the calculated energy value of the ground state peak using KINMAT. Most of the energy spectra were out by less than 2 MeV to the expected energy value. Uncertainty in the energy calibration of the Si detector telescope was therefore estimated to be 1%. In the case of the BCD, the uncertainty arose from the energy loss of the alpha particles in the entrance window. The energy loss was taken into account by identifying the 8.78 MeV alpha peak in the spectrum. The uncertainty was estimated to be less than 1%.

d) Particle identification

The uncertainty in the particle identification of the Si telescope resulted from the gates that were set on the mass function spectra to separate the different isotopes of C, N, and O. There were possibilities that some isotopes may fall outside the gate and contribute to the yield in a neighboring gate. The uncertainty in the Si telescope was estimated to be 1%.

In the case of the BCD, the main contributor to the uncertainty in the PID was due to fold backs as discussed in subsection 3.9. The uncertainty was estimated to be less than 5%.

e) Total charge

The uncertainty in the total charge was estimated to be less than 0.5%

f) Electronic dead time

The uncertainty in the electronic dead time was estimated to be less than 2%.

A combination of all the sources listed in table 3.3, give the linear summed error of 5.6 % for Si detector telescope and a value of 9.6% for the BCD. The total systematic errors for Si detector telescope are 2.7% and 5.6% for the BCD.

Table 3.3: *Summary of the total systematic errors*

	Si telescope	BCD
Source	Error in %	Error in %
Solid angle	0.1%	0.1%
Target thickness	1%	1%
Energy calibrations	1%	1%
Electronic dead time	2%	2%
Total charge	0.5%	0.5%
Particle identification	1%	5%
Linear sum	5.6%	9.6%
Total systematic errors	2.7%	5.6%

CHAPTER 4

Theoretical Model

4.1 Introduction

Most of the nuclear reaction mechanisms studies conducted at iThemba LABS have been interpreted with the theoretical model that was initiated and developed at the University of Milano during the past fifteen years. In the previous studies of IMF production in C and O induced reaction on ^{93}Nb and ^{59}Co at incident energies between 6 to 25 MeV/n [Gad03], this model was implemented successfully to describe the contributions of different reaction mechanisms such as nucleon coalescence and projectile break-up and showed the reproduction of the energy and angular dependence of the observed IMF spectra.

In this model, it is assumed that the projectile loses energy before breaking up, the energy loss occurs when two ions come into contact. After breaking up both fragments may be emitted without further interaction with the target nucleus or the participant may violently interact or even fuse with the target nucleus. In the present study the model is revisited to study the reaction mechanisms involved in the emission of IMF in the much lighter system of ^{12}C with ^{12}C at an incident energy of 200 MeV.

This chapter presents the theory of fragmentation or break-up of the projectile based on the original Serber approximation [Ser47] as well as nucleon coalescence which describes the intranuclear interaction cascade through which the initial kinetic energy of the two fusing ions transforms into random thermal energy by a set of Boltzmann Master equations (BME) [Cav98].

4.2 Nucleon coalescence

The method in studying the emission of nucleons ([Fab89], [Fab91]), light particles [Cer92] and intermediate mass fragments [Cav92] during the pre-equilibrium phase of a nuclear reaction between heavy ions started from the evolution of many body systems through two-body scattering. The subsequent time evolution of the system has been followed by solving a set of Boltzmann master equations (BME) [Cav96], as first proposed by Harp *et al* [Har68]. BME simulates the cascade of nucleon-nucleon interactions by defining a set of bins which have a constant volume in momentum space.

To evaluate inclusive particle spectra one may exploit the azimuthal symmetry with respect to the beam direction and use only two independent variables p^2, the square of the nucleon's momentum, and p_z, its component along the beam axis. The bins may thus be characterized by constant values of Δp^2 and Δp_z. The bin indices label momentum space intervals with volume $V_p = \Delta\epsilon\Delta p_z$ centered around given values of the energy ϵ_i, and $(p_z)_i$. With an appropriate ordering of the bins one may still label each bin by only one index. Describing the nucleus as a two-fermion gas, the set of BME for the proton gas is given by [Cav96]

$$
\begin{aligned}
\frac{d(n_i g_i)^\pi}{dt} = & \sum_{jlm} [\omega^{\pi\pi}_{jlm\to ij} g^\pi_l n^\pi_l g^\pi_m n^\pi_m (1-n^\pi_i)(1-n^\pi_j) \\
& - \omega^{\pi\pi}_{ij\to lm} g^\pi_i n^\pi_i g^\pi_j n^\pi_j (1-n^\pi_l)(1-n^\pi_m)] \\
& + \sum_{jlm} [\omega^{\pi\nu}_{lm\to ij} g^\pi_l n^\pi_l g^\nu_m n^\nu_m (1-n^\pi_i)(1-n^\nu_j) \\
& - \omega^{\pi\nu}_{ij\to lm} g^\pi_i n^\pi_i g^\nu_j n^\nu_j (1-n^\pi_l)(1-n^\nu_m)] \\
& - n^\pi_i g^\pi_i \omega^\pi_{i\to i'} g^\pi_{i'} \delta(\in^\pi_i - \in^\pi_F - B^\pi_i - \in^\pi_{i'}) - \frac{dD^\pi_i}{dt}
\end{aligned}
\tag{4.6}
$$

where π and ν indicate the protons and the neutrons respectively. The quantities g_i are the total number of states in bin i. The quantities $\omega_{ij\to lm}$, $\omega_{i\to i'}$ and dD_i/dt are respectively, the internal transition decay rates, the decay rates for emission of single protons into the continuum, and a depletion term which accounts for the emission of protons bound in clusters. The internal transition rates $\omega_{ij\to lm}$ are still given by [Cav96]

$$\omega_{ij\to lm} = \frac{1}{2\pi}\int_0^{2\pi}\omega_{ij\to lm}\,d\phi_j\,, \tag{4.7}$$

where,

$$\omega_{ij\to lm} = \frac{\sigma_{ij}v_{ij}\prod_{ij\to lm}}{V}, \tag{4.8}$$

$V \cong$ is the nuclear volume

$v_{ij} \cong$ is the two interacting nucleon relative velocity.

The indexes i, j, l, m stands for momenta p_i, p_j, p_l, p_m and ϕ_j is the azimuthal angle of p_j, having taken $\phi_i = 0$. The quantity $\Pi_{ij\to lm}$ represents the probability of reaching bins l and m if the interacting nucleons have momenta p_i and p_j belonging to bins i and j. The decay rates $\omega_{i\to i'}$ are given by [Cav96]

$$\omega_{i\to i'} = \frac{\sigma_{inv}v'_i}{g_i V'}, \tag{4.9}$$

where,

$\sigma_{inv} \cong$ is the inverse process cross section

$v'_i \cong$ is the relative velocity between the nucleon and the residual nucleus.

$V' \cong$ is the laboratory volume which cancels a similar factor appearing in the expression of $g_{i'}$ in equation 4.6.

The differential multiplicity of the particles emitted in the time interval dt at an angle θ with energy E′ is given by [Cav96]

$$\frac{d^3\mathrm{N}'(E',\theta,t)}{dE'd\theta dt} = R\mathrm{N}(\epsilon,\theta,t)\frac{\sigma_{inv}v'}{V'}\rho(E',\vartheta), \tag{4.10}$$

where,

$E' \cong$ is the energy of the emitted particle in the continuum,

$N(\epsilon,\theta,t) \cong$ is the occupation probability of the states of the considered particle inside the composite nucleus.

$R \cong$ is the survival factor that takes into account the possible dissolution of the cluster before emission.

$$\rho(E',\theta) = \frac{\sin\theta}{2}\rho(E'), \tag{4.11}$$

where,

$\rho(E') \cong$ is the density of the particle states in the continuum.

The measured multiplicity spectra are given by [Cav96]

$$\frac{d^2M}{dE'd\Omega} = \int_0^{t^*} \frac{1}{2\pi\sin\theta}\frac{d^3N'(E',\theta,t)}{dE'd\theta dt}dt, \tag{4.12}$$

In a first approximation the refraction of the projectile and the ejectile as they cross the nuclear surface is not considered.

$t^* \cong$ is the time at which the emission of high energy is over.

For nucleons, $N(\epsilon,\theta,t)$ interpolates the values of the bin occupation numbers n_i in (4.6) and R is equal to unity.

For clusters with energy E_c inside the nucleus, the direction defined by the angle θ_c with respect to the beam, $N(\epsilon,\theta,t) \cong N(E_c,\theta_c,t)$ is given by [Cav96], [Gad02]

$$N(E_c,\theta_c,t) = \prod_i (n_i^{\pi})^{P_i(E_c,\theta_c)Z_c} \cdot \prod_i (n_i^{\nu})^{P_i(E_c,\theta_c)N_c}, \tag{4.13}$$

where the index i runs over all the bins in which the nucleons constituting the cluster may be found and $P_i(E_c,\theta_c)$ is the fraction of bin i within the Fermi sphere of the cluster C with radius p_{cF}. Z_c and N_c are numbers of protons and neutrons of cluster c, respectively.

If Q_c is the Q-value for cluster emission and $A_c = N_c + Z_c$, then E'_c, the continuum energy of the cluster c, is given by [Cav96], [Gad02]

$$E_c' = E_c + Q_c - A_c(\epsilon_F - \epsilon_{Fc}), \tag{4.14}$$

where ϵ_F and ϵ_{Fc} are the composite nucleus and the cluster Fermi energies, respectively.

The depletion term dD_i^{π}/dt in (4.6) is given by [Cav96],

$$\frac{dD_i^{\pi}}{dt} = \sum_c \iint P_i(E_c, \theta_c) Z_c \frac{d^3 N'(E_c', \theta_c, t)}{dE_c' d\theta_c dt} dE_c d\theta_c, \tag{4.15}$$

where the summation runs over all possible clusters and the integrals are over all the angles and energies of clusters containing a proton or a neutron in bin i.

4.3 Monte Carlo implementation in the transport code Fluka

4.3.1 Introduction

The nucleus-nucleus reaction Fluka code [Fas03], [Fas05], which is based on the BME theory [Cav96] explained in section 4.3 was used to calculate the double differential cross sections presented in this thesis.

The BME theory describes the thermalization of an excited nucleus by evaluating the variation with time of the distribution of the momenta of its nucleons as a result of their mutual interactions and their emission into the continuum either as separate entities or as a part of a cluster (a light particle or an IMF). The nucleon momentum space is divided into bins of volume $\Delta V = 2\pi \cdot m \cdot \Delta\varepsilon \cdot \Delta p_z$ (where m and ε are the nucleon mass and energy and p_z is the component of the nucleon momentum along the beam axis) and the time evolution of the occupation probability $n(\varepsilon,\theta,t)$ of the states in each bin is calculated. To this aim a set of coupled differential equations, expressing the variation of $n(\varepsilon,\theta,t)$ in the time interval between t and $t+dt$ as a function of the occupation probabilities at time t and the decay rates (4.9) for nucleon-nucleon scatterings and emissions into the continuum, has to be integrated. The information so obtained is inclusive, i.e., averaged over many different reaction paths. In other words, the theory provides the mean multiplicities of emitted particles and

does not allow one to analyze exclusive processes or evaluate other measurable quantities like, for instance, the cross section for the formation of a particular residue.
In order to eliminate such limitations we assume that the probability of emitting a particle i with energy between ε and $\varepsilon + d\varepsilon$ at a polar angle between θ and $\theta+d\theta$ in the time interval $(t,t+dt)$ be equal to its expected differential multiplicity $d^3N_i(\varepsilon,\theta,t)$ evaluated with the BMEs. The probability of any possible sequence of events may be evaluated as a joint probability using these elementary probabilities.
This approach, anyway, is not easily integrated in a transport code such as FLUKA because the run-time calculation of the triple differential multiplicity spectra which may be needed for all the particles emitted through the pre-equilibrium phase, is too time consuming for allowing the simulation of the reactions induced in thick materials of complex geometry. Even the run-time access to pre-computed spectra is out of reach if we have to consider every possible projectile-target-incident energy combination.

4.3.2 Complete fusion calculations

To provide the FLUKA code with a more realistic treatment of nucleus-nucleus interactions below 100 MeV/nucleon, it has been adopted the strategy of using the BME theory to describe the complete fusion of a representative set of ion pairs at different energies, fitting the predicted ejectile multiplicities and double differential spectra with simple analytical expressions containing a small number of parameters. These parameters are stored in a database which may be read by the FLUKA code. This way the simulation of the thermalization can be performed in the short times needed to make the transport code calculations [Cer06] feasible. The further de-excitation of the excited equilibrated nuclei which are produced is handled by the FLUKA evaporation/fission/fragmentation module.

For any pair of interacting ions the reaction cross section (σ_R) is calculated with an improved version [Cer05] of a model proposed by P.J. Karol [Kar75] and is subdivided into two different mechanisms: the complete fusion with probability $P_{CF} = \sigma_{CF} / \sigma_R$ and a peripheral collision with probability $P=1-P_{CF}$.

For any peripheral collision, an impact parameter b is chosen by extraction of random numbers and a standard acceptance-rejection technique using the differential cross-section $d\sigma_R/db$. As discussed in [Kar75], the model predicts the formation of rather cold projectile-like and target-like nuclei, and a middle system preferentially excited, the mass number of which is obtained by integrating the projectile's and the target's Fermi densities over the overlapping region.

To extract a possible value for the emission angle of a given particle, the predicted cumulative angular distribution [Mai06],

$$\int_0^\theta \frac{dM}{d\theta} d\theta$$

(in the center of mass frame) at the considered incident energy was used. To obtain the energy of the emitted particles we used analytical functions which accurately reproduce their theoretical double differential spectra (in the center of mass frame), as [Mai06]:

$$d^2M/(dEd\Omega) = E^{P_0(\theta)} \exp(-P_1(\theta) - P_2(\theta)E)$$

E is the particle emission energy and $P_0(\theta)$, $P_1(\theta)$, and $P_2(\theta)$ are parameters depending on the emission angle, particle type, incident energy, and interacting ions. These parameters are obtained at a few incident energies between 10 and 100 MeV by interpolating the values obtained for a few incident energies and emission angles to other experimental data [Mai06].

The comparisons between the calculated and the measured double differential cross sections are presented in chapter 5.

CHAPTER 5

Results and discussion

5.1 Overview

This chapter presents the experimental and some theoretical results of carbon (C), nitrogen (N) and oxygen (O) fragments emitted in the interaction of ^{12}C with ^{12}C at an incident energy of 200 MeV. While the calculations of the other spectra are still in progress, in this thesis some oxygen isotope spectra are compared with the theoretical results at different angles to confirm the different reaction mechanisms involved in their emission.

5.2 C, N and O measured energy spectra

Figures 5.1-5.4 show the laboratory double differential cross sections of the C, N and O fragments. These spectra are shown in the angular range of 15° to 45°. The low energy part of the spectra was measured with the BCD while the high energy part of the spectra was measured with the Si detector telescope. The low-energy cut-off of about 15 MeV in the BCD data arises from the minimum energy threshold of the detector. While the minimum energy threshold of the Si detector telescope is not more than 60 MeV depending on the fragment detected. The gap between the BCD data and Si detector telescope data arises from the gates set around the loci in the BCD PID spectra to avoid the contributions of the tailing effects to the spectra which could not be corrected for as discussed in section 3.8. As was mentioned before, isotope separation was not achieved with the BCD.

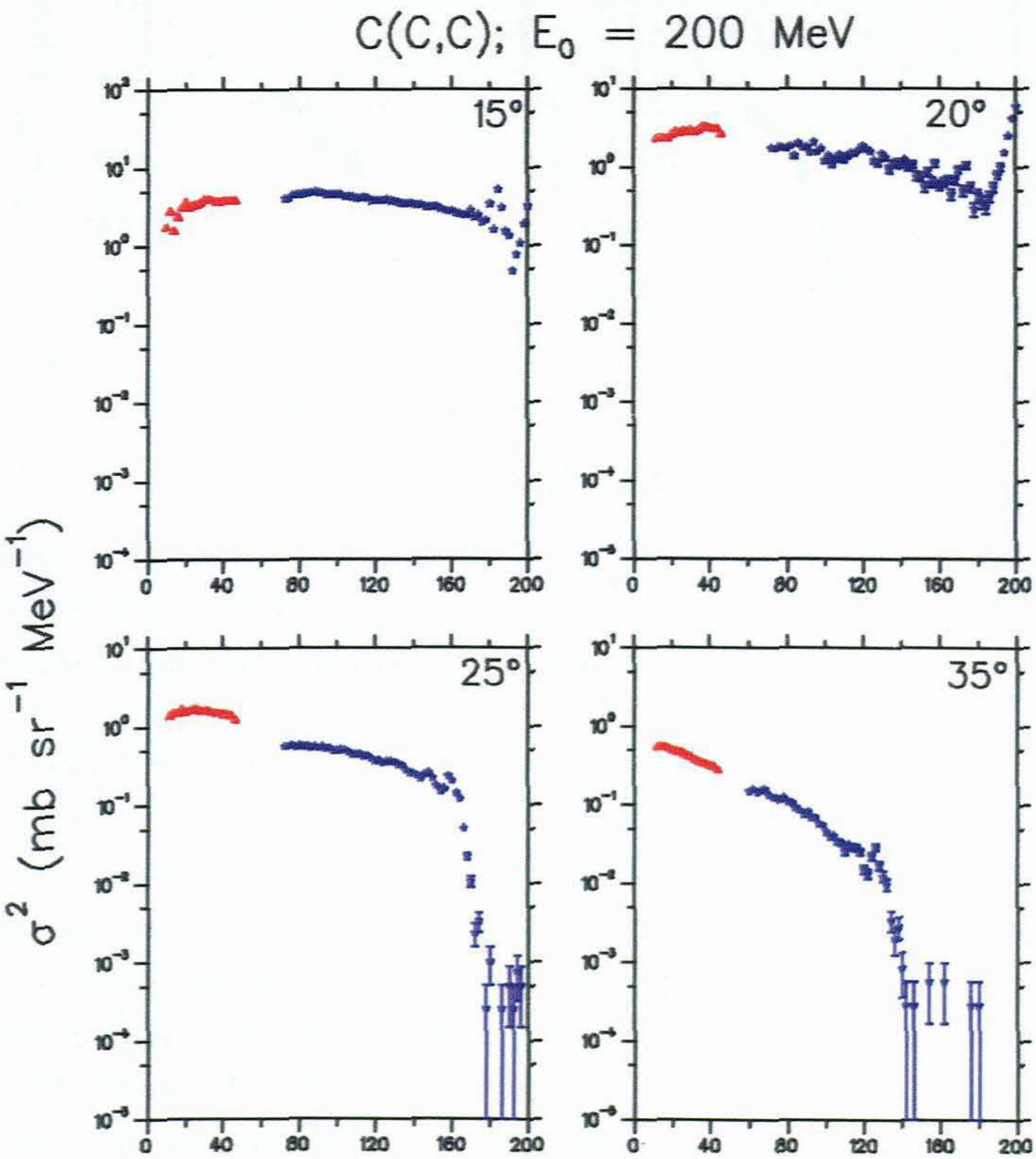

Figure 5.1: *Laboratory Double differential cross sections of carbon fragments at different emission angles. Triangles represent BCD data, Si detector telescope data are presented as the star data points. The error bars reflect the statistical errors.*

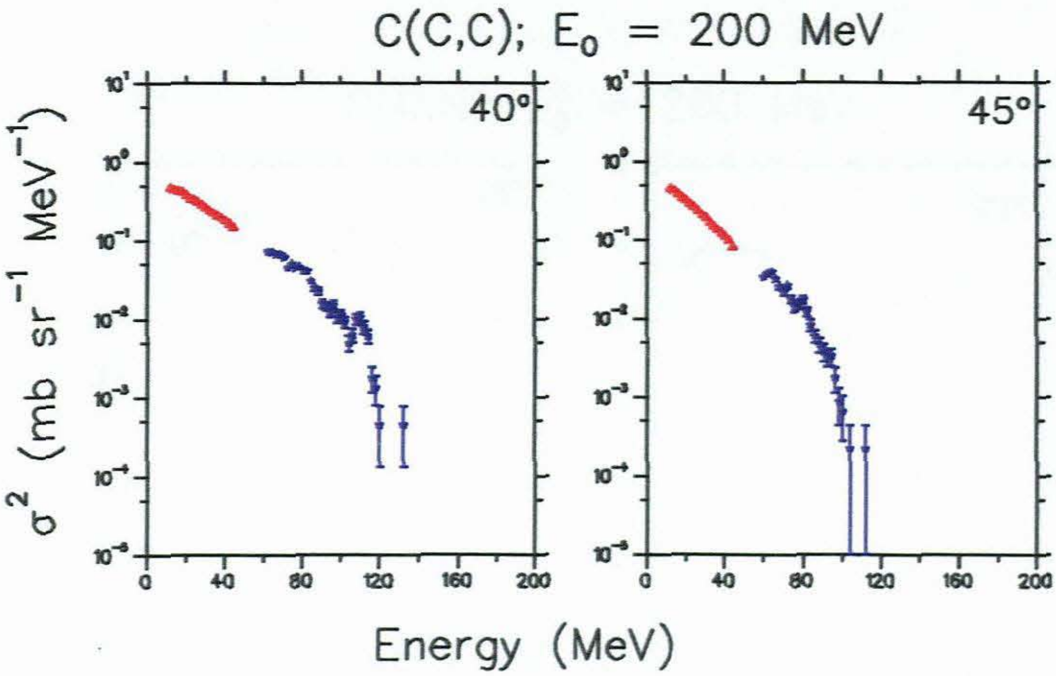

Figure 5.2: *Laboratory double differential cross sections of carbon fragments at emission angles of 40° and 45°. Triangles represent the BCD data, stars represent Si detector telescope data points. The error bars reflect the statistical errors.*

It is difficult to analyze the reaction mechanism involved in the production of C, N, and O fragments as measured with the BCD, since the yield consists of the different isotopes which were produced in different reaction mechanisms. The carbon fragments are produced with high yield at forward angles which decreases as the emission angle increases, the slope of the energy spectra becomes steeper. At the lower energies of the spectra at the most forward emission angles the continuum spreads over more than 140 MeV (see figure 5.1). At larger emission angles carbon is emitted with energy of less than 140 MeV (see figure 5.2).The nitrogen fragments were detected up to 40° (see figure 5.3). The energy spectra are mainly dominated by the continuum region. In this region the pre-equilibrium reaction mechanisms mainly dominate the production of these fragments. Similarly, oxygen fragments are also mainly produced by pre-equilibrium reaction mechanisms. These fragments are produced with a lower yield compared to N and C (see figure 5.4). The nitrogen and oxygen spectra follow the same trend as for the carbon fragments. With increasing detection angle, the cross sections of these fragments decrease and the slopes of the energy spectra become steeper displaying an exponential decay character.

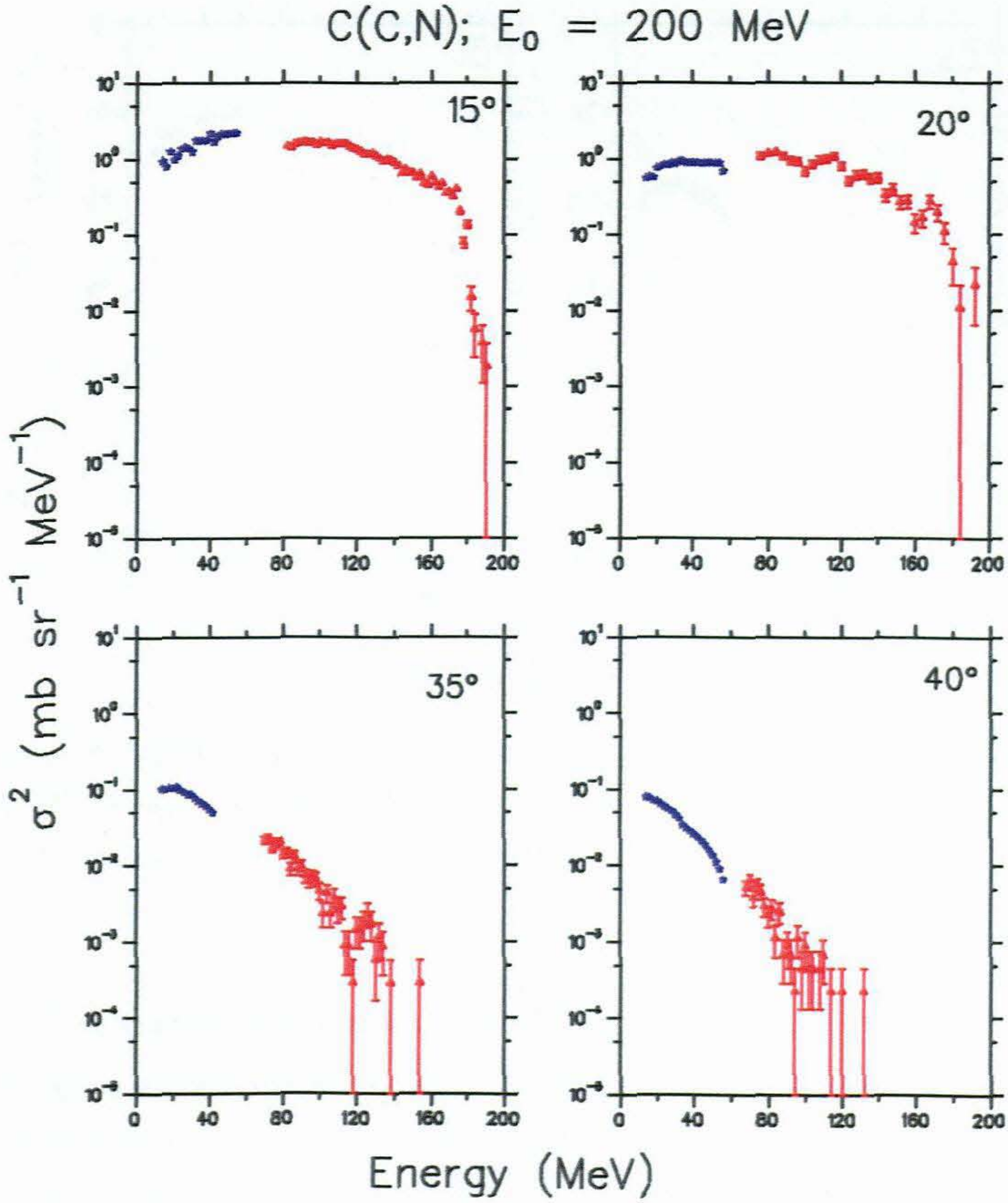

Figure 5.3: *Laboratory double differential cross sections of nitrogen fragments at different emission angles. Stars represent BCD data while triangles represent Si detector telescope data points. The error bars reflect the statistical errors.*

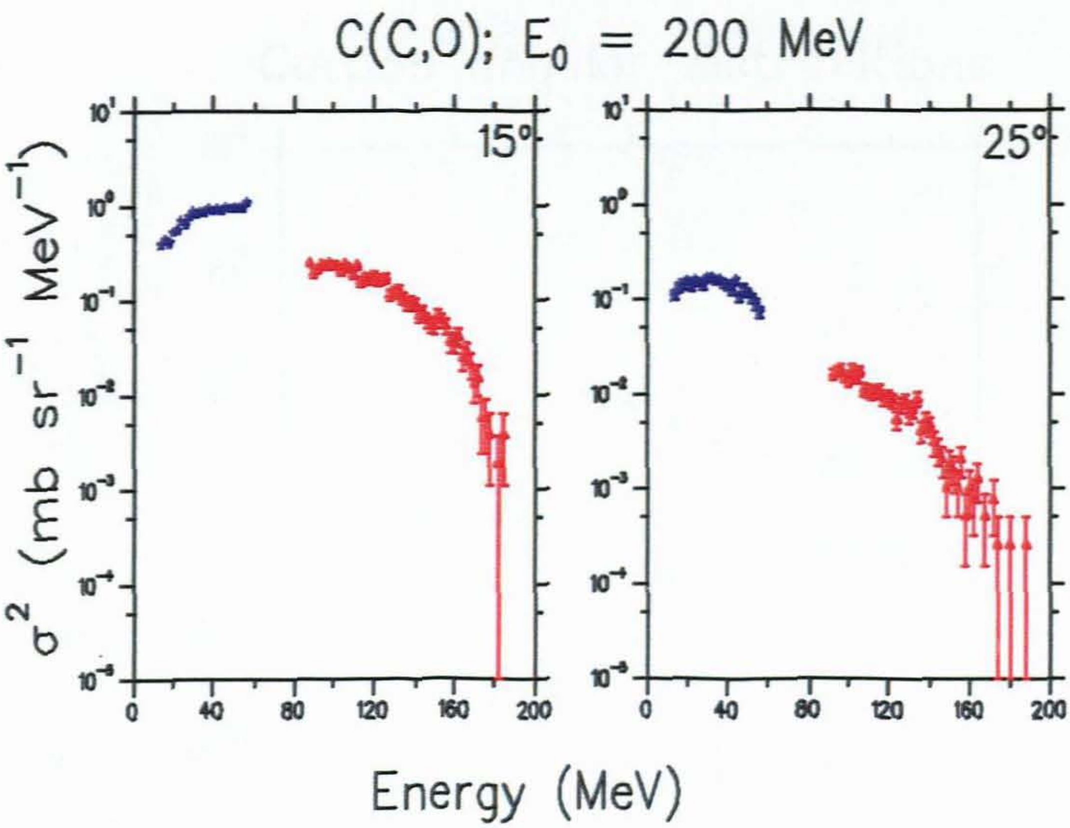

Figure 5.4: *Laboratory double differential cross sections of oxygen fragments at 15° and 25°. Triangle represent BCD data and star represent Si detector telescope data points. The error bars reflect the statistical errors.*

5.3 The angular distributions of C, N and O fragments.

The angular distributions of C, N and O emitted in the interaction of ^{12}C with ^{12}C at an incident energy of 200 MeV are shown in figures 5.5, 5.6 and 5.7, respectively. These double differential cross sections were extracted from energy spectra measured with the BCD at emission energies of 20 and 40 MeV, respectively, while the data at the larger energy cuts were measured with the Si detector telescope. The angular distributions were extracted from the differential energy cross sections at selected emission energies. The angular distributions for C, N and O exhibit a significant linearity toward large angles. A similar behavior was observed in the emission of light particles in heavy ion reactions [Awe80]. It is significant that for the lowest emission energy i.e. 20 MeV the angular distribution is almost isotropic with respect to the

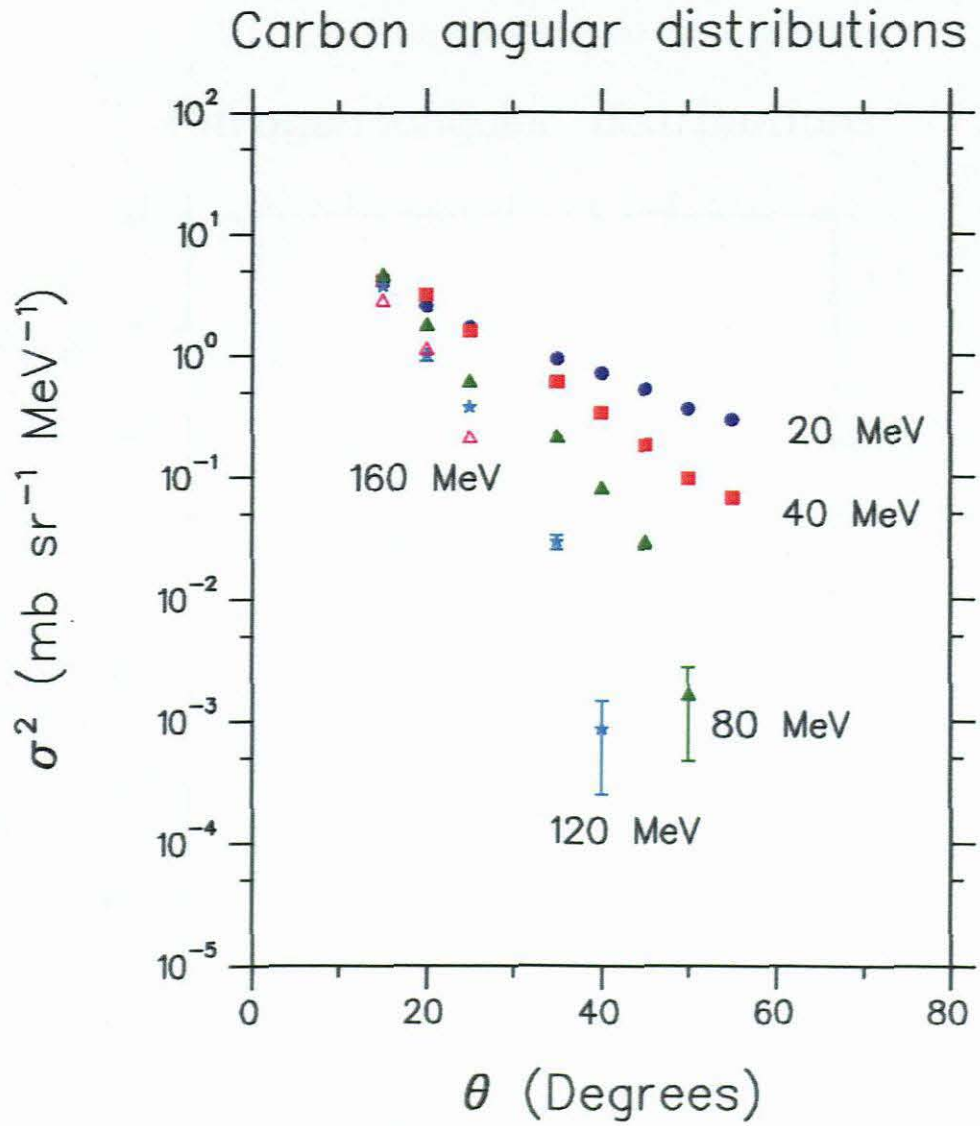

Figure 5.5: *Angular distributions of carbon fragments measured with the BCD and Si detector telescope in the interaction of ^{12}C with ^{12}C at an incident energy of 200 MeV. The energies are shown in the figure. The error bars reflect the statistical errors.*

emission angle especially for carbon fragments. The slopes of the angular distributions of C, N, and O fragments decrease rapidly as the emission angle increases. The double differential cross section decreases with the increasing emission angle. As the increasing mass of the detected fragments the angular distribution becomes steeper.

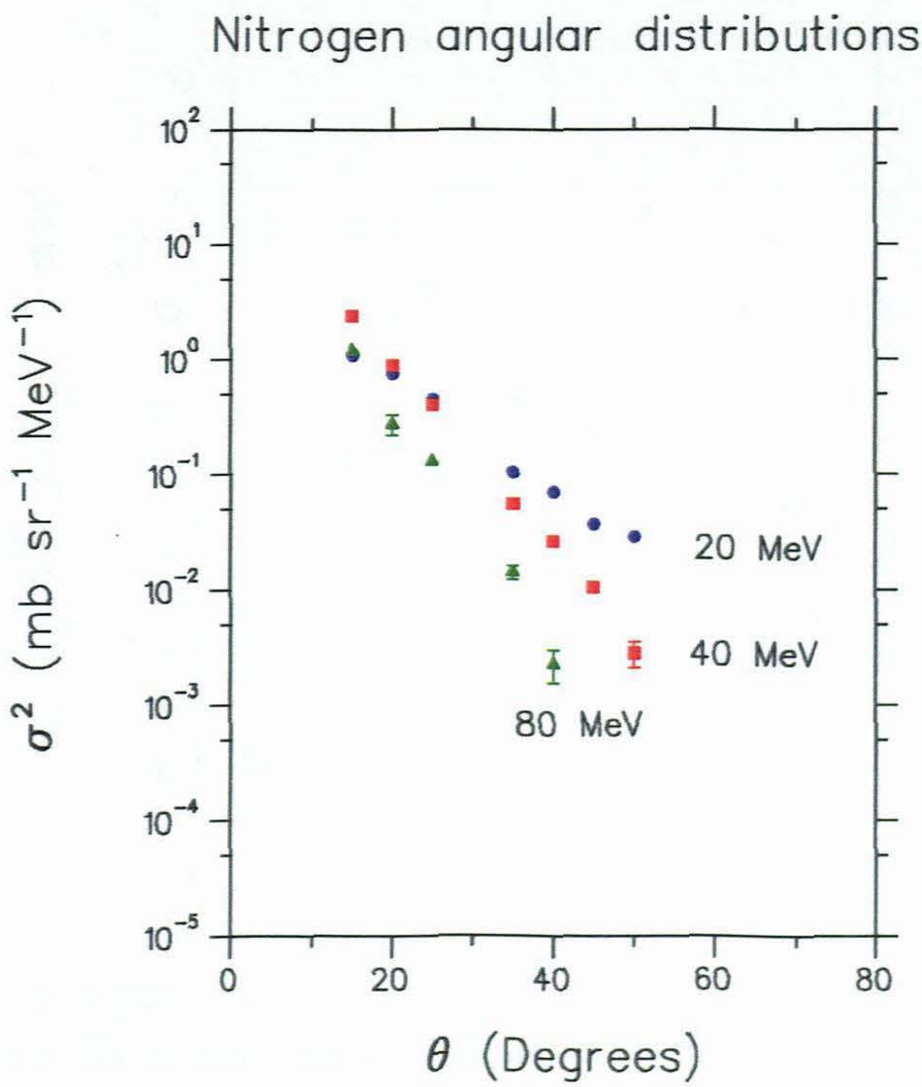

Figure 5.6: *Angular distributions of nitrogen fragments measured with the BCD as well as the Si detector telescope in the interaction of* ^{12}C *with* ^{12}C *at an incident energy of 200 MeV. The energies are reflected in the figure. The error bars reflect the statistical errors.*

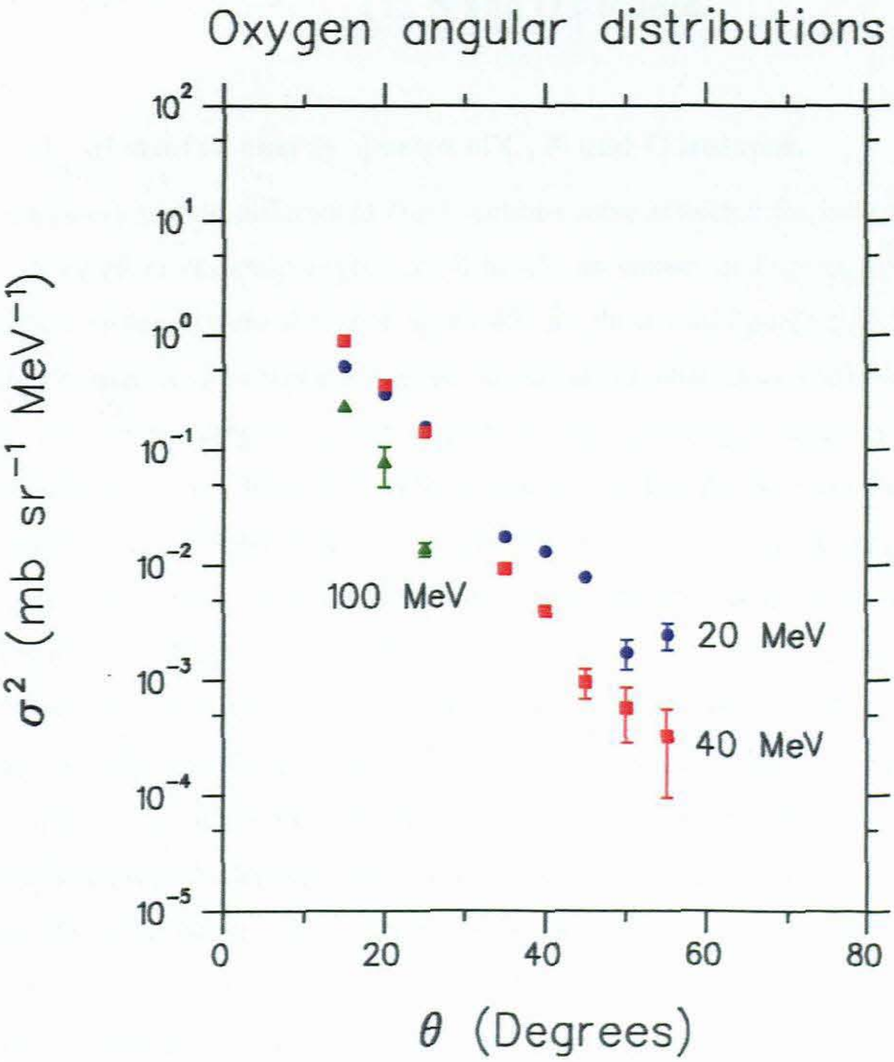

Figure 5.7: *Angular distributions of oxygen fragments measured with the BCD as well as the Si detector telescope in the interaction of* ^{12}C *with* ^{12}C *at incident energy of 200 MeV. The emission energies are shown in the figure. The error bars reflect the statistical errors.*

5.4 Inclusive spectra of C, N and O isotopes.

5.4.1 Measured energy spectra of C, N and O isotopes.

Laboratory double differential cross sections were extracted for isotopes of C, N, and O detected at emission angles of 8° to 45° as shown in Figures 5.9 to 5.14. The carbon isotopes were detected up to 45° as shown in figures 5.9, 5.10, and 5.11. Mainly two features characterize the double differential cross sections energy spectra of the carbon isotopes. These spectra are dominated by a broad continuum which extends over more than 100 MeV at forward angles. At the most forward emission angles (8° to 20°) the high-energy part of the spectra shows the features of discrete states. These features originate mainly from transfer reactions of few neutrons or protons from the projectile to the target nucleus or vice versa. As the angle increases (25° to 45°) these features of discrete states decrease very rapidly as can be seen in figures 5.10 and 5.11. This behavior was previously also observed by Czudek [Czu91]. The dramatic change in the yield indicates that dominant reaction mechanisms at the forward angles are different or change from the ones describing the spectra at the larger angles. From the previous studies [Gad02] the emission of the particles to the continuum is dominated by pre-equilibrium processes followed by nucleon coalescence in the course of the cascade of nucleon-nucleon interactions by means of which the composite nuclei produced either in the complete or in the partial fusion of the two ions and further by evaporation.

In order to estimate the relative contributions from the continuum region and the discrete states, the double differential cross sections of the C and N-isotopes were first fitted with Legendre polynomials which were then integrated over the outgoing energy as shown in figure 5.8. The energy regions which were used to define the continuum for C and N-isotopes are given in tables 5.1 and 5.2, respectively. Values of the energy integrated cross sections of the continuum as well as the region corresponding to the discrete states are also presented in tables 5.1 and 5.2. These tables clearly indicate the angular dependence of the energy integrated cross sections corresponding to the continuum and the discrete region. This dependence shows that the cross sections of the discrete states decrease much faster than the continuum cross sections as the emission angle increases. At all emission angles ^{12}C has the highest yield followed by $^{11,13}C$ while $^{10,14}C$ are produced with the lowest yields. These isotopes are produced with high cross sections and high emission energies at forward angles, while at larger angles they are produced with lower cross sections and emission energies of less than 125 MeV at 40° and 45°.

The nitrogen isotopes were detected up to 30° as shown in figures 5.12 and 5.13. Only two isotopes ^{14}N and ^{13}N were observed to be produced similarly to the carbon isotopes, while $^{15,12,16}N$ start to show a different trend. In the case of the Nitrogen isotopes, ^{14}N has the highest yield followed by $^{15,13}N$ while $^{12,16}N$ are produced with the lowest yields. The discrete states of the energy spectra of ^{14}N and ^{13}N also decrease rapidly as the emission angle increases. At the emission angles larger than 20°, all nitrogen isotopes were produced with outgoing energies of less than 175 MeV.

All oxygen isotopes were detected up to 20° as shown in figures 5.14 and 5.15. The energy spectra of these isotopes are clearly different to the carbon isotopes at forward angles. At these angles the discrete states were not observed for oxygen isotopes. Since it is unlikely to produce oxygen isotopes through single nucleon transfer reactions. At the largest angle (20°) these isotopes were detected with energies less than 175 MeV. ^{16}O has the highest yield followed by $^{17,15}O$ while $^{14,18}O$ are produced with the lowest yields. At the larger angles evaporation processes dominate the energy spectra since the emission energy of fragments is very low, it is unlikely for compound nucleus to emit particles by pre-equilibrium and nucleon coalescence.

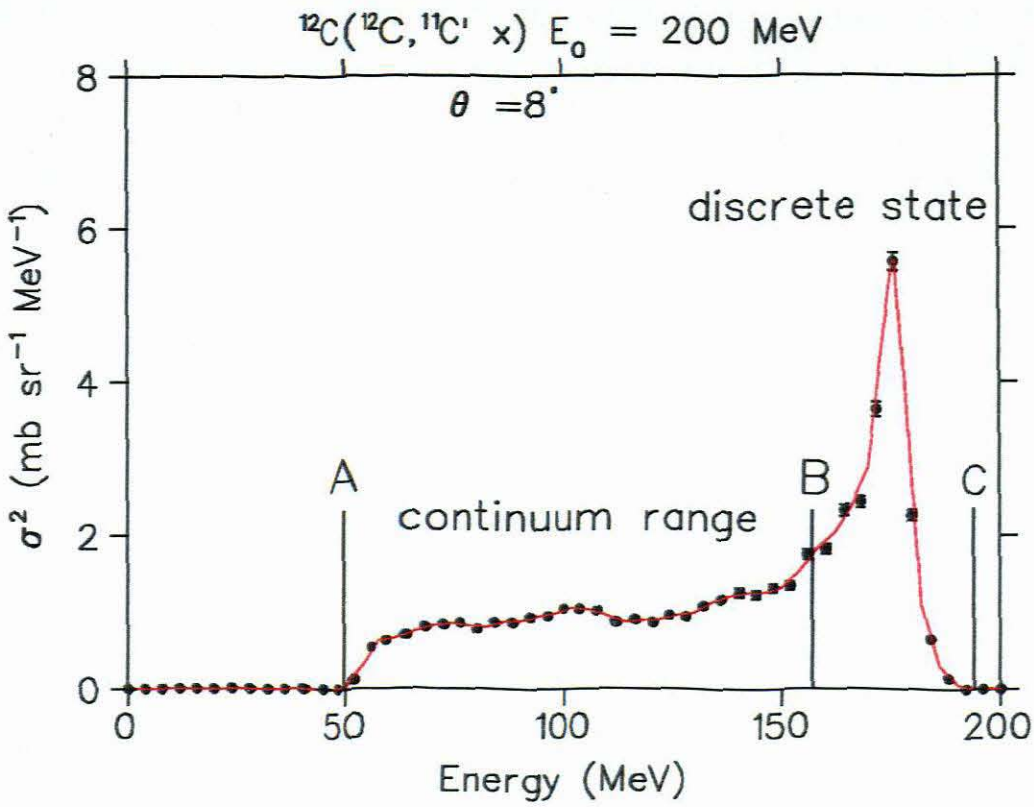

Figure 5.8: *The double differential cross section of ^{11}C at 8° fitted with Legendre polynomials which were then integrated over the outgoing energy. The region from A to B shows the continuum region while B to C shows the discrete state region.*

Table 5.1: *Energy integrated cross sections in (mb/sr) of the continuum (energy range given in last column) as well as the discrete region of the C-isotopes measured at laboratory angles of 8°, 10° and 20° in the bombardment of ^{12}C with 200 MeV ^{12}C ions.*

C-isotope	Continuum [mb/sr]			Discrete region [mb/sr]			Continuum region [MeV]		
	8°	10°	20°	8°	10°	20°	8°	10°	20°
^{12}C	316	-	50	539	-	7	60-168	-	52-160
^{11}C	101	98	45	75	54	8	56-158	64-140	56-152
^{13}C	91	179	-	16	25	-	64-164	60-168	-
^{14}C	10	17	20	2	1.6	5	68-148	62-158	60-154
^{10}C	4	11	6	12	5	1	56-116	54-152	52-150

Table 5.2: *Energy integrated cross sections in (mb/sr) of the continuum (energy range given in last column) as well as the discrete region of the N-isotopes measured at laboratory angle of 8° in the bombardment of ^{12}C with 200 MeV ^{12}C ions.*

N-isotope	Continuum [mb/sr]	Discrete region [mb/sr]	Continuum region [MeV]
	8°	8°	8°
^{14}N	65	17	76-156
^{13}N	8	12	66-144
^{15}N	45	3	72-156
^{12}N	2	0.6	68-132
^{16}N	3	0.3	76-140

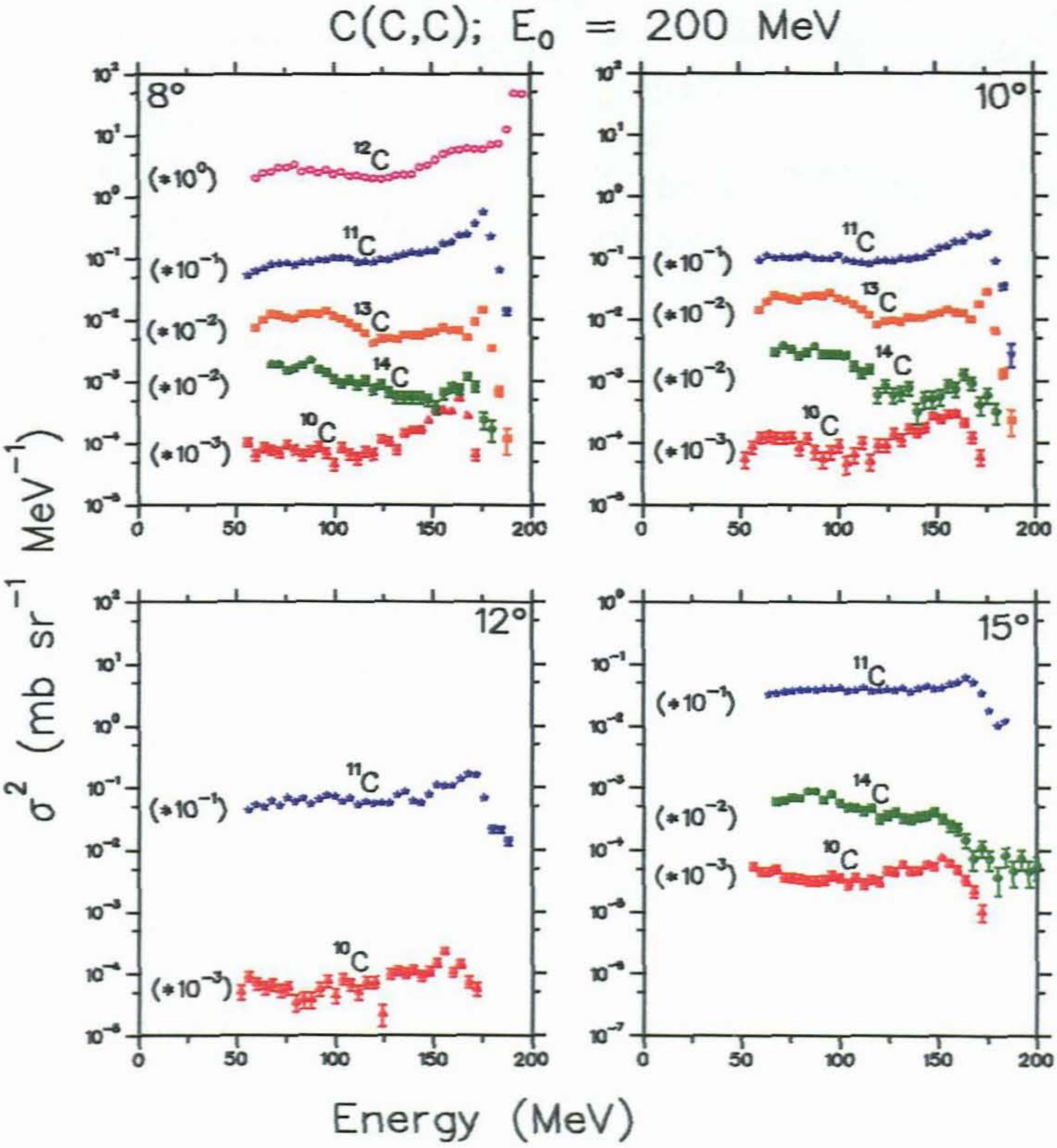

Figure 5.9: *Double differential cross sections of carbon isotopes emitted at different angles shown in the figure in the interaction of* ^{12}C *with* ^{12}C *at an incident energy of 200 MeV. The error bars reflect the statistical errors.*

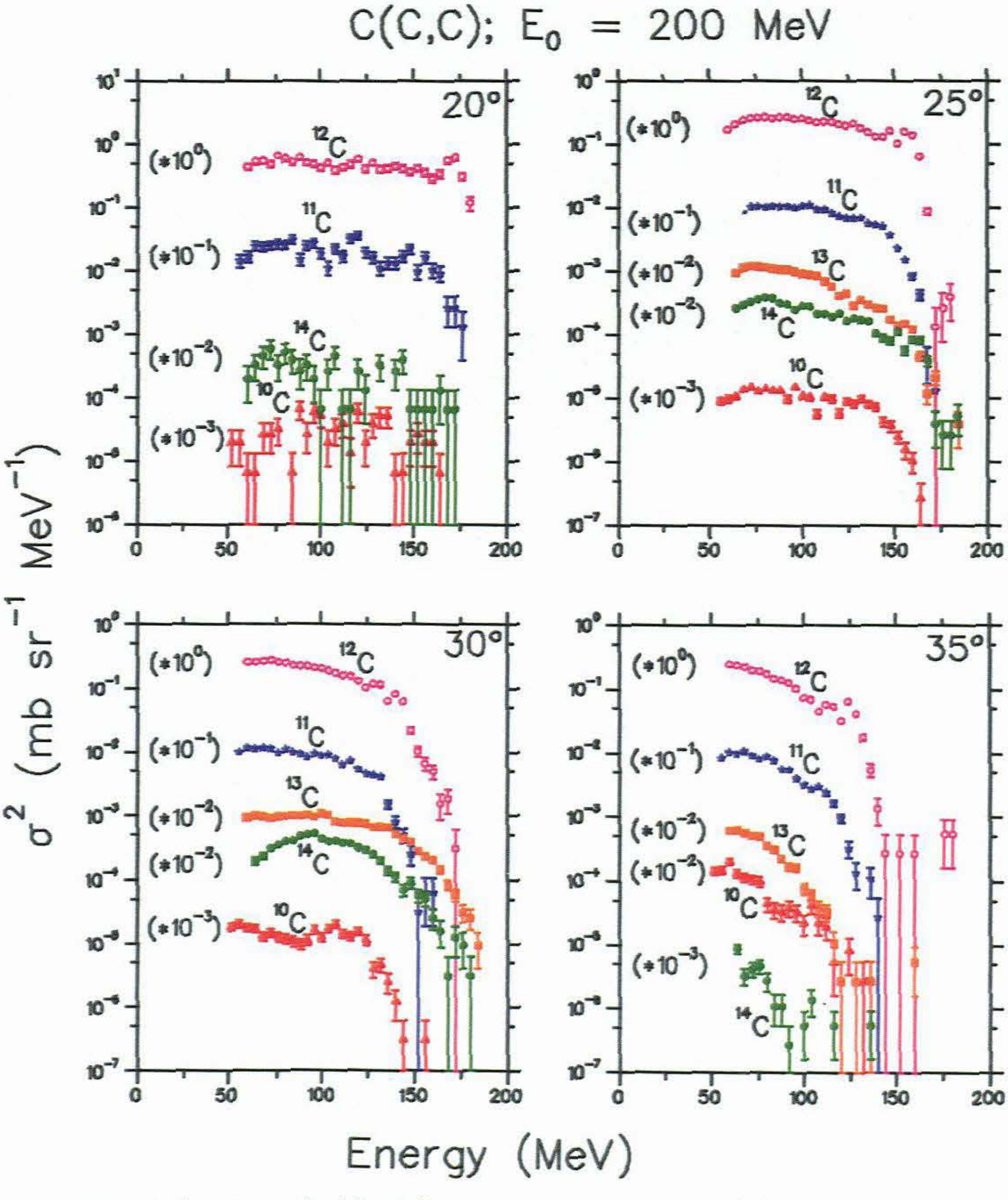

Figure 5.10: *Laboratory double differential cross sections of the carbon isotopes as indicated emitted at different angles shown in the figure in the interaction of ^{12}C with ^{12}C at an incident energy of 200 MeV. The error bars reflect the statistical errors.*

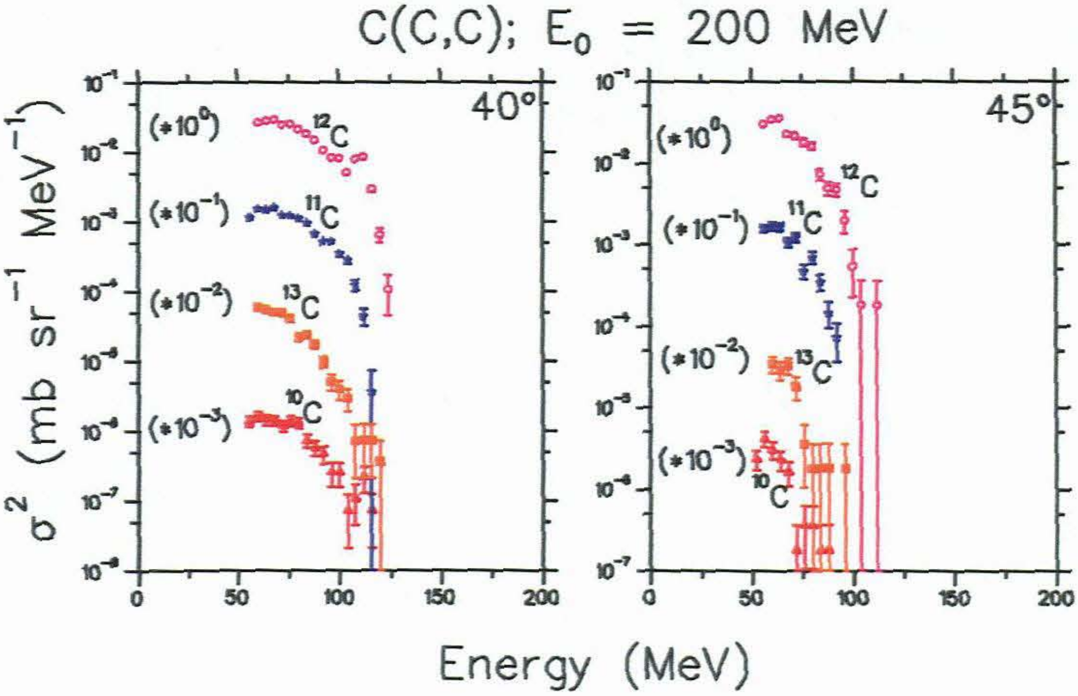

Figure 5.11: *Laboratory double differential cross sections of carbon isotopes as indicated emitted at different angles shown in the figure in the interaction of* ^{12}C *with* ^{12}C *at an incident energy of 200 MeV. The error bars reflect the statistical errors.*

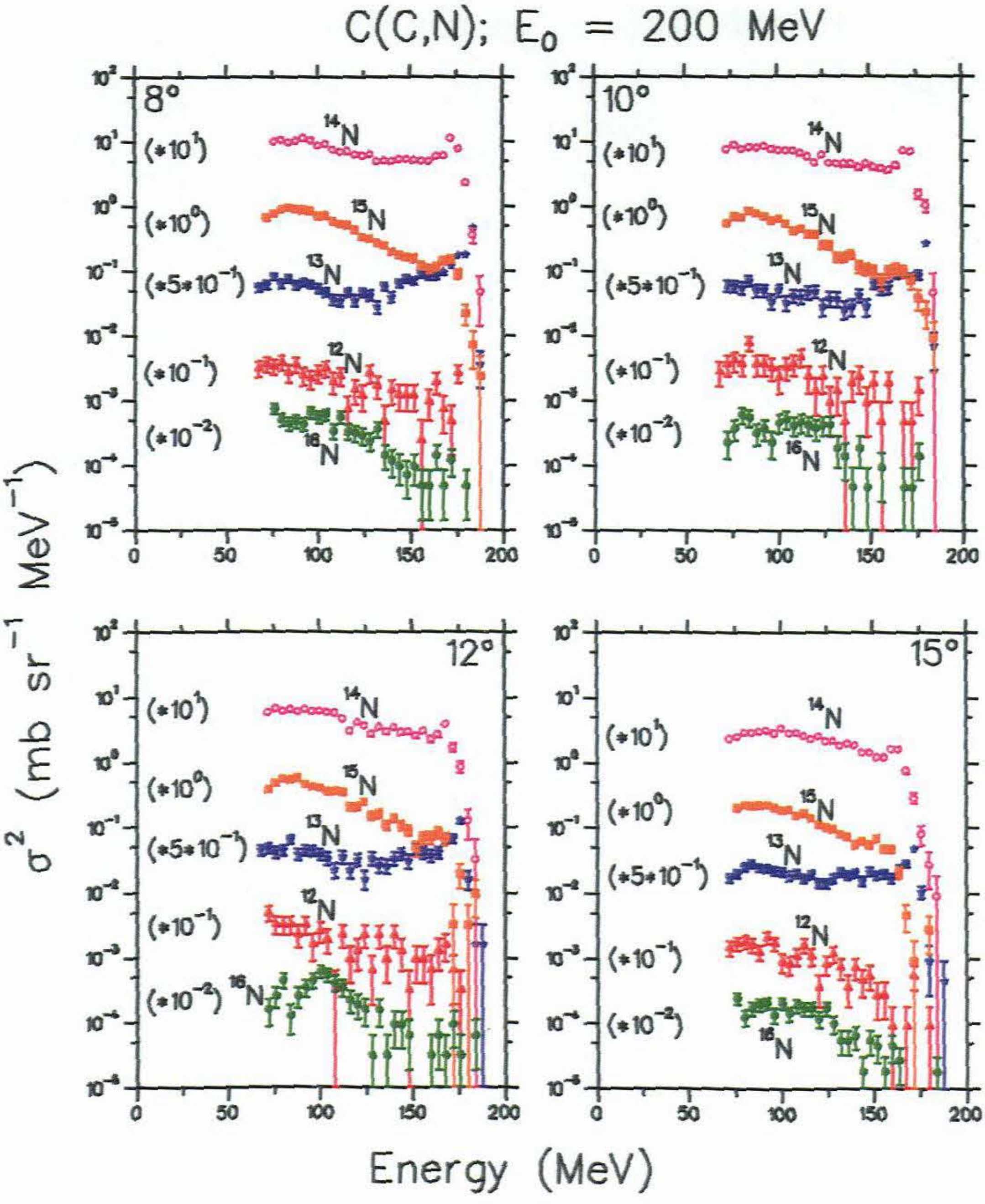

Figure 5.12: *Laboratory double differential cross sections of the nitrogen isotopes as indicated emitted at different angles shown in the figure in the interaction of ^{12}C with ^{12}C at an incident energy of 200 MeV. The error bars reflect the statistical errors.*

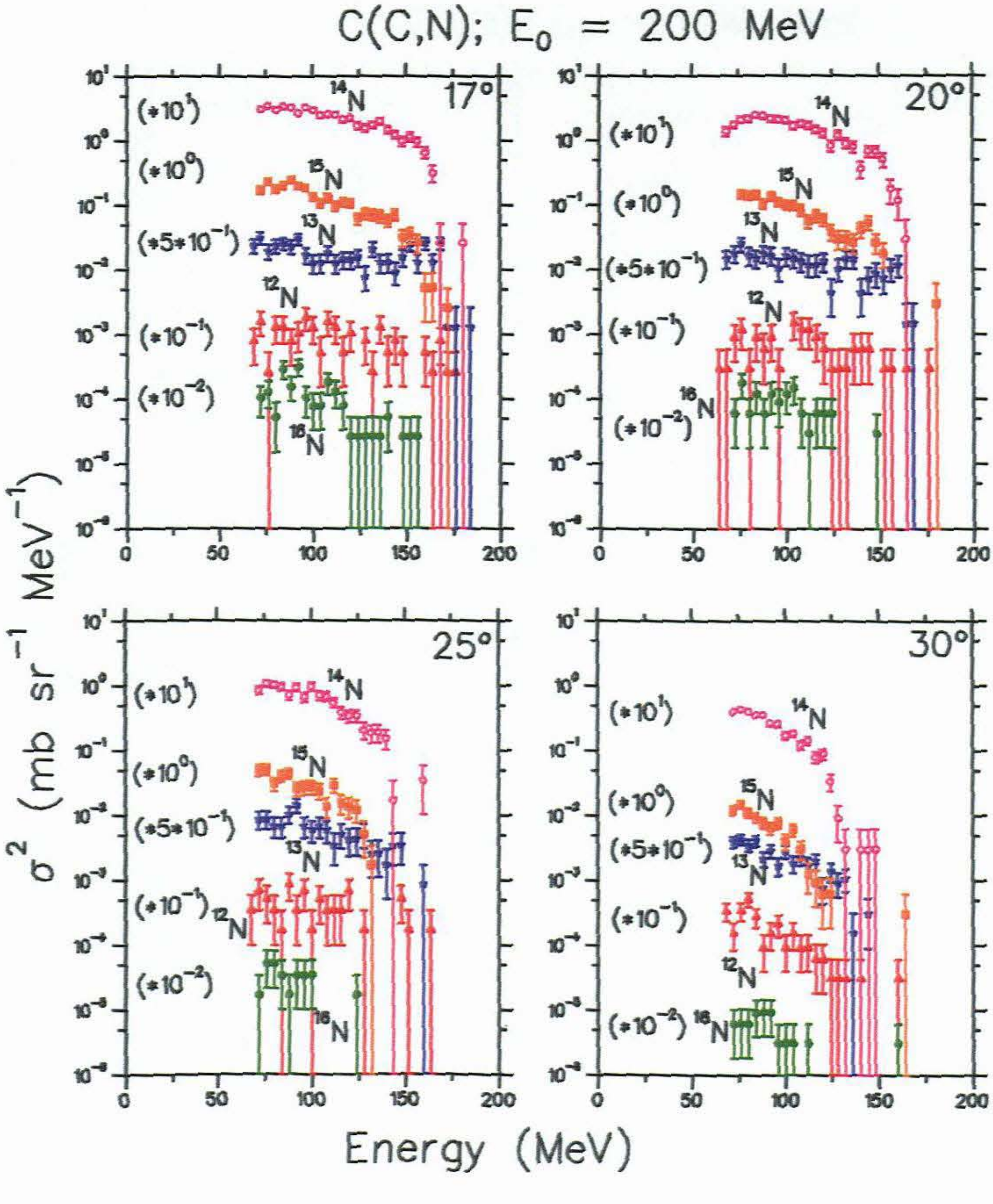

Figure 5.13: *Laboratory double differential cross sections of the nitrogen isotopes as indicated emitted at different angles shown in the figure in the interaction of ^{12}C with ^{12}C at an incident energy of 200 MeV. The error bars reflect the statistical errors.*

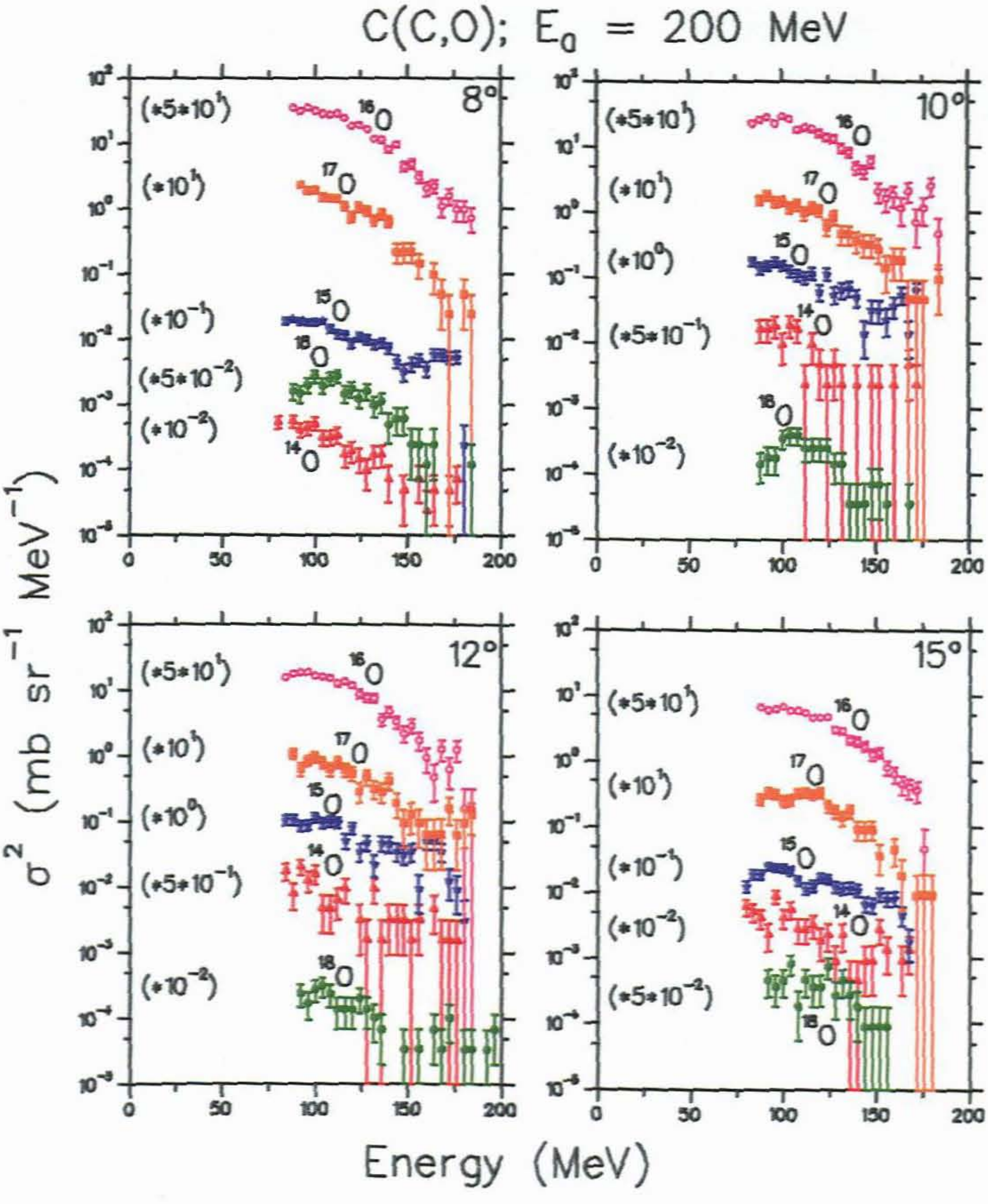

Figure 5.14: *Laboratory double differential cross sections of the oxygen isotopes as indicated emitted at different angles shown in the figure in the interaction of ^{12}C with ^{12}C at an incident energy of 200 MeV. The error bars reflect the statistical errors.*

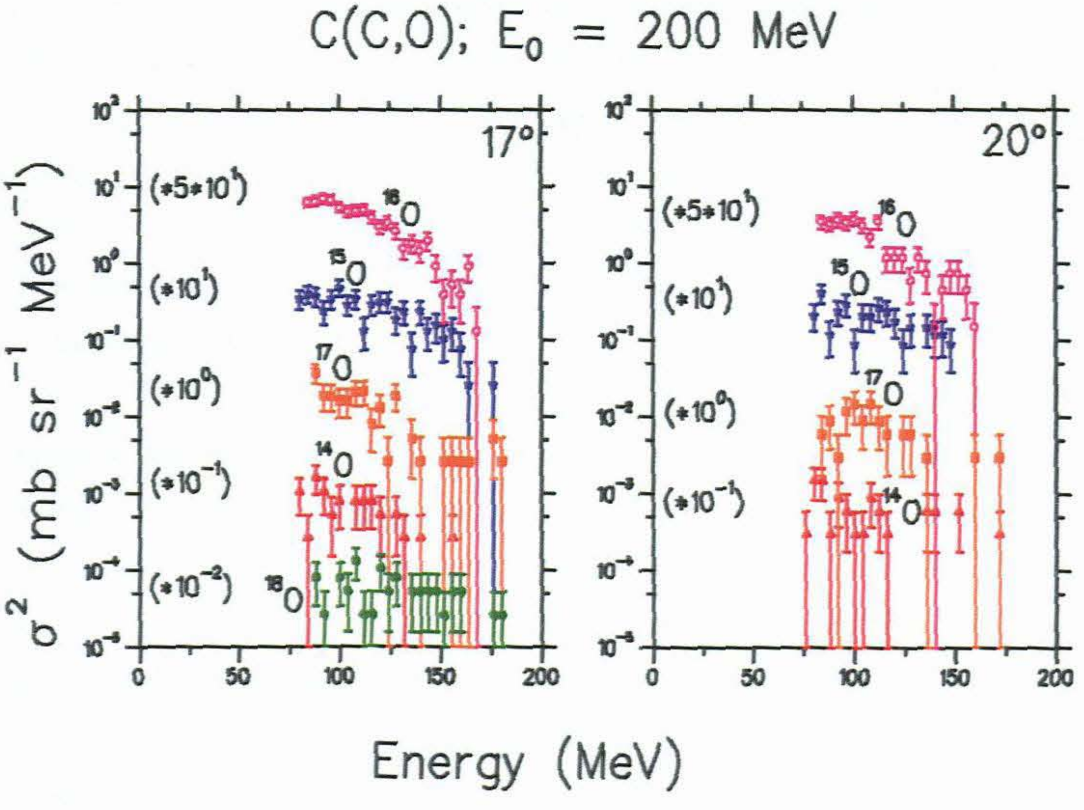

Figure 5.15: *Laboratory double differential cross sections of the oxygen isotopes as indicated emitted at different angles shown in the figure in the interaction of ^{12}C with ^{12}C at an incident energy of 200 MeV. The error bars reflect the statistical errors.*

5.4.2 Comparison of experimental energy spectra with model calculations.

The comparison between the theoretical and experimental energy spectra for $^{16,17,18}O$ at incident energy of 200 MeV are shown in figures 5.16 to 5.20 for different emission angles i.e. 8°, 10°, 12°,15°, 17°, and 20° . These figures show a good correspondence between the theoretical and experimental data.

Figures 5.16 to 5.19 show the contribution of different reaction mechanisms in the production of ^{16}O and ^{17}O in comparison with experimental double differential cross sections, respectively. These two lighter fragments (^{16}O and ^{17}O) are well reproduced by the contributions of nucleon coalescence in the complete fusion reaction and evaporation process. These fragments were obtained as evaporation residues by simulating the complete fusion with the Fluka-BME event generator and as IMFs formed by nucleon coalescence applying the BMEs alone to the complete fusion of the composite nucleus [Mai06].

Among the residues which are observed in this experiment, those with higher mass and charge such as e.g. ^{18}O, are presumably produced by a complete fusion process and the subsequent emission of light particles both in the pre-equilibrium and the evaporation stage leaving them as residues. In fact, being of mass significantly larger than that of the interacting ions, it is quite unlikely that they are produced by nucleon coalescence in the complete fusion process and it is also unlikely that they are produced in complete fusion reactions, because, for instance, the incomplete fusion of a ^{8}Be from one of the interacting carbons with the other produces a ^{20}Ne, with an excitation energy such that the subsequent pre-equilibrium emissions and evaporations will presumably produce lighter residues. Figure 5.20 shows the comparison of measured and calculated double differential cross section ^{18}O spectra at different angles. The calculations slightly overestimate the cross sections of ^{18}O at all angles. The agreement is nevertheless acceptable.

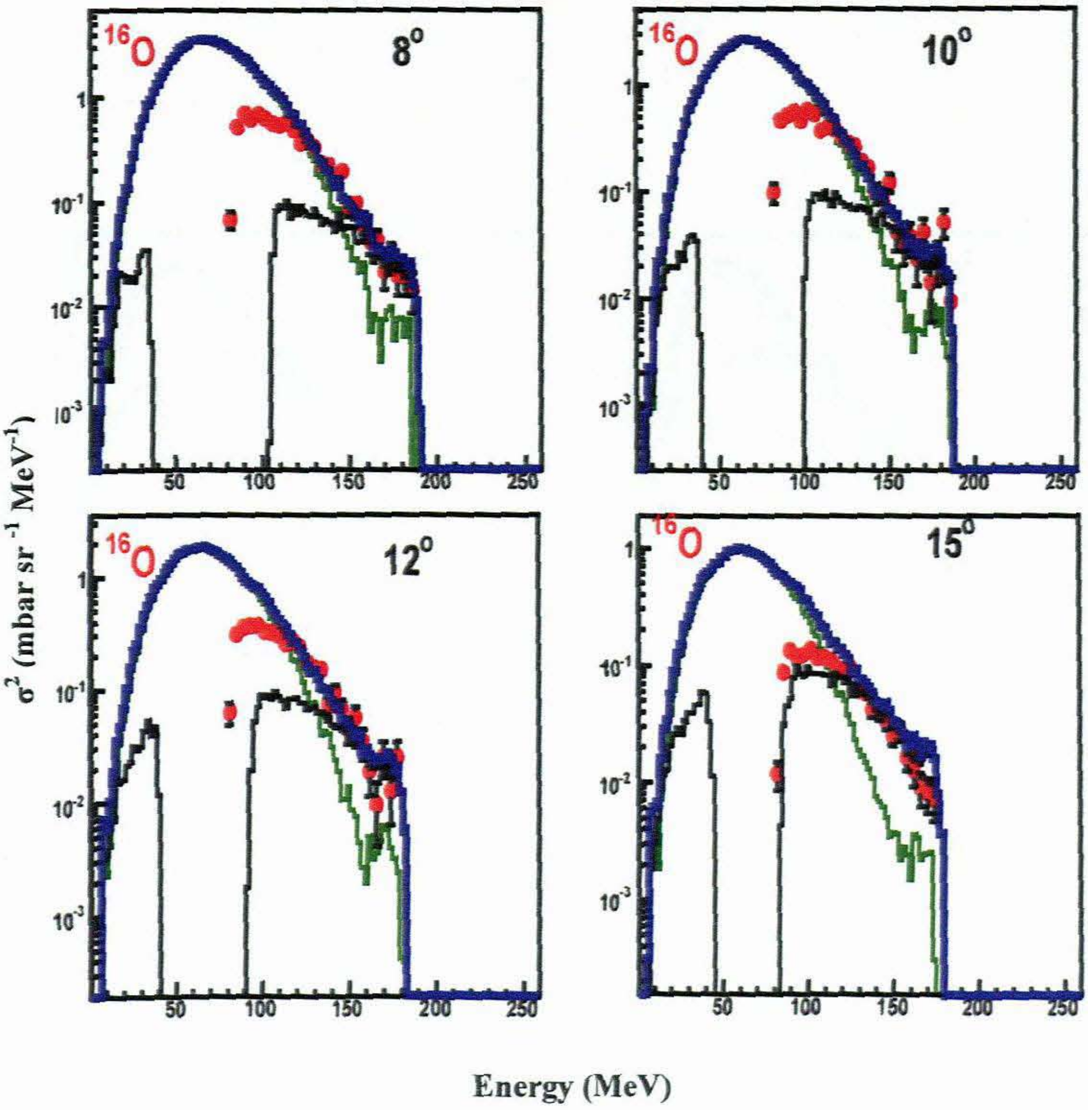

Figure 5.16: *The comparison of the measured and the calculated double differential cross section spectra of ^{16}O at different angles shown in the figure [Mai06]. ^{16}O is emitted in the interaction of ^{12}C + ^{12}C at incident energy of 200 MeV. The red points with error bars give the experimental result, the green histograms the predicted spectra of evaporation residues, the black histograms represent fragments produced by nucleon coalescence in a complete fusion reaction, the blue histograms the sum of the two theoretical contributions.*

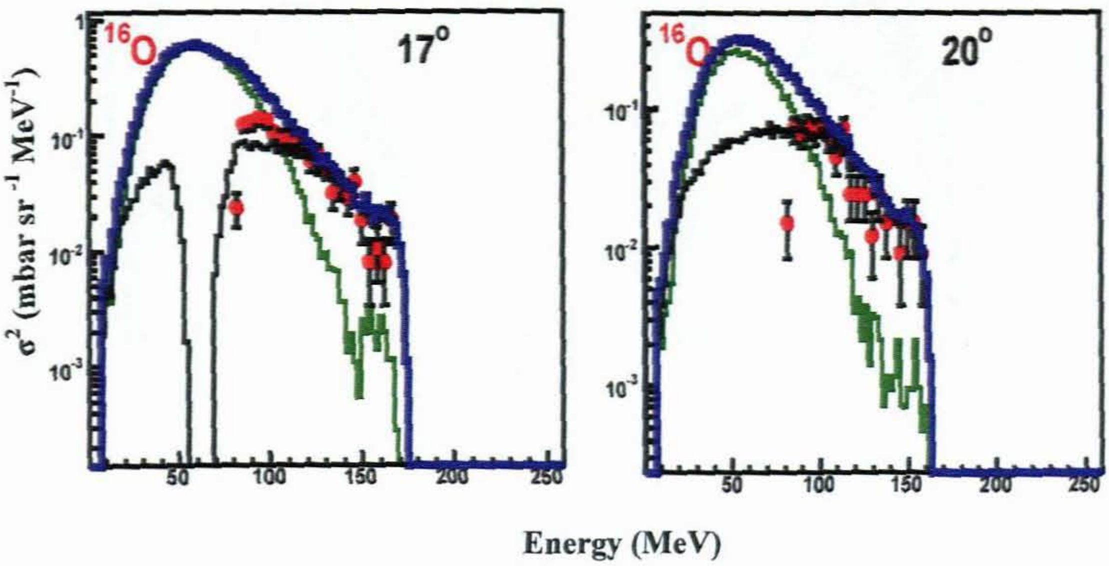

Figure 5.17: *The comparison of the measured and the calculated double differential cross section spectra of ^{16}O at different angles shown in the figure [Mai06]. ^{16}O is emitted in the interaction of ^{12}C + ^{12}C at incident energy of 200 MeV. The red points with error bars give the experimental result, the green histograms the predicted spectra of evaporation residues, the black histograms represent fragments produced by nucleon coalescence in a complete fusion reaction, the blue histograms the sum of the two theoretical contributions.*

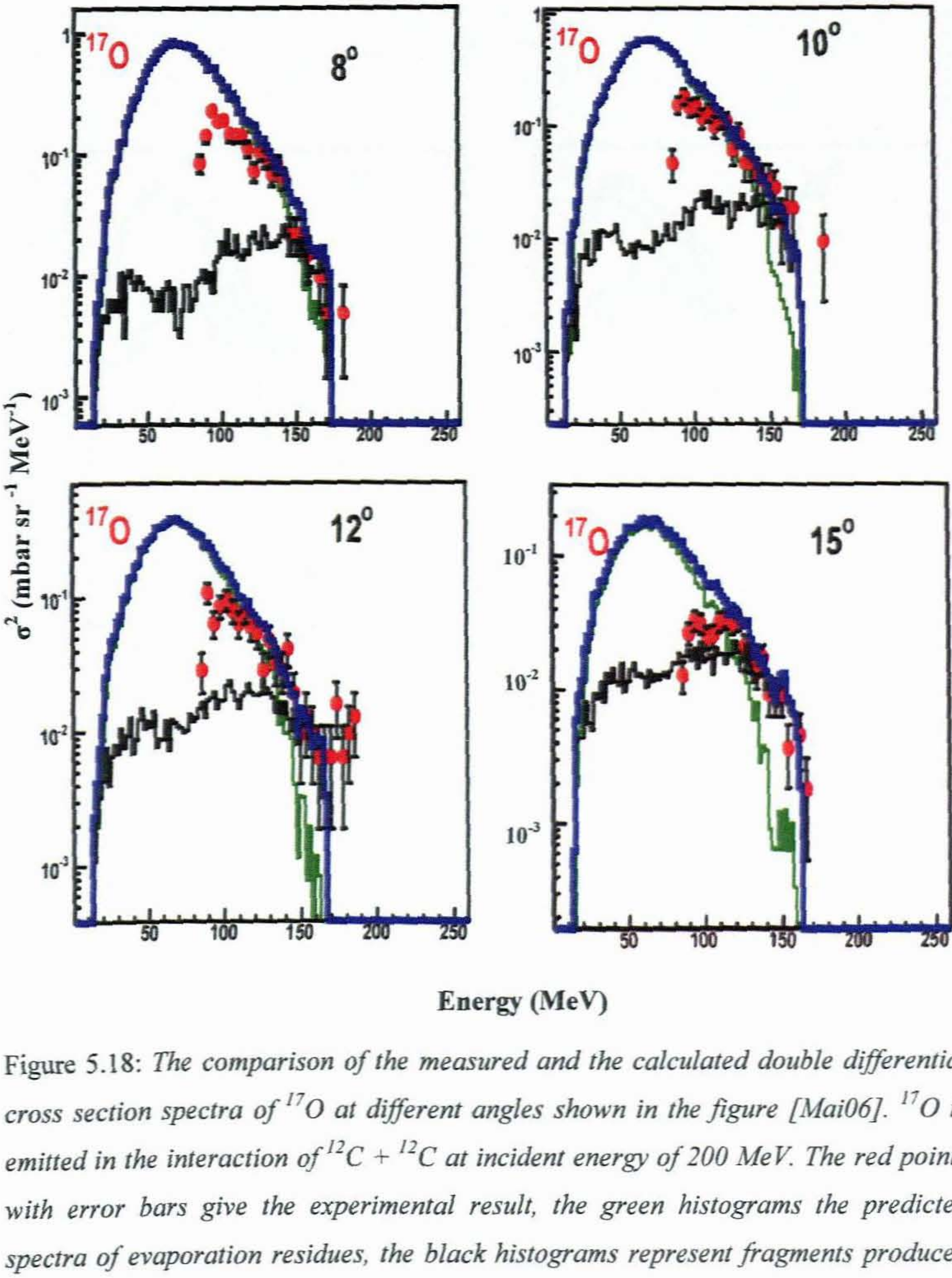

Figure 5.18: *The comparison of the measured and the calculated double differential cross section spectra of ^{17}O at different angles shown in the figure [Mai06]. ^{17}O is emitted in the interaction of ^{12}C + ^{12}C at incident energy of 200 MeV. The red points with error bars give the experimental result, the green histograms the predicted spectra of evaporation residues, the black histograms represent fragments produced by nucleon coalescence in a complete fusion reaction, the blue histograms the sum of the two theoretical contributions.*

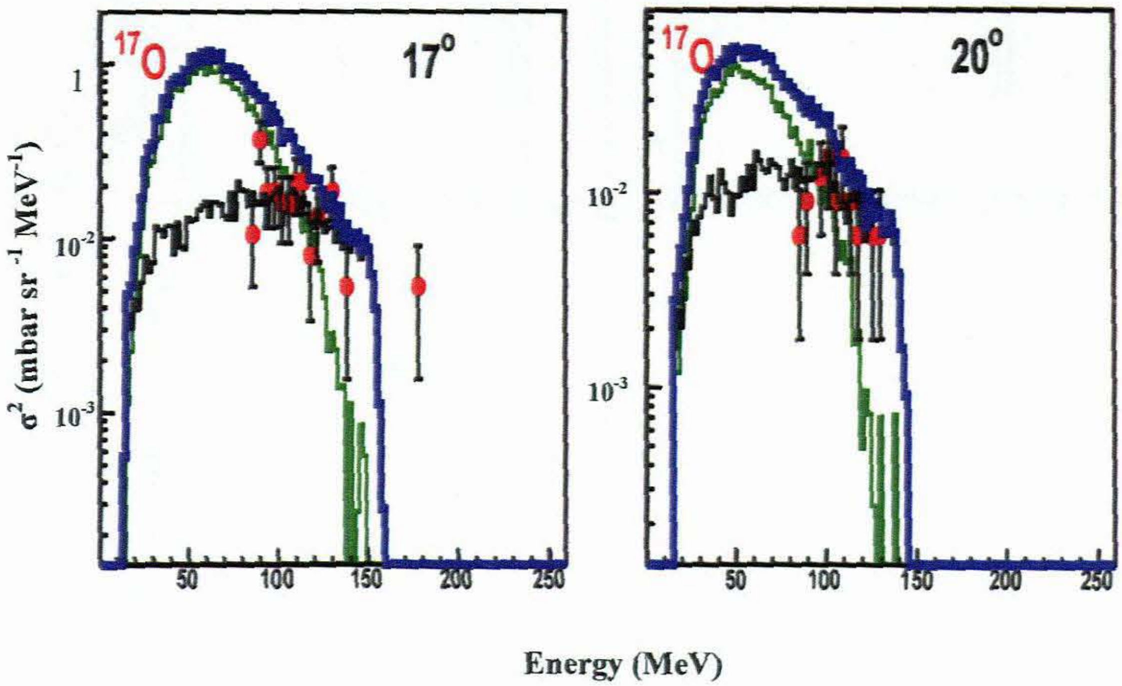

Figure 5.19: *The comparison of the measured and the calculated double differential cross section spectra of ^{17}O at different angles shown in the figure [Mai06]. ^{17}O is emitted in the interaction of $^{12}C + ^{12}C$ at incident energy of 200 MeV. The red points with error bars give the experimental result, the green histograms the predicted spectra of evaporation residues, the black histograms represent fragments produced by nucleon coalescence in a complete fusion reaction, the blue histograms the sum of the two theoretical contributions.*

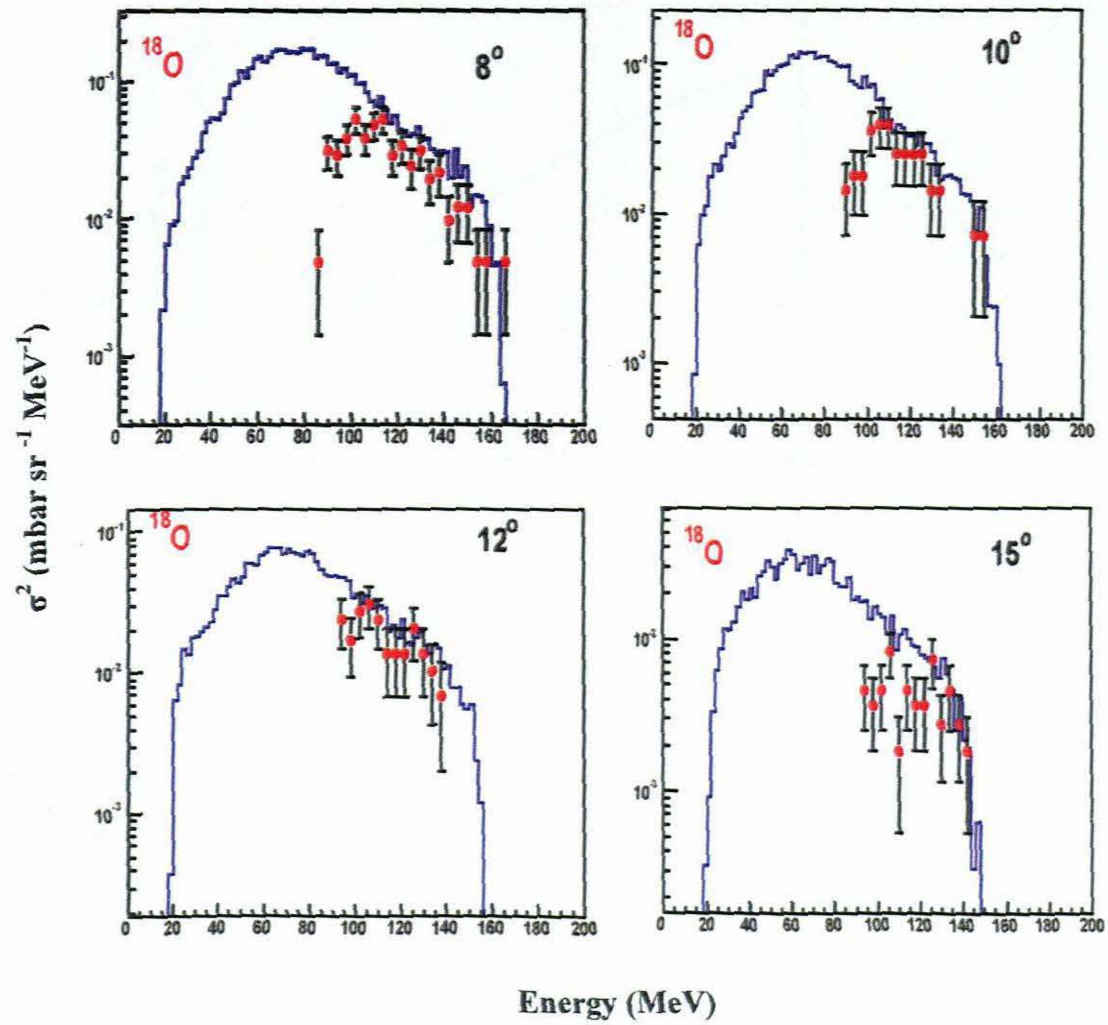

Figure 5.20: *The comparison of the measured and the calculated double differential cross section spectra of ^{18}O at different angles shown in the figure[Mai06]. ^{18}O is emitted in the interaction of ^{12}C + ^{12}C at incident energy of 200 MeV. The red points with error bars give the experimental result, the blue histograms the theoretical estimate.*

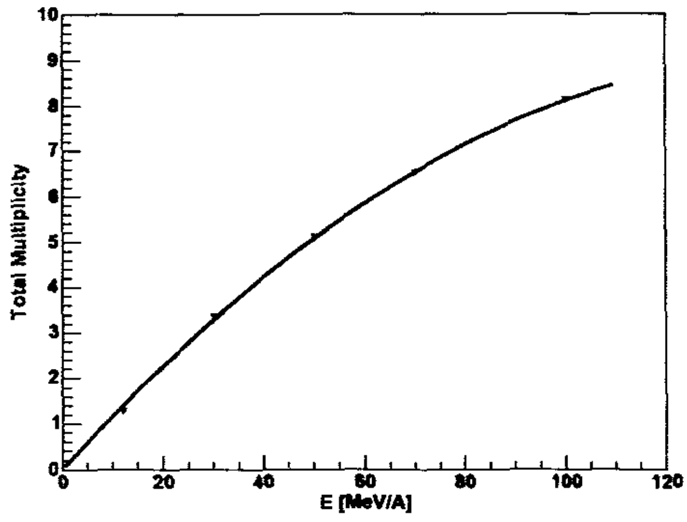

Figure 5.21. *Theoretical prediction of the average total multiplicity of pre-equilibrium ejectiles in the complete fusion of two ^{12}C ions as a function of the incident energy. The triangles give the values predicted by the BMEs, the line is a parabolic fit [Mai06].*

Fig. 5.21 shows the average multiplicity of all ejectiles emitted in the pre-equilibrium phase at 200 MeV incident energy, as predicted by the BMEs [Mai06]. The theoretical predictions show that at an incident energy of 16.67 MeV/n approximately two ejectiles may be emitted during the pre-equilibrium stage. Figure 5.22 shows the differential reaction cross section as a function of the impact parameters also obtained with the BME at an incident energy of 16.67 MeV. At smaller impact parameters the reaction in dominated by complete fusion since the there is central collision between the target and the projectile. As the impact parameter b increases three body scattering which are two particles emitted as predicted by the BMEs and the residual nucleus dominate. These results in the emission of fast particles by pre-equilibrium processes, nucleon coalescence and further by evaporation. All these processes contribute most to the reaction cross section at average impact parameter. At high impact parameters, this reaction mechanism smoothly changes to inelastic scattering (Fig. 5.22) which includes processes such as transfer reactions.

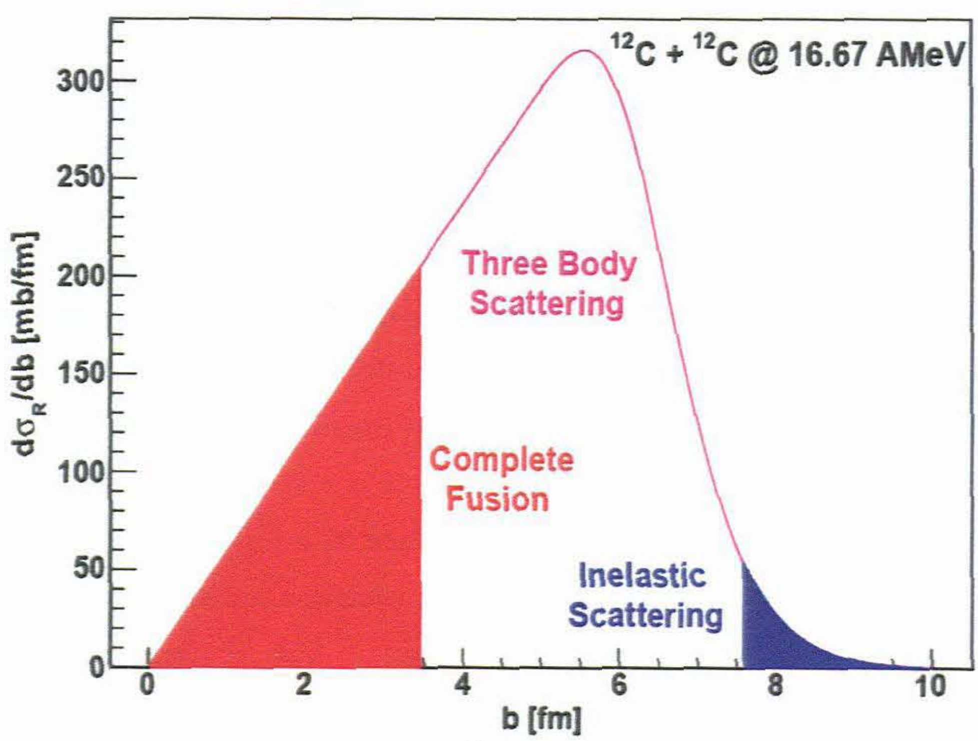

Figure 5.22. *Differential reaction cross section as function of impact parameter b.*

CHAPTER 6

6.1 Summary and conclusions

Double differential cross sections of C, N, O, and their isotopes have been measured in the angular range of 8° to 60° in the interaction of ^{12}C with ^{12}C at an incident energy of 200 MeV. The aim of this study was to study the reaction mechanisms involved in the production of these fragments.

Continuum energy spectra of C, N, and O fragments were obtained by measuring the high energy parts of these spectra with the Si detector telescope while the corresponding low energy parts were measured with the BCD. Isotope separation was achieved with the Si detector telescope ΔE-E technique. The double differential cross sections were extracted from these energy spectra. The double differential cross sections showed that the extracted data of these two detectors are more or less consistent, despite the gaps observed between the data due to tailing effects discussed in section 3.8. These double differential cross sections decay exponentially at larger angles. The angular distributions of the C, N, and O fragments were extracted for different energy cross section at selected energies showed. It is significant that for the lowest emission energy i.e. 20 MeV the angular distribution is almost isotropic with respect to the emission especially for carbon fragments. The slopes of the angular distributions of C, N, and O fragments decrease rapidly as the emission angle increases. Also the angular distributions become steeper as the mass of the detected fragment increases. This change in the slope of the cross sections could indicate a change in the reaction mechanisms from a transfer reaction at higher energies to pre-equilibrium reactions and nucleon coalescence dominant at lower emission energies and eventually to evaporation.

The double differential cross sections of carbon isotopes at high emission energies and at the most forward angles show that the dominant reaction mechanism is the transfer reaction of few nuetrons or protons from the projectile to the target or vice versa. This process has also been suggested in the previous studies of the fragmentation of ^{12}C interacting with ^{12}C at an incident energy of 28.7 MeV/n [Czu91]. This conclusion is supported by the presence of the discrete states observed in the spectra of carbon isotopes at forward angles and high emission energies. These discrete states decrease very rapidly as the emission angle increases. Pre-equilibrium processes as well as evaporation process mainly dominate the emission of the fragments to the continuum. These particles are emitted with high energies and contribute to the bulk of the continuum cross sections first by nucleon coalescence which occurs in a very short time interval and increasingly by evaporation processes. The evaporation process during which light particles evaporate from the excited composite system leads to these IMF as residues is dominant both at forward angles and larger angles. This reaction mechanism dominates as the IMF mass increases.

Experimental cross sections have been compared with nucleus-nucleus interaction calculations. These calculations were performed with the FLUKA code based on the BME theory in order to test the inferred reaction mechanisms involved in the production of $^{16,17,18}O$ isotopes. From the theoretical treatment of the double differential cross sections of the lighter fragments such as $^{16,17}O$, good agreement was found between the calculated and the measured double differential cross sections. It can be concluded that these fragments were produced by nucleon coalescence in the complete fusion reaction and as evaporation residues. A complete fusion process and the subsequent emission of light particles both in the pre-equilibrium and the evaporation stage of the reaction leaving them as residues presumably produce fragments with a larger mass such as ^{18}O. The overall conclusion from these calculations is that the fragments heavier than ^{17}O are produced as evaporation residues in a complete fusion process accompanied by the emission of light particles.

6.2 Outlook

In order to fully understand the reaction mechanisms involved in the production of the fragments with mass equal to the projectile or target and the change in the reaction mechanisms as the mass of the fragment detected increases, the ongoing theoretical calculations for carbon and nitrogen isotopes should be compared to the present measured cross sections. In addition the emission of fragments lighter than the projectile or target could lead to the further investigation of reaction mechanisms involved in their emission at incident energy of 200 MeV, such as projectile or target break-up.

The tailing effects observed with the BCD could be excluded in future work by analyzing the BCD data differently. Instead of plotting the Bragg peak against the energy of the detected particle one may use the length of the signal against the energy of the particle. This could lead to the well separation of the particles that punch the detector and those that are stopped in the detector. By gating the stopped particles, the clean PID spectra without tailing effects could be generated. Also one can employ the ΔE-E technique by using the BCD with ancillary stopping detector to measure the high energy particles of the light fragments. Such a setup was previously used in the PISA experiment [Bar04]. With this setup it might be possible to obtain cleaner BCD PID spectra such that the gaps observed between the Si detector telescope and BCD data are eliminated.

In the case of the silicon detector telescope, the preamplifiers with a lower gain should be employed especially to measure the high energy component of the yield for the heavier fragments. With the present gain settings the signals from the detector for these high energy events is distorted by high gain preamplifiers, leading to loss of information.

REFERENCES

[And92] L.N. Andronenko, M.N. Andronenko, A.A. Kotov, W. Neubert, L.A. Vaishnene, S.A. Pavlenko, D.M. Seliverstov, V.L. Stepanov and V.I. Yatsura, Nuclear Instruments and Methods in Physics Research A **312,** 467-474 (1992).

[Ass82] J.M. Asselineau, J. Duchon, M. L'Haridon, P. Mosrin, R. Regimbart and B. Tamain. Nuclear Instruments and Methods **204,** 109-115 (1982).

[Awe81] T.C. Awes, G. Poggi, C.K. Gelbke, B.B. Back, B.G. Glagola, H. Breuer, V.E. Viola, Phys. Rev. C **24,** 89 (1981).

[Bar04] R. Barna, V. Bollini, A. Bubak, A. Budzanowski, D. De Pasquale, D. Filges, S.V. Förtsch, F. Goldenbaum, A. Heczko, H. Hodde, A. Italiano, L. Jarczyk, B. Kamys, J. Kisiel, M. Kistryn, St. Kistryn, St. Kliczewski, A. Kowalczyk, P. Kulessa, H. Machner, A. Magiera, J. Majewski, W. Migdal, H. Ohm, N. Paul, B. Piskor-Ignatowicz, K. Pysz, Z. Rudy, H. Schaal, R. Siudak, E. Stephan, G.F. Steyn, R. Sworst, T. Thovhogi, M. Wojciechiwski, W. Zipper, Nuclear Instruments and Methods in Physics Research A **519**, 610-622 (2004).

[Bec03] B. Becker, F. Albertini, E. Gadioli, G.F. Steyn, M. Cavinato, S.H. Connell, A.A. Cowley, E. Fabrici, S.V. Förtsch, E. Gadioli Erba, J.J. Lawrie, and E. Sideras Haddad, Eur. Phys. J. A **18**, 639-644 (2003).

[Bir96] C. Birattari, M. Bonardi, M. Cavinato, E. Fabrici, E. Gadioli, E. Gadioli Erba, F. Groppi, M. Bello, C. Bovati, and A. Di Filippo, Phys. Rev. C **54**, No. 6, 3051 (1996).

[Bun47] O. Bunemann, T.E. Cransshaw and J.A. Harvey, Canadian Journal of Research, Vol. **27**, Section A, 191-206 (1947).

[But04] E.Z. Buthelezi, E. Gadioli, G.F. Steyn, F. Albertini, C. Birattari, M. Cavinato, F. Cerutti, S.H. Connell, A.A. Cowley, E. Fabrici and E. Gadioli Erba. Nuclear Physics A **734,** 553-556 (2004).

[Cav01] M. Cavinato, E. Fabrici, E. Gadioli, E. Gadioli Erba, and G. Riva, Nucl. Phys. A **679,** 753 (2001).

[Cav94] M. Cavinato, E. Fabrici, E. Gadioli, E. Gadioli Erba, M. Galmarini, A. Gritti, Z. Phys. A **347**, 237 (1994).

[Cav98] M. Cavinato, E. Fabrici, E. Gadioli, E. Gadioli Erba, E. Risi, Nuclear Physics A **643,** 15-29 (1998).

[Cer05] F.Cerutti, A. Clivio and E. Gadioli, Eur. Phys. J. A25, 413 (2005).

[Cer06] F. Cerutti *et al.*, Proceedings of the 11th International Conference on Nuclear Reaction Mechnisms, Varenna, June 12-16, 2006, E. Gadioli edt., Ricerca Scientifica and Educazione Permanente, Suppl. **126,** 507-514 (2006).

[Cer92] I. Cervesato, I. Fabrici, E. Gadioli, E. Gadioli Erba, M. Galmarini, Phys. Rev. C **45,** 2369 (1992).

[Czu91] J. Czudek, B. Kamys, A. Magiera, R, Siudak, A. Strzakowski, and B. Steyczen, Phys. Rev C **43,** No.3 (1991).

[Fab89] E. Fabrici, E. Gadioli, E. Gadioli Erba, M. Galmarini, F. Fabbi, G. Reffo, Phys. Rev. C **40,** 2548 (1989).

[Fab91] E. Fabrici, E. Gadioli, E. Gadioli Erba, M. Galmarini, Z. Phys. A **338,** 17 (1991).

[Fas03] The physics models of FLUKA: status and recent developments, A. Fasso`, A. Ferrari, A. Ottolenghi, A. Empl and J. Ranft, Computing in High Energy and Nuclear Physics 2003, (paper MOMT005), eConf C0303241 (2003), arXiv:hep-ph/0306267.

[Fas05] FLUKA: a multi-particle transport code, A. Fasso`, A. Ferrari, J. Ranft, P.R. Sala, CERN-2005-10 (2005), INFN/TC_05/11, SLAC-773.

[För05] S.V. Förtsch, F. Cerutti, P. Colleoni, E. Gadioli, A. Mairani, G.F. Steyn, J.J. Lawrie, F.D. Smit, S.H. Connell, R.W. Fearrick, T. Thovhogi, H. Machner, F. Goldebaum and K. Pysz. "Projectile and target fragmentation in the interaction of ^{12}C and ^{27}Al." (Unpublished).

[För92] S.V. Förtsch, Proton emission in pre-equilibrium reactions induced by protons of 100 and 200 MeV, PhD thesis (1992), University of Pretoria (Unpuplished).

[Gad00] E. Gadioli, M. Cavinato, E. Gadioli Erba, R. Bassini, C. Birattari, S. Crippa, G.F. Steyn, S.V. Förtsch, J.J. Lawrie, F.M. Nortier, S.H. Connell, E. Sideras Haddad, J.P.F. Sellschop, and A.A. Cowley. "Evidence for a dissipative friction mechanisms based on ^{8}Be fragments from the interaction of ^{12}C with ^{59}Co." (Unpublished).

[Gad02] E. Gadioli, G.F. Steyn, C. Birattari, C. Catarisano, M. Cavanato, S.H. Connell, A.A. Cowley, E. Fabrici, S.V. Förtsch, E. Gadioli Erba, J.J. Lawrie, J.P.F. Sellschop, E. Sideras Haddad, Nuclear Physics A **708**, 391-412 (2003).

[Gad03] E. Gadioli, G.F. Steyn, F. Albertini, C. Birattari, M. Cavinato, S.H. Connell, A.A. Cowley, E. Fabrici, S.V. Förtsch, E. Gadioli Erba, J.J. Lawrie, M. Pigni, J.P.F. Sellschop, and E. Sideras Haddad. Eur. Phys. J. A **17**, 195-212 (2003).

[Gad92] E. Gadioli and P.E. Hodgson. Pre-Eqiulibrium Nuclear Reactions (Oxford Clarendon Press, 1992).

[Gad97] E. Gadioli, C. Birattari, M. Cavinatto, E. Fabrici, E. Gadioli Erba, V. Allori, C. Bovati, F. Cerutti, A. Di Fillippo, S. Vailati, T.G. Stevens, S.H. Connell, J.P.F. Sellschop, S.J. Mills, F.M. Nortier, G.F. Steyn, C. Marchetta, Physics Letters B **394**, 29-36 (1997).

[Gad98] E. Gadioli, C. Birattari, M. Cavinatto, E. Fabrici, E. Gadioli Erba, V. Allori, F. Cerutti, A. Di Fillippo, S. Vailati, T.G. Stevens, S.H. Connell, J.P.F. Sellschop, F.M. Nortier, G.F. Steyn, C. Marchetta, Nuclear Physics A **641**, 271-296 (1998).

[Gad99] E. Gadioli, M. Cavinato, E. Fabrici, E. Gadioli Erba, C. Birattari, I. Mica, S. Solia, G.F. Steyn, S.V. Förtsch, J.J. Lawrie, F.M. Nortier, T.G. Stevens, S.H. Connell, J.P.F. Sellschop, A.A. Cowley, Nuclear Physics A **654,** 523-540 (1999).

[Gou83] C.R. Gould and N.R. Roberson, IEEE Transaction on Nuclear Science, Vol. NS-**30**, No.5, October 1983.

[Har68] G.D. Harp, J.M. Miller, B.J. Berne, Phys. Rev. **165**, 1166 (1968).

[Jip84] P. Jipsen, ELOSS, A program for calculating the ranges of ions in matter, National Accelerator Center (1984) (unpublished).

[Kar75] P.J. Karol, Phys. Rev. C**11**, 1203 (1975).

[Leo87] R.W. Leo, Techniques for Nuclear and Particle Physics Experiment, (Springer-Verlag Berlin Heidelberg, 1987).

[Lil01] J.S. Lilley, Nuclear physics, Principles and applications, (2001).

[Mag98] A. Magiera, J. Hebenstreit, L. Jarczyk, B. Kamys, A. Strzalkowski, and B. Styezeń, Phy. Rev. C **57**, 749-763 (1998).

[Mai06] A. Mairani, PhD thesis, (2006).

[McV80] K.W. McVoy, M. Carolina Nemes. Z. Phys. A **295**, 177 (1980).

[Mör88] K. Mörhring, T. Srokowski, D.H.E. Gross and H. Homeyer, Physics Letters B **203**, 210-214 (1988).

[Mud05] L.J. Mudau, M.SC thesis. "Emission of ^{3}He and ^{6}He particles from the interaction of ^{12}C with ^{93}Nb at 400 MeV incident energy" (2005).

[Nts05] S.S. Ntshangase, "Measurement of the fusion barrier distribution for the ^{86}Kr + ^{208}Pb reaction", M.Sc Thesis "unpublished" (2005).

[Och96] H. Ochiishi, H, Ito, K. Kimura, S. Kouda, T. Murakami, Shimooka, Y. Sugaya, K.H. Tanaka, S. Toyama, Y. Yamanoi, K. Yamamoto, K. Yasuda. Nuclear Instruments and Methods in Physics Research A **369,** 269-279 (1996).

[Paw97] J. Pawelke, W. Enghardt, Th. Harberer, B.G. Hasch, R. Hinz, M. Kramer, K. Lauckner and M. Sobiella. IEEE TRANSACTIONS ON NUCLEAR SCIENCE, VOL. **44**, NO.4 AUGUST 1997

[Pil96] J.V. Pilcher, The NAC MBD to VME Conversion Guide (1996).

[Ser47] R. Serber. Phys. Rev. **72**, 1008 (1947).

[She85] N.J SHENHAV and H. STELZER, Nuclear Instruments and Methods in Physics Research 228, 359-364 (1985).

[Ste97] S.W. Steyn, "Multistep direct reactions in nuclei", PhD Thesis.

[Sze91] A. Szezurek, A. Budzanowski, L. Jarczyk, A. Magiera, K. Möhring, R. Siudak, and T. Srokowski, Z. Phys. A – Hadrons and Nuclei **338,** 187-191 (1991).

[Tan95] K.H. Tanaka, Y. Yamanoi, H. Ochiichi, H. Akiyoshi, S. Kounda, H. Nakamura, S. Morinobu, Y. Tanaka, K. Kimura, T. Shibata, Y. Sugaya, K. Yasuka, H. Ito, and T. Murakami, Nucl. Phys. A **583**, 581 (1995).

[Tho03] Tshilidzi Thovhogi, "Application of a Bragg Curve Detector to inclusive (p,a) reactions to the continuum." M.Sc Thesis (unpublished) (2002.